INTEGRATION OF TIME-RESOLVED FLUORESCENCE AND DIFFUSE REFLECTANCE SPECTROSCOPY FOR INTRAOPERATIVE DETECTION OF BRAIN TUMOUR MARGIN

INTEGRATION OF TIME-RESOLVED FLUORESCENCE AND DIFFUSE REFLECTANCE SPECTROSCOPY FOR INTRAOPERATIVE DETECTION OF BRAIN TUMOUR MARGIN

By

Zhaojun Nie, M.Sc. B.Sc.

A Thesis

Submitted to the School of Graduate Studies

In Partial Fulfillment of the Requirements for the Degree

Doctor of Philosophy

McMaster University

©Copyright by Zhaojun Nie, February 2014

Doctor of Philosophy (2014) McMaster University

School of Biomedical Engineering Hamilton, Ontario

TITLE: Integration of time-resolved fluorescence and diffuse reflectance spectroscopy for intraoperative detection of brain tumour margin

Author: Zhaojun Nie,

M.Sc., Beijing Institute of Technology

B.Sc., Xi'an University of Post and Telecommunications

Supervisor: Qiyin Fang, Ph.D.

Number of pages: xviii, 129

Abstract

The annual incidence rate of tumours in the brain and central nervous system (CNS) was 19.89 per 100,000 persons between 2004 and 2008 in the United States. Surgery is a common treatment option for brain and CNS tumours. Typically, biopsy followed by histological analysis is used to confirm tumour types and margin during neurosurgery as an intraoperative diagnostic tool. However, this biopsy method is invasive, sampling number limited and not in real-time. To overcome these problems, many minimally invasive optical techniques, called optical biopsies, have been developed towards intraoperative diagnosis.

The research work carried out in this dissertation focuses on combining the time-resolved fluorescence (TRF) and diffuse reflectance (DR) spectroscopy towards intraoperative tumour margin detection in neurosurgery. Combining these two modalities allows us to obtain additional contrast features, thus potentially improving the diagnostic accuracy. To achieve this goal, first, a clinically compatible integrated TRF-DR spectroscopy instrument was developed for *in vivo* brain tumour study. An acousto-optical-tunable-filter-based spectrometer was designed to acquire the time-resolved fluorescence signal. A dual-modality fibre optic probe was used to collect the TRF and DR signals in a small volume. The system's capabilities of resolving fluorescence spectrum and lifetime, and optical properties were characterized and validated using tissue phantoms. Second, in order to retrieve the fluorescence impulse response function accurately from measured fluorescence signals, a robust Laguerre-based deconvolution method was optimized by using the constrained linear least squares fitting and high order Laguerre function basis. This optimized Laguerre-based deconvolution method overcomes the over-fitting problem introduced by low signal-to-noise ratio and complex fitting model. Third, an *ex vivo* clinical study of brain tumours was carried out using the TRF and DR spectroscopy. Fluorescence spectra and lifetime features were selected to classify various tumour types. The sensitivity and specificity of meningioma grade I differentiated from meningioma grade II are both 100%. Finally, in order to increase the measurement tissue volume and obtain imaging contrast features, a scanning-based hyperspectral fluorescence lifetime imaging system was developed. This setup can provide time-, space-, spectrum- resolved multi-dimensional images for tumour margin detection.

Acknowledgments

I would like to express my appreciation to my PhD supervisor, Dr. Qiyin Fang, for his advices and helps throughout my PhD study period. I also want to thank my committee members Dr Joseph E. Hayward, Dr Thomas J. Farrell, and Dr Kevin Diamond for their valuable discussion and advice. I am thankful to Dr. Naresh Murty, and Dr. John Provias for their kind supports in the clinical study of *ex vivo* brain tumour.

Furthermore, I also want to thank the people in the Biophotonics group in McMaster University to give me a wonderful experience through the years. Especially, I want to express my thank to Dr. Ran An and Jin Ning for their helps and instructions for system design. I would like to thank Derek Cappon and Du Le for their collaboration in this project. I also want to thank Allison Yeh, Anthony Tsikouras, and Dr. Samir Sahli for their discussion of the project and kind helps.

Finally, I would like to thank my parents and my brother for their selflessness support and love. I also want to thank my husband Haowen Ruan for his love, support, and encouragement. I cannot achieve anything without them.

Contents

List of Figures

List of Tables

List of Abbreviations

AOD:	Anaplastic oligodendroglioma
AOTF:	Acousto-optical tunable filter
CNS:	Central nervous system
CT:	Computed tomography
CLF:	Constrain Laguerre function
DE:	Diffraction efficiency
DR:	Diffuse reflectance
FAD:	Flavin-adenine dinucleotide
GBM:	Glioblastoma multiform
FWHM:	Full width half maximum
FLIM:	Fluorescence lifetime imaging microscopy
IRF:	Impulse response function
LED:	Light emitting diode
LEC:	Laguerre expansion coefficient
LSB:	Least Significant Bit
MCP-PMT:	Microchannel plate photo-multiplier tube
MRI:	Magnetic resonance imaging
NA:	Numerical aperture
NADH:	Reduced nicotinamide adenine dinucleotide
Nd:YAG:	Neodymium-doped yttrium aluminum garnet
OCT:	Optical coherence tomography
OLF:	Original Laguerre function
PET:	Positron emission tomography
PAT:	Photoacoustic tomography
PPIX:	Protoporphyrin IX
PBS:	Phosphate buffered saline
PTD:	Probe-target distance
RF:	Radio frequency
SNR:	Signal-to-noise ratio\
SVM:	Support vector machine
TRF:	Time-resolved fluorescence
TCSPC:	Time correlated single photon counting
TeO_2:	Tellurium dioxide

TTS :	Transit time spread
UV:	Ultraviolet
VIS:	Visible
5-ALA:	5-aminolevulinic acid

Chapter 1

Introduction

Tumours differ from normal tissue in many aspects including growth control, morphological change, cell-to-cell interaction, etc. [1]. Malignant tumours or cancers grow rapidly and may relocate to other organs. They cause significant damage to the organ's normal function and are life-threatening. According to the cancer statistics of National Cancer Institute, the incidence rate of primary brain and central nervous system (CNS) tumours was 19.89 per 100,000 persons per year in the United States during 2004-2008 [2]. The incidence rate of malignant brain tumours was 7.3 per 100.000 persons per year [2]. In Canada, brain tumor caused 1561 new cases and 1066 deaths in 2012 [3]. Although this rate is quite low compared to other cancers (*e.g.* 45 per 100,000 person-years for colorectal cancer [4]), primary brain tumours, especially malignant gliomas, have a devastating effect on patients' life. For example, the average survival time for the patients with malignant gliomas is about 14 months after diagnosis [5].

Surgery, followed by radiation therapy and/or chemotherapy, is the most commonly prescribed treatment for gliomas. It is shown that the prognosis of patients is directly correlated to the completeness of tumour removal during the surgery [5]. Due to the infiltrating characteristics of malignant gliomas, complete resection is difficult to achieve without removing healthy, functional normal tissue. Therefore, a surgeon needs to maintain the balance between removing as much tumour as possible and avoiding damage to essential brain functions. To achieve this balance, a technique capable of providing accurate real-time demarcation between tumour and normal tissue in neurosurgery is needed.

Some pre-operative diagnostic imaging methods such as magnetic resonance imaging (MRI), computed tomography (CT), and positron emission tomography (PET) are used to investigate the tumour's location and types. MRI observes the changes in the magnetic properties of tumour. CT detects the absorption rate of x-ray in the biological tissue, while PET detects the emission rate of gamma ray to reflect biological molecule's activity. However, it is still necessary to confirm the properties of the tumours during surgery. The current "gold standard" is invasive biopsy in which small pieces of tissue are removed by

a neurosurgeon from the area of interest. The specimens are then frozen, stained, and diagnosed under a microscope by a pathologist. This biopsy procedure is time-consuming and unable to provide real-time diagnosis. In addition, for brain tissue biopsy, only limited samples can be resected to avoid damages to normal tissue, which may lead to significant sampling error.

To overcome those problems that occur in the invasive biopsy, minimally invasive optical techniques, called optical biopsies, have been developed for intraoperative diagnosis in a number of applications [5-10]. The optical biopsy monitors the cellular structure and biological composition of biological tissue based on the interactions between light and tissue. Many single-point spectroscopies, such as fluorescence [6], Raman [7] and diffuse reflectance (DR) spectroscopy [8], have been investigated for clinical diagnosis. Some imaging modalities, such as optical coherence tomography (OCT) [9], photoacoustic tomography (PAT) [10], and fluorescent-based imaging [11], are also involved in many studies. With recent developments in fibre optic probe and endoscope techniques, it is feasible to translate these modalities from bench-top to bedside [12]. The light illumination and collection can be realized using a fibre probe/endoscope for the *in vivo* study without significant interference to the surgery. The optical biopsy has several advantages which make it much compatible for clinical studies: (a) it is a noninvasive or minimally invasive, (b) it provides rapid measurements that can lead to real-time diagnosis, (c) it is able to detect small tumours with high spatial resolution [13], and (d) it is able to detect precancerous conditions according to spectral characteristics that are associated with molecular changes [1].

In principle, the optical biopsy modalities that provide endogenous biochemical and morphological features are preferred in intraoperative applications over those that rely on exogenous contrast agents. Autofluorescence spectroscopy and DR spectroscopy [14] are two common non-contrast-agent-based modalities. Autofluorescence signals from the endogenous fluorophores in biological tissue highly correlate with the tissue's biological compositions and cellular structures. Time-resolved fluorescence (TRF) spectroscopy measures dynamic fluorescence signals such as fluorescence lifetime in addition to fluorescence spectrum [15]. TRF is particularly favored for *in vivo* diagnostic applications because fluorescence lifetime is independent of intensity variation artifacts common in *in vivo* measurements and is sensitive to microenvironment changes such as pH, ionization, and temperature [16]. A clinical study has demonstrated the feasibility of TRF spectroscopy to differentiate brain tumor from normal tissue [6]. DR spectroscopy is another minimally invasive optical biopsy method. In DR spectroscopy, a broadband light is measured at different source-to-detector distance via fibre optic bundles to estimate the

scattering and absorption properties of biological tissue. Typically, the scattering properties are related to the scattering size and structure of the biological tissue [17], while the absorption properties are related to the concentration of absorbers (oxygenated hemoglobin, deoxygenated hemoglobin) [18], both of which are importance diagnosis criteria [19].

1.1. Motivation

The autofluorescence and diffuse reflectance spectroscopy do not need exogenous contrast agents and can provide some unique features about biochemical composition, structure, and morphology of biological tissues. However, each technique has its limitation when applied to clinical studies. For example, autofluorescence spectroscopy is limited by the penetration depth of excitation light, such that it can only measure the autofluorescence signals from the surface layer of tissue about several hundred micrometers. In addition, autofluorescence signals are also altered by tissue's scattering and absorption properties. Therefore, the measured autofluorescence signals may not reflect the real information of endogenous fluorophores. Diffuse reflectance spectroscopy only provides the optical properties of the bulk tissue, but miss the biochemical composition details.

Fortunately, with current techniques advances, it is possible to combine multiple optical biopsy modalities for tissue diagnosis, thus providing extra contrast features to improve the diagnostic accuracy. By combining fluorescence spectroscopy and diffuse reflectance spectroscopy, a number of biochemical features (such as hemoglobin and oxygen concentration and tissue's metabolic status) and morphological features (such as scattering size, shape and density, as well as extracellular structures) can be used to differentiate tumours from normal tissue. In addition, the optical properties derived from diffuse reflectance spectroscopy can also be used to correct the distortion of the fluorescence signals measured at the same location. Therefore, the intrinsic fluorescence signal can be obtained to provide much accurate diagnostic results.

Combining steady-state fluorescence spectroscopy with DR spectroscopy has been shown a better discrimination results in many clinical studies, such as epithelial dysplasia diagnosis [19], breast surgical margin detection [20], and brain tumour discrimination [21-23]. Recently, TRF spectroscopy has also shown its ability to distinguish the brain tumour from normal brain tissue [6]. By taking the advantages of TRF and DR spectroscopy, the motivation of this study is to combine TRF and DR spectroscopy towards an intraoperative application to improve diagnostic accuracy of margin detection of brain tumour. To meet these requirements, some potential roadblocks appear when

applying these technologies to *in vivo* intraoperative tumour discrimination in neurosurgery.

(a) Intraoperative optical biopsy has challenging requirements for the clinical instrument. The clinical instrument needs to be compatible with the surgical procedure and sensitive enough to detect weak signals from biological tissue. Therefore, developing a clinically compatible system to collect TRF and DR signals with sufficient signal-to-noise ratio in real-time is one of the issues that is needed to be resolved.

(b) In order to assess the properties of tumour and normal tissue, it is important to retrieve the fluorescence properties (spectrum and lifetime) and tissue optical properties (scattering, absorption, and anisotropy) accurately and quickly from measured signals. Therefore, fast, accurate algorithms to quantitative retrieve these features are necessary. Moreover, the measured fluorescence signals are altered by the absorption and scattering effects in tissue; this leads to inaccurate diagnostic results. Therefore, retrieving the intrinsic fluorescence signal from turbid tissue is another question we need to solve.

(c) The relationship between TRF and DR features and the biological properties of brain tumour is still not clear, although a number of studies have been done in this area [6,21-23]. To investigate the TRF and DR characteristics of different brain tumours, large numbers of clinical cases are necessary. In addition, reliable classification methods also need to be developed to improve the sensitivity and specificity for tumour discrimination.

1.2. Dissertation overview

To overcome the limitations of existing intraoperative biopsy methods, the goal of this research is to develop a minimally invasive intraoperative optical biopsy method by combining TRF and DR spectroscopy for the quantitative diagnosis of brain tumours. To achieve this goal, four major milestones were achieved in this dissertation.

First, an integrated TRF and DR spectroscopy instrument was developed as an intraoperative tool. The fluorescence and DR spectra can be collected within 2 seconds to realize near real-time data collection. The system performance was calibrated and validated using tissue phantoms to ensure the accuracy of signal measurement.

Second, to accurately retrieve the fluorescence lifetime from the low signal-to-noise data obtained from biological tissue, Laguerre-based deconvolution method was optimized by using the physical properties of the fluorescence decay to constrain the fitting regression. Hence, the fitting accuracy is improved significantly compared to previous Laguerre deconvolution methods.

Third, to investigate the TRF and DR characteristics of brain tumour diagnosis, a pilot *ex vivo* study of brain tumours were investigated using TRF and DR spectroscopy with separated optical fibre probes individually. The spectral and lifetime features were selected to classify the different tissue types.

Finally, to solve the small detection tissue volume and slow data collection problems in the single-point spectroscopy measurements, a scanning-based hyperspectral fluorescence lifetime imaging application was developed. The performance was validated using tissue phantoms and biological samples [24].

1.3. Dissertation organization

This dissertation is organized according to the specific aims of this study:

In this introduction chapter, the motivation and milestones of this project are presented to give an overview of the dissertation.

Chapter 2 reviews the conventional diagnostic technologies as well as optical biopsy methods used as potential intraoperative tools in neurosurgery. The background of brain tumours, including meningiomas and gliomas, are presented in Section 2.1, and then followed by conventional intraoperative methods. A review of various optical biopsy methods are introduced in Section 2.3. Focusing on the research in this dissertation, fluorescence spectroscopy and DR spectroscopy are discussed in detail in Sections 2.4 and 2.5, respectively. In addition, a review of multi-modality optical biopsy methods is presented in Section 2.6.

Chapter 3 focuses on the integrated TRF-DR spectroscopy instrument that was developed as an intraoperative tool for brain tumour margin detection. The design of the clinically compatible TRF-DR spectroscopy instrument is described in Section 3.1. Section 3.2 presents details of system calibration methods and results, which ensure our system to collect time-resolved fluorescence and diffuse reflectance signals accurately.

Chapter 4 describes the performance of the integrated TRF-DR instrument using standard fluorescence dyes, biomolecules, and liquid tissue-simulating phantoms. Validation results show that our system is able to retrieve the fluorescence spectra and lifetime information from standard fluorescence dyes and biomolecules accurately. The effects of optical properties on fluorescence spectral and lifetime measurements were also investigated using different tissue phantoms. The results show that the fluorescence spectra are altered by the optical properties, whereas the fluorescence decay does not change with differences in optical properties when a single fiber is used for the fluorescence measurement.

Chapter 5 presents an optimized robust Laguerre-based deconvolution method to retrieve intrinsic response functions from measured fluorescence signals. This method overcomes the over-fitting problem that is introduced by high-order Laguerre functions and low signal-to-noise ratio. The theory of the robust Laguerre-based deconvolution is presented in Section 5.2. A series of Laguerre parameter selection methods is discussed in Section 5.3 to realize accurate, real-time data processing. the performance of the robust Laguerre algorithm is demonstrated in the simulation data and experimental results.

Chapter 6 describes a pilot *ex vivo* study of brain tumours using TRF and DR spectroscopy. The clinical procedure, including sample preparation and experimental data acquisition, is presented in Section 6.1. Data processing, feature selection, and classification methods are described in Section 6.2, and followed by the study results in Section 6.3. Several features including intensity ratios, lifetime values, and Laguerre coefficient ratios at different wavelengths were selected based on one-way ANOVA tests. The support vector machine (SVM) method was applied to classify the different tissue types. The results show that the meningioma grade I and grade II can be separated with both sensitivity and specificity of 100%.

Chapter 7 demonstrates a hyperspectral fluorescence lifetime imaging setup (FLIM) that was developed to acquire autofluorescence images for optical biopsy studies. An introduction of FLIM applications is presented in Section 7.1. The system configuration and tissue phantom preparation is shown in Section 7.2. The 2-dimensional images are acquired by scanning a fibre-optic probe using a translation stage. The system's performance was characterized and validated using standards fluorescence dyes and biological tissue. The results (Section 7.3) illustrate ability of the hyperspectral lifetime imaging system to resolve the different fluorescence signals from fluorescence dyes and biological tissue spatially, spectrally, and temporally.

In Chapter 8, the research of this thesis is summarized in Section 8.1 and discussion of future directions is presented in Section 8.2.

Chapter 2

Optical biopsies for neurosurgery

Brain tumour is considered as one of the aggressive tumour types. Currently, surgery is the main treatment for brain tumour, but is a risky procedure that requires removal of the entire tumour without causing damages to the nervous system. This chapter presents an overview of conventional techniques as well as optical biopsy techniques that are used to help the neurosurgeon to identify tumours in neurosurgery. The details of different brain tumours, including gliomas and meningiomas, are introduced in Section 2.1, and then followed by the conventional intraoperative diagnostic methods used in neurosurgery in Section 2.2. Section 2.3 introduces the promising diagnostic techniques of optical biopsies that provide minimally invasive, real-time, high resolution tumour detection. Focusing on this dissertation, time-resolved fluorescence (TRF) spectroscopy and diffuse reflectance (DR) spectroscopy are discussed in detail in Section 2.4 and 2.5, respectively. To improve diagnostic accuracy, combination of two- or multi-modalities is widely used in biological studies recently. A review of the clinical studies by combining fluorescence and diffuse reflectance spectroscopy is presented at end of this chapter.

2.1. Brain tumours

The annual incidence rate of the brain and central nervous system (CNS) tumours is 19.89 per 100.000 persons in the United States during 2004-2008 reported by the National Cancer Institute [2]. Gliomas and meningiomas are two common primary brain tumours. Gliomas account for 30% of all cases and 80% of malignant tumours, while meningiomas account for 35% of all cases [2]. In addition, glioblastomas are the main malignant tumour types, which account for 16% of all tissue types.

Gliomas originate from glial cells that are used to support and protect the nervous system in brain. Gliomas can be classified to astrocytoma, oligodendroglioma, ependymoma, or a combination of them based on their cell types. Anaplastic astrocytoma and glioblastoma are the main types of malignant gliomas [2]. In addition, gliomas can also be classified into grades I to IV based on their histopathological performances [25]. Grades I and II are classified as low-grade gliomas, which are usually non-malignant and can be treated. It has been shown that the 5-year survival rate of patients with grade II

astrocytomas is approximately 50% [2]. Grades III and IV are considered as high-grade gliomas which are diffusely infiltrative to the surrounding normal tissue and have high proliferative index. Thus, the histologic results usually show heterogeneity and have various characteristics from different samples [5]. Thus, the treatment of malignant gliomas becomes complex as they are very difficult to be removed completely. For example, the 5-year survival rate of glioblastoma multiforme is down to 4.7% [2].

Meningiomas arise from arachnoid cells in the meninges of brain and commonly occur in older adults with the median age about 65-year old [2]. The WHO classifies meningiomas into three grades based on the histopathological results [25]. Grade I is benign, which grows very slowly and accounts for 75% of all meningiomas. Grade II is atypical, which grows slowly but still can be malignant. Grade III is anaplastic, which grows very fast and is most likely malignant. Usually, meningiomas can be treated by surgical resection.

2.2. Traditional diagnostic methods

A surgical resection followed by chemo- and/or radiation therapy is the most common treatment strategy for malignant gliomas. Magnetic resonance imaging (MRI), computed tomography (CT), and positron emission tomography (PET) are commonly used in pre-operative diagnosis to obtain the information of tumour's locations and types. During neurosurgery, invasive biopsy is performed for histopathological analysis to further confirm the tumour types. Unlike other types of organs, it is challenging to find a distinct barrier between malignant tumour and normal brain tissue; hence, there is a greater risk in causing irreversible damage to the nervous system when excessive brain tissue is removed.

To improve the precision of the resection, some applications have already been used to help the surgeon determine the tumour margin, such as stereotactic image-guided surgery based on pre-diagnostic imaging, intraoperative ultrasound, and intraoperative magnetic resonance imaging (iMRI). Stereotactic image-guided surgery uses pre-operative diagnostic images co-registered with other imaging modalities such as microscopy and MRI to assist the surgeon in determining the location and size of brain tumour [26]. It can also provide anatomical information as well as pre-operative blood-brain-barrier leaks. However, one unfavorable limitation of this method is that it is very easy to lose the registration because of the brain-shifting during surgery [26]. Intraoperative ultrasound is another imaging technique that can be used in neurosurgery. It is not affected by the brain-shifting and provides subsurface structural images with high spatial resolutions (axial: 0.15-0.35 mm, lateral: 0.4-1.2 mm) and deep penetration depth (3-10 cm) [27].

This method can quickly determine the location of brain tumour and evaluate the completeness of tumour resection. However, low signal-to-noise ratio prevents its widespread use during surgery [27]. In contrast, iMRI is the most popular method used in neurosurgery, where the tumour structure can be identified in real-time with desirable signal-to-noise ratios and resolutions [28]. The requirement of proper magnetic shielding for certain surgical instrumentations, however, becomes a challenging issue on top of the cost of iMRI.

2.3. Optical biopsy

Optical biopsy has been proven as a promising diagnostic method as it probes tissue heterogeneity quickly based on changes in light-tissue interactions. Common methods used in optical biopsy include single-point spectroscopic techniques such as fluorescence, diffuse reflectance and Raman spectroscopy. Various imaging-based modalities have also been proposed, such as optical coherence tomography (OCT), photoacoustic tomography (PAT), and fluorescent-based imaging. In this section, principles and applications of these modalities are reviewed, and fluorescence and diffuse reflectance techniques will be further illustrated in detail in Section 2.4 and 2.5, respectively.

2.3.1. Raman spectroscopy

Raman scattering is an inelastic scattering process that results from the energy changes of the scattering molecule. The molecule is excited by an incident light from the ground state to a virtual state; then it relaxes back to a vibrational state by emitting photons. The vibrational state might have higher or lower energy level than ground state. Due to the difference of the energy between the ground state and vibrational state, the wavelength of emitted light can be shorter or higher compared to the wavelength of incident light. Therefore, there are two types of Raman scattering: (i) Raman stokes scattering in which the scattered photon has lower energy than the incident photon, which results in a longer wavelength emission; (ii) Raman anti-stokes scattering in which the scatted photon has more energy than the incident photon, thus resulting a shorter wavelength emission.

Raman spectroscopy has been used in the past few decades to detect the chemical components of samples based on their Raman scattering spectra. In other word, the distinct Raman spectrum of different molecules used to discriminate the chemical components in biological tissue; for example, the common biological molecules that contribute to Raman spectra include proteins, lipids, nucleic acids, and water [29]. In recent years, Raman spectroscopy has been investigated for brain tissue diagnosis by several groups [6, 28-30]. Koljenovic *et al*. reported a study of using Raman spectroscopy

to discriminate the vital tumours from necrotic tissue with 100% sensitivity [30]. As revealed by the Raman spectra, this study confirmed that the necrotic tissue contains higher concentration of cholesterol. Zhou *et al.* [7] used a confocal micro-Raman system to investigate resonance Raman spectra on six types of brain tissues *in vitro.* This study showed that an increased intensity ratio of 1587 cm^{-1} and 1605 cm^{-1} was observed in meningioma compared to benign and normal meningeal tissue, which provides the sensitivity and specificity of 90.9% and 100% respectively.

2.3.2. Optical coherence tomography

Optical coherence tomography (OCT) based on low coherence interferometry was first described by Huang *et al.* [33]. In the OCT system, a low coherence light is split into the reference and the sample arms. Scattering light from the sample at different depths is collected and mixed with the reference light at the detector to generate an interferometry pattern. Because the temporal coherence of the light source is low, a well-defined interference pattern will be generated only if the path difference between sample arm and reference arm is within the coherence length of light source. Therefore, the reflected scattering light at specific depths can be measured by changing the path-length of the sample arm. This technique is able to obtain images of the sub-layer structure of the biological tissue by measuring the optical reflectance and scattering [33].

OCT can provide sub-micrometer-resolution, real-time, and non-invasive imaging of biological tissue. Moreover, optical fibre-based instrument makes this technique much more compatible with clinical application such as endoscopy and catheter based studies. It has also been applied as an intraoperative technique for neurosurgery. Boppart *et al*. [34] evaluated the feasibility of OCT as an intraoperative imaging tool to identify intracortical melanomas. In this study, a hand-held OCT surgical imaging probe was used to obtain two- or three-dimensional images. The results showed that the optical backscatter increased in the tumour region. This can be used to determine the tumour margin accurately as it correlates well with histological results.

2.3.3. Photoacoustic tomography

Photoacoustic tomography (PAT) has also been used in imaging biological tissue in the last decade. The imaging contrast of PAT is based on the ultrasonic detection of thermal expansion from biological composition, such as hemoglobin and melanin [13]. In particular, photothermal effect is caused by optical absorption after a short-pulsed laser illuminates biological tissue. Consequently, the thermoplastic expansion from the temperature increase (ΔT) at the illumination area results in a raised pressure that can be expressed by $p_0 = \beta \cdot \Delta T / k$, where β is the thermal expansion coefficient and k is the

isothermal compressibility [13]. After the pressure travels through the tissue, this pressure wave is detected by ultrasonic transducer(s) to form a high-resolution image that is related to the optical absorption of biological composition such as hemoglobin and melanin [13].

Photoacoustic tomography has been widely used to image from the cellular level to organ specimens with the use of certain contrast agents [13]. An *in vivo* case reported by Kircher *et al*. used PAT, MRI and Raman spectroscopy to investigate the brain tumour margin in a mouse model [35]. In this study, PAT produced a three-dimensional image to localize the position of brain tumour using a nanoparticle contrast agent, thus yielding an improved accuracy in tumour detection.

2.4. Fluorescence spectroscopy

When a biological molecule is illuminated by a light source with proper wavelengths that match its absorption spectrum, it is activated from the ground state (S_0) to excited states (S_1 or S_2) as shown in the Jablonski diagram (Figure 2-1). The molecule at the higher excited state (S_2) is back to the low excited state (S_1) nonradiatively by vibration relaxation and internal conversion. In contrast, fluorescence emission is a radiative process when a molecule releases its energy and drops back to its ground state, which happens in the time scale of nanoseconds. Several parameters are used to characterize the fluorescence phenomenon of the molecule (fluorophore) including emission spectrum, quantum yield, and fluorescence lifetime. The emission spectrum of a fluorophore has a red-shifted wavelength relative to the excitation light, but is independent from the excitation wavelength. Quantum yield is the ratio between the emitted photons and absorbed photons of the molecule, which is highly related to the molecular structure and microenvironment. Fluorescence lifetime is the average time a biological molecule spends in the excited state before it returning to the ground state. Usually, for the fluorescence emission of a single fluorophore, the fluorescence decay can be described as an exponential function:

$$I(t) = A\, exp(-t/\tau) \tag{2.1}$$

where A is the intensity at the time 0 and τ is the fluorescence lifetime, which is calculated from the time it takes for the intensity to decrease to 1/e of the peak intensity. For a complex fluorescence emission contributed by several fluorophores, the fluorescence decay can be presented as the sum of the exponential components of each fluorophore as:

$$I(t) = \sum_{i=0}^{N} A_i \exp(-t/\tau_i)\,, i = 1..N \tag{2.2}$$

where i represents the i^{th} fluorescence component. The average lifetime of the complex fluorescence decay can be calculated using its statistic definition:

$$\tau_{average} = \frac{\sum_{t=0}^{\infty} tI(t)}{\sum_{t=0}^{\infty} I(t)} \quad (2.3)$$

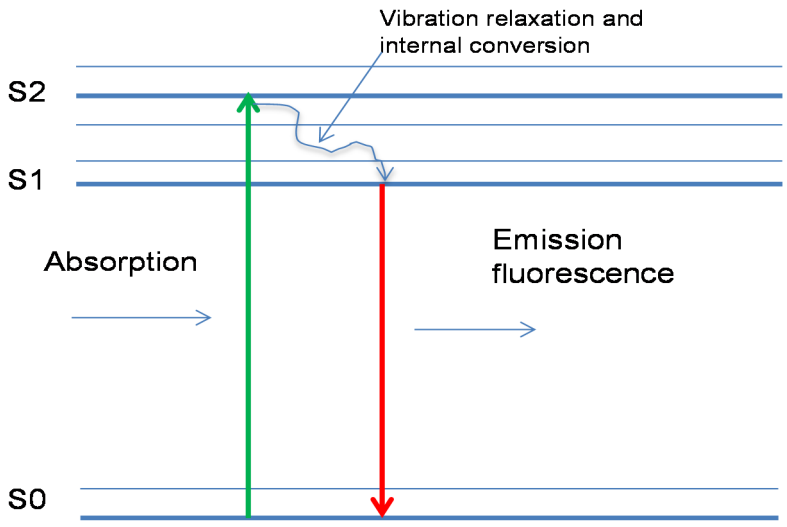

Figure 2-1. Jablonski diagram of fluorescence emission.

Fluorescence techniques have been used extensively in cellular and tissue studies to monitor the changes of biochemical composition, reaction, and structure. Both endogenous fluorescence and exogenous fluorescence are used in these studies. The following sections describe the properties of endogenous and exogenous fluorescence and their detection methods, as well as the clinical applications.

2.4.1. Endogenous fluorescence in biological tissue

Endogenous fluorophores such as amino acids (tyrosine and tryptophan), structural proteins (elastin and collagen), and enzyme cofactors [*e.g.* reduced nicotinamide adenine dinucleotide (NADH) and flavin-adenine dinucleotide (FAD)] exhibit great potential to monitor tumour environments because of their proportional changes during the alternation of biochemical composition, cellular structure, and tumour metabolism. For example, an increase of NADH concentration is found in tissue with higher metabolic activities. Because NADH emits fluorescence in the spectral range of 400-700 nm with UV radiation; whereas the oxidized form (NAD+) is non-fluorescent. A change of autofluorescence emission intensity then offers a good contrast for tumour detection. In addition, NADH exhibits short and long lifetime components depending on its binding status with proteins. The ratio change of free to bound NADH in cancer results in

changes of the average lifetime of NADH [36]. Thus, the intensity and lifetime of NADH become potential indicators to monitor tumour's environment. Most endogenous fluorophores can be excited by UV-VIS light (280-450 nm) and emit fluorescence in range of 370-700 nm as shown in Figure 2-2. The fluorescence lifetime values of endogenous fluorophores are in the range of 0.5-6 ns [36]. Detailed properties of endogenous fluorophores properties are summarized in Table 2-1.

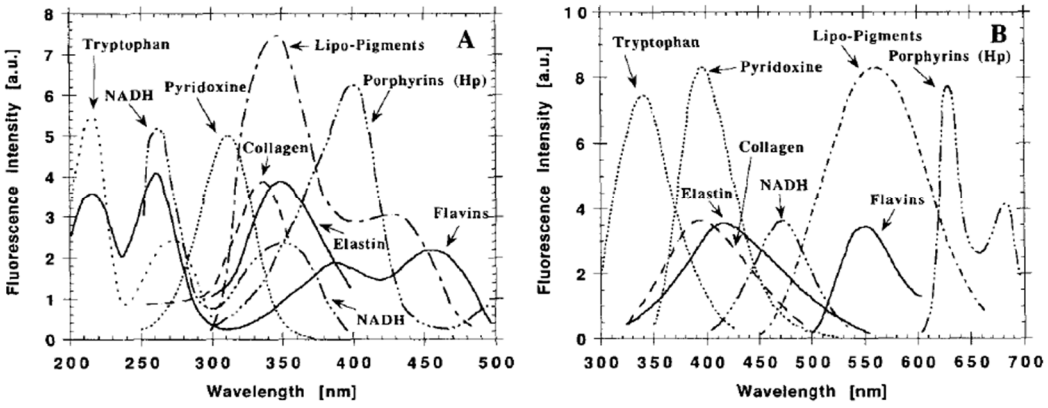

Figure 2-2. The fluorescence excitation (a) and emission (b) spectra of selected endogenous fluorophores in tissue. (Adapted from the Ref [37])

Table 2-1. Summary of endogenous fluorophores' properties [38-40]

Fluorophores	Excitation peak (nm)	Emission peak (nm)	Lifetime (ns)	Quantum yield	tissue types
Amino acid					
Tryptophan	280	350	0.5~2.8	0.2	All proteins
Tyrosine	275	300	3.6	0.1	All proteins
Phenylalanine	260	280	6.4	0.04	All proteins
Structural proteins					
Collagen	325,360	400, 405	3		Skin
Elastin	290,325	340, 400	2.7		Skin
Enzymes /coenzyme					
NADH	340	450	0.4-2.8	0.4-0.69	All cells
FAD/FMN	370/440	510-520	2.3-5		Brain, liver
Vitamin					

Pyridoxine	332,340	400		0.03	Liver, brain, kidney
Pyridoxamine	335	400	0.11	0.18	Liver, brain, kidney
Lipids					
Phospholipids	436	540,560			
Lipofuscin	340-395	540-640, 430-460	1.5		Brain
Ceroid	340-395	540-640, 430-460	2		Vessel
Lipopigments	340-395	430-460,540	1.5	NA	Brain

2.4.2. Exogenous fluorescence

Exogenous fluorophores including indocyanine green (ICG), 5-aminolevulinic acid (5-ALA), and fluorescein have been used as contrast agents for brain tumour margin detection. 5-ALA is one of the FDA-approved photosensitizers used in photodynamic therapy and tissue diagnosis. It is a prodrug that is converted to protoporphyrin IX (PpIX) via heme synthesis pathway [11]. PpIX is an endogenous fluorophore that is normally converted to heme through the enzyme, ferrochelatase. How, with the reduced ferrochelatase activities in tumour, the PpIX will be easily accumulated with the application of exogenous 5-ALA. Therefore, high levels of PpIX can be detected by the fluorescent-based techniques [11].

2.4.3. Fluorescence measurement methods

Both steady-state fluorescence spectroscopy and time-resolved fluorescence spectroscopy techniques have been used to monitor the fluorescence variation in many clinical studies. Steady-state fluorescence spectroscopy measures the fluorescence intensity in a broadband spectral region, whereas time-resolved fluorescence spectroscopy measures the dynamic fluorescence decay to obtain the fluorescence lifetime features in addition to the intensity measurement. Time-resolved fluorescence spectroscopy, in particular, provides additional information in optical biopsy due to the following advantages: (1) fluorescence lifetime is independent of the emission, thus it can be used to differentiate the fluorescence components with overlapped fluorescence emission spectra; (2) fluorescence lifetime can be easily changed when the energy of the molecule is absorbed by its surrounding. In other words, it becomes sensitive tool to probe the changes in microenvironment (*e.g.* pH, ionization, and temperature). Therefore, time-resolved fluorescence spectroscopy is renders additional contrast upon steady-state

fluorescence techniques.

In terms of the instrumentation, steady-state fluorescence spectroscopy is relatively simple, which usually includes a narrow band light source (laser or LED) and a grating-based spectrometer to collect the fluorescence emission. On the contrary, time-resolved fluorescence spectroscopy is much more complex, where the fluorescence decay signals need to be collected with picosecond temporal resolution. A short-pulsed laser is generally used as an excitation light in the time-domain measurement, whereas a modulated light source is used in frequency-domain measurement. To date, several time-domain applications have been used in clinical studies based on different data acquisition methods [15].

(a) Time-correlated single-photon counting (TCSPC)-based detection

TCSPC is the most common technique to detect fluorescence signal of a fluorophore. In the TCSPC system, a pulsed laser with high repetition rate (*e.g.* 80 MHz) is used to excite the fluorophore, and only the single photon that reaches the detector first is captured after each excitation. A histogram of the photons with respect to their arrival time is generated after multiple excitations, thus, the profiles of fluorescence decay can be retrieved from this histogram. This method has high sensitivity and resolution, such that it can detect the weak autofluorescence signals from biological tissue. It has been used extensively in cellular or *ex-vivo* tissue studies. However, the data acquisition time is relatively long, which limits its application as intraoperative tool in surgery.

(b) Time-gated detection

Time-gated detection provides an alternative method to detect the weak fluorescence signal in time-domain. In this method, the sample is excited by a short-pulsed laser. The fluorescence emission at different times along the fluorescence decay are detected by an imaging detector with a fixed gating time (*e.g.* 200 ps), and then are used to reconstructed the decay curve in time-domain. Time-gated intensified charge-coupled device (ICCD) is the typical device used in such measurement. This method is suitable to obtain the image for a large spatial area. However, the temporal resolution and the sensitivity are relatively low.

(c) Pulse-sampling-based detection

With the development of high-speed digitizer, it is possible to acquire short fluorescence decay in picosecond or nanosecond temporal resolution using a high-speed digitizer. After the sample is excited by a laser pulse, fluorescence decay signal is detected by a point detector such as PMT or avalanche photodiode, and then digitized by a high speed digitizer. The fluorescence decay signal can be acquired right after each

laser excitation in real-time. However, the temporal resolution of fluorescence signal is limited by the sampling rate of digitizer.

(d) Streak camera based detection

Streak camera is a fast photo-detector that uses time of flight to measure light intensity changes as a function of time. It operates by dispersing the photoelectrons across an imaging screen. Therefore, the photons arriving at the streak camera at different times are detected at different positions. By using streak camera, multiple decay curves can be measured simultaneously with high temporal resolution of several picoseconds. However, the sensitivity is still lower than that of TCSPC.

Considering the feasibility of these methods towards clinical studies, the advantages and disadvantages of each method are summarized in Table 2-2. In summary, the TCSPC method can provide the best sensitivity and temporal resolution. However, long acquisition time and high instrumentation costs limit its broad applications in clinical studies. On the contrary, time-gated- and pulse-sampling-based methods are much more feasible for clinical applications due to their fast data acquisition speed and affordable instrumentation costs.

Table 2-2. Comparison of time-resolved fluorescence measurement methods

Method	Advantage	Disadvantage	Prices
TCSPC	• High sensitivity • High temporal resolution • Low system error	• Slow data acquisition	• $$$$
Time-gated	• Fast data acquisition • Simultaneous acquisition for imaging	• Low sensitivity	• $$
Pulse-sampling	• Fast data acquisition • High intensity	• Limited time resolution • Large system error	• $
Streak camera	• High resolution • Fast data acquisition	• Low sensitivity	• $$$

To date, both single-point spectroscopy [16,42,43] and imaging system [44-47] have been developed for tissue diagnosis. In single-point measurements, a fibre optic probe is used to deliver laser light and collect fluorescence signal, which makes the TRF spectroscopy much more compatible with clinical studies. In imaging measurements, a single fibre or fibre bundles are used to collect the image in the wide-field-based FLIM [44,46], whereas high speed scanning modules such as galvanometer mirrors are used in scanning-based FLIM [47], Recently, video-frequency-based fluorescence imaging

systems were reported to provide near real-time fluorescence lifetime monitor [48,49].

2.4.4. Clinical studies for brain tumours

Both steady-state and time-resolved fluorescence techniques have been investigated extensively for brain tumour diagnosis in the past decades. A brief review of fluorescence applications of brain tumour studies is presented in this section.

For steady-state autofluorescence spectroscopy, NADH and FAD are two main endogenous fluorophores that were investigated in brain tissue. Usually, the emission intensity ratio of these two fluorophores is used to discriminate tumour from normal tissue. Chung *et al*. [50] reported an *ex vivo* study that the gliomas had lower autofluorescent intensity than normal brain tissue when using different excitation lights in the spectral range of 360-490 nm. They also found that both fluorescent intensities of NADH and FAD were lower in all kinds of tumours than in normal tissue, but the ratio of NADH to FAD fluorescence intensity was not significantly different between the tumours and normal tissue. Another *in vivo* brain study has been investigated by Lin *et al*. [21] using the combination of fluorescence and diffuse reflectance spectroscopy. This study obtained a sensitivity of 100% and a specificity of 76% when discriminating brain tumours from normal tissue. Corce *et al*. [51] also investigated the autofluorescence properties of neoplastic and normal brain tissue using *ex vivo* tissue sections and homogenates. It was found that the fluorescence intensity ratio of 520 nm and 470 nm in glioblastoma is higher than that in normal tissue by using a 360 nm excitation light. This indicates that oxidized FAD and lipopigment increase in the neoplastic tissue compared to the normal sample. Lately, Lin *et al*. [22] also used multiple excitation wavelengths (337 nm, 360 nm, and 440 nm) to differentiate pediatric neoplastic and epileptogenic tissue from normal tissue. Their study found statistically significant differences (P value $<$ 0.05) between neoplastic brain tissue and normal gray/white matters. Moreover, Liu *et al*. [52] aimed to analyze the redox ratio, the intensity ratio of FAD and NADH, for brain tumours in a rat brain model. The results suggested that the fluorescence intensity ratio of different wavelengths can be used as a feature for brain tissue discrimination.

The initial TRF spectroscopy study of *ex vivo* brain tumours was reported in Ref [53], in which the fluorescence lifetime of glioblastoma was found longer than that in normal white matter and cortex. In a later *ex vivo* study, the fluorescence lifetime features of low-grade and high-grade gliomas have been investigated [54]. This study found the low-grade gliomas had faster decay than high-grade gliomas at the emission wavelength of 460 nm. Another *ex vivo* study by Butte *et al*. [55] analyzed meningiomas using the TRF spectroscopy. Their results showed that the meningiomas have different fluorescence spectral intensities and lifetime values from normal dura and cerebral cortex.

By using both spectral and time-resolved features, the meningiomas can be distinguished with the high sensitivity and specificity of 89% and 100% respectively. Lately, two *in vivo* clinical studies were reported by Butte *et al*. [6, 56]. These studies showed that the low-grade gliomas had distinct fluorescence emission characteristics from the normal cortex and white matter, whereas fluorescence characteristics varied with different high-grade gliomas types. Their study also showed that both spectral and time-resolved features varied not only with the tumour phenotypes, but also with the location of examination spot due to the heterogeneity of tumour. With a combination of spectral and lifetime parameters, the low-grade gliomas could be distinguished from other tissue types with 100% sensitivity and 98% specificity. On the contrary, high-grade gliomas were distinguishable with 47% sensitivity and 94% specificity. Sun *et al*. [45] demonstrated the feasibility of using fluorescence lifetime imaging microscopy (FLIM) in glioblastoma multiforme diagnosis using a fibre bundle and a gated intensifier imaging system. The clinical results showed that FLIM was able to differentiate tumour from normal cortex at the emission wavelength of 460 nm.

The exogenous fluorescence has been widely used in brain tumour during the neurosurgery worldwide. Stummer *et al*. used 5-ALA as a contrast agent to identify the resection margin of brain tumour during neurosurgery in several clinical studies [57-59]. The results suggested that the completely resection rate improved when using the 5-ALA compared to that without the 5-ALA [57]. Valde *et al*. [60] investigated the 14 patients with different tumour types using a fluorescence imaging modality to determine the PpIX concentration generated in different types of brain tissue quantitatively. The results indicated a significant difference in the PpIX concentration generated in tumour compared to the normal tissue, which may be used as a criterion for intraoperative diagnosis. Pogue *et al*. [11] have also presented a detailed review of 5-ALA application of tumour detection in neurosurgery.

2.4.5. Limitations of fluorescence spectroscopy

A challenge for the TRF technique is the limited penetration depth of excitation light. Typically, an UV light as an excitation source only has a penetration depth of several hundred micrometers. Consequently, only the fluorescence signal from the surface of tissue is measured using the TRF technique. Thus, this technique is much more preferred to detect the molecular changes on the tissue surface layer; it cannot give any depth information that is necessary for surgical resection. The multi-photon excitation at the near infrared wavelength conquered this problem to increase the depth of detectable fluorescence [61]. However, the instrumentation of the multi-photon method is very complex and expensive. Hence, this limits its application for clinical studies. In addition,

as the laser excitation light and fluorescence emission pass through the turbid tissue, they are altered by the absorption and scattering of tissue and blood. In other words, the fluorescence signal collected from the biological tissue may not reflect its real fluorescence properties. To retrieve the intrinsic fluorescence emission, diffuse reflectance spectroscopy is a common technique used to estimate optical properties of biological tissue.

2.5. Diffuse reflectance spectroscopy

2.5.1. Optical properties

When a biological tissue is illuminated by an incident light, typical light-tissue interactions include scattering and absorption events. Tissue heterogeneity can be studied by quantifying the scattering and absorption properties. For example, the scattering properties reflect the molecular size and structure of tissue whereas the absorption properties reflect the concentration of absorbers (*e.g.* oxygenated hemoglobin, deoxygenated hemoglobin) that further stands for angiogenesis of the vasculature, which are all considered as important criteria for diagnosis.

Detailed explanations of how light interacts with tissue as well as the optical properties of human tissue have been described by Cheong *et al.* [62] Scattering phenomena is induced by the mismatch of the refractive index occurring at microscopic boundaries such as cell membranes and intracellular structures. The scattering coefficient (μ_s), the probability of a scattering event per unit path length, is used to describe the scattering properties of measured target. In biological tissue, the distribution of scattering event does not depend on the original direction prior to scattering, and thus it has to expressed as a function of the angle between the directions of the incident and scattered light. The angular dependence of scattering distribution can be described by the anisotropy factor $g = \int_{-1}^{1} \cos\theta \cdot f(cos\theta) \cdot d(cos\theta)$, which is in the range of -1 to 1, where forward and backward scattering are represented by g equals to 1 and -1 respectively, while the anisotropy factor in isotropic scattering is 0. In general, light in biological tissue is strongly forward scattered in the visible and near-infrared spectral range. Typically, the scattering coefficients of biological tissue is in the range of 10-50 mm^{-1}, and g is in the range of 0.6-0.97 [62].

The absorption coefficient (μ_a) can be calculated by the inverse of distances of two absorption events. Chromophores, including oxygenated hemoglobin, deoxygenated hemoglobin, protein, and melanin, are the main absorbers in the biological tissue. The wavelength region between 800 nm and 1100 nm is known as the “optical window” due

to the relatively low absorption level in this region. Although scattering events dominate in the visible and NIR range, the significant attenuation of light due to hemoglobin absorption cannot be neglected in clinical studies.

2.5.2. Diffuse reflectance spectroscopy

Diffuse reflectance (DR) spectroscopy is a minimally invasive method that is used to measure the optical properties of biological tissue. Usually, a broad band light is incident on the tissue surface perpendicularly via an optical fibre as shown in Figure 2-3. After several scattering and absorption events, the light transmits in various directions, and escapes from the tissue surface at different positions. This diffused reflectance light can be collected by the optical fibres placed on the tissue surface near the original delivery location. Generally, small source-detector distances are preferred because this geometry provides the best sensitivity to the details of light scattering properties in the cellular level. In addition, small source-detector configuration is easy to realize by using a fibre optic probe that is highly compatible with *in vivo* clinical studies. The optical properties of measured tissue can be estimated from diffused reflectance spectra by using diffuse theory [63] or Monte Carlo simulation [64,65]

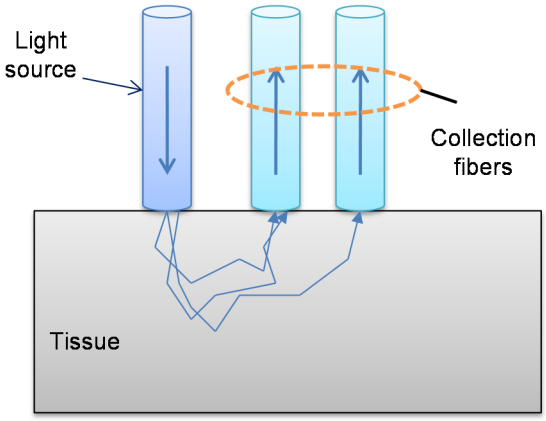

Figure 2-3. Diagram of diffuse reflectance spectroscopic measurement

2.5.3. Clinical studies for brain tumours

Brain tumour is known as a highly scattered medium, thus it is necessary to perform precise estimations of light-tissue interactions to improve the detection accuracy. Optical properties for different types of brain tissue, including normal cortex, normal white matter, astrocytoma, and meningioma, were presented in Ref [8]. Diffuse reflectance spectroscopy has been used to investigate the optical properties of brain tumour in many *ex vivo* and *in vivo* clinical studies. Johns *et al*. [65] used the scattering spectroscopy to locate the border of globus pallidus in Parkinson's disease. The globus pallidus is a

structure composed of gray matter surrounded by white matter. Clinical results showed that the gray matter had lower reflectance intensity than the white matter in the wavelength range of 650 nm to 800 nm. Thus, the globus pallidus boundary could be well distinguished based on diffuse reflectance measurement. Lin *et al*. [67] reported an *in vivo* case to demonstrate the feasibility of using diffuse reflectance spectroscopy in differentiating pediatric neoplastic from normal brain parenchyma. This study demonstrated that certain brain tumours could be effectively distinguished from the normal tissue using the diffuse reflectance intensity in the spectral range of 600-800 nm.

2.6. Multi-modality optical biopsy for clinical studies

Even though each aforementioned modality has the potential to differentiate tumour from normal tissue, neither of them can be used a "standard" tool. Improvement in measurement and data analysis is still required to achieve desired performance for clinical applications. On the other hand, information acquired from multi-modality optical biopsies may be able to complement the drawback of each single modality. A combination of steady-state fluorescence spectroscopy and time-resolved fluorescence spectroscopy has been used in several clinical studies. By combining these two modalities, the fluorescence features (*e.g.* metabolic status, cellular structures) and optical properties (*e.g.* scattering size and density, hemoglobin absorption) can be used to investigate the measured biological tissue. This will help us to study the differences between different tissue types. Lin and his coworkers demonstrated the feasibility of the dual-modality in determining the brain tumour types [21-23, 68]. These studies illustrate that it is possible to higher contrast for tissue diagnosis using multi-modality optical biopsy. Moreover, several clinical instruments of combining spatially resolved diffuse reflectance spectroscopy and steady-state fluorescence spectroscopy have been proposed by several groups [68-77]. Optical properties can be calculated using the diffuse reflectance measurement. Based on the optical properties of biological tissue, it is possible to estimate the distortion of fluorescence excitation light and emission light, thus retrieving the intrinsic fluorescence signals. Several methods have been developed to solve this problem. Wu *et al*. [78] and Műller *et al*. [79] developed a diffuse theory-based method to retrieve the intrinsic fluorescence spectra. In this method, the same source and detection fibres were used to measure the fluorescence and diffuse reflectance signals in sequence. Afterwards, the diffuse reflectance signal can be used to estimate the fluorescence transmission in the tissue. Kim *et al*. [80] further developed a simplified method based on the diffuse theory to retrieve quantitatively fluorescence signal using diffuse reflectance measurement. Vishwanath *et al*. [81-83] developed several models based on the Monte Carlo simulation to investigate the intrinsic fluorescence emission of a double layer

turbid tissue.

2.7. Discussion

Intraoperative diagnostic method is urgently needed to help the surgeon to identify tissue types during neurosurgery. Optical biopsy is a minimally invasive tool that provides contrast to differentiate tumour and normal tissue base on their biochemical and morphological features. Fluorescence and diffuse reflectance spectroscopy are two common methods that have been investigated for brain tumour diagnosis. Thus, combining time-resolved fluorescence and diffuse reflectance spectroscopy may also improve the diagnostic accuracy of brain tumour margin detection. As shown in Figure 2-4, the fluorescence signal, including intensity and lifetime, can provide the variation of biochemical composition as well as the binding status of biological molecules, while optical properties can be used to estimate the tissue morphological features such as the scattering size, density and chemical concentrations such as oxygen absorption. In addition, combining two modalities together can also help us to retrieve the intrinsic fluorescence spectral and lifetime features of the biology tissue to improve the diagnostic accuracy.

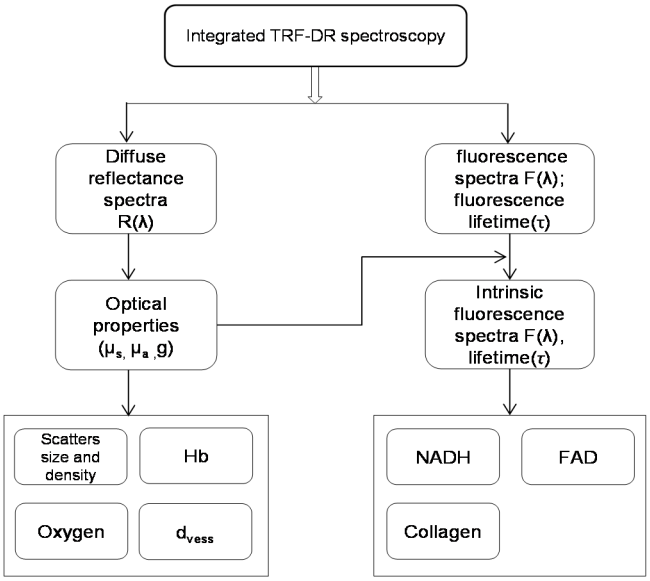

Figure 2-4. The flow chart of the combination of time-resolved fluorescence and diffuse reflectance spectroscopy.

In the next chapter, we will focus on the integrated system of time-resolved fluorescence and diffuse reflectance spectroscopy for optical biopsy.

Chapter 3

Integrated time-resolved fluorescence and diffuse reflectance spectroscopy instrument for optical biopsy

Both time-resolved fluorescence (TRF) and diffuse reflectance (DR) spectroscopy have been investigated extensively as minimally invasive clinical tools to discriminate tumour from normal tissue. TRF spectroscopy measures the changes in fluorescence intensity and lifetime of endogenous fluorophores, which are correlated with the changes of biochemical composition and structures of biological tissue. DR spectroscopy provides optical properties that reflect the scattering size, density as well as the absorber concentration of tissue. Combining these two modalities allows us to obtain more contrast features, thus potentially improving the diagnostic accuracy.

An integrated TRF and DR (TRF-DR) spectroscopy instrument was developed for optical biopsy studies. The detailed configurations of this clinically compatible TRF-DR spectroscopy instrument are described in Section 3.1, and calibration results of this system are presented in Section 3.2.

3.1. Integrated TRF-DR spectroscopy system

A schematic of TRF-DR spectroscopy system is illustrated in Figure 3-1a. The integrated system consists of four modules: the TRF subsystem, the DR subsystem, the dual-modality fibre optic probe, and the control unit. The TRF subsystem uses an acousto-optic-tunable-filter (AOTF) -based spectrometer to collect dynamic fluorescence decay signals and uses a grating-based spectrometer to collect steady-state fluorescence spectra. The DR subsystem collects spatially resolved diffuse reflectance spectra in a small tissue volume. The four-meter length clinical sterilizable fibre optic probe is used to deliver illumination light and to collect TRF and DR signals. Photographs of TRF-DR spectroscopy instrument housed in a mobile cart (L×W×H: 32 × 24 × 50 inch) and the

dual-modality fibre optic probe are shown in Figure 3-1b and Figure 3-1c respectively. During clinical studies, autofluorescence and diffuse reflectance signals are collected in sequence within 2 seconds.

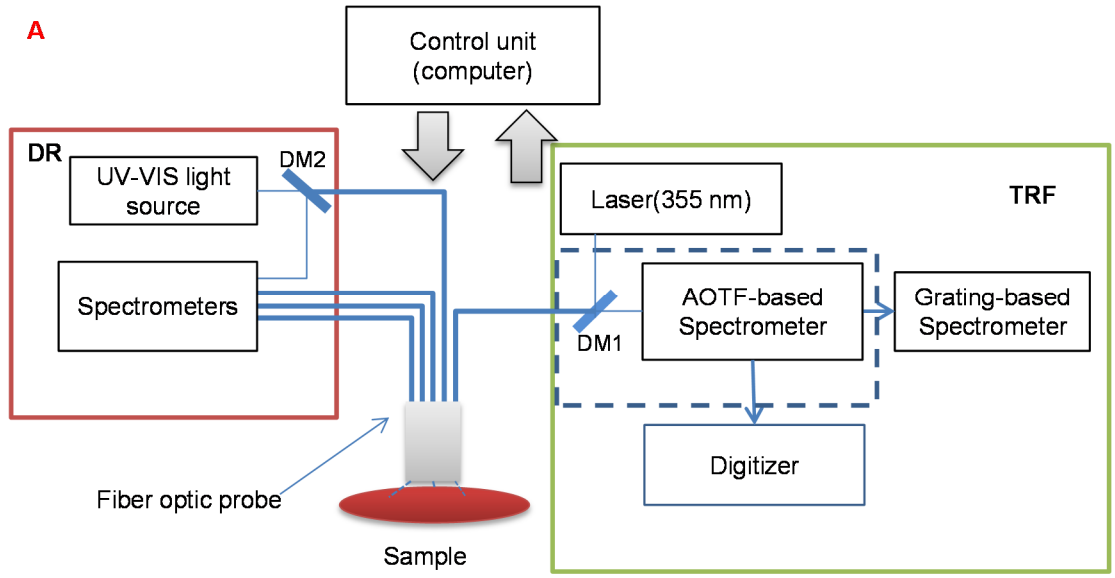

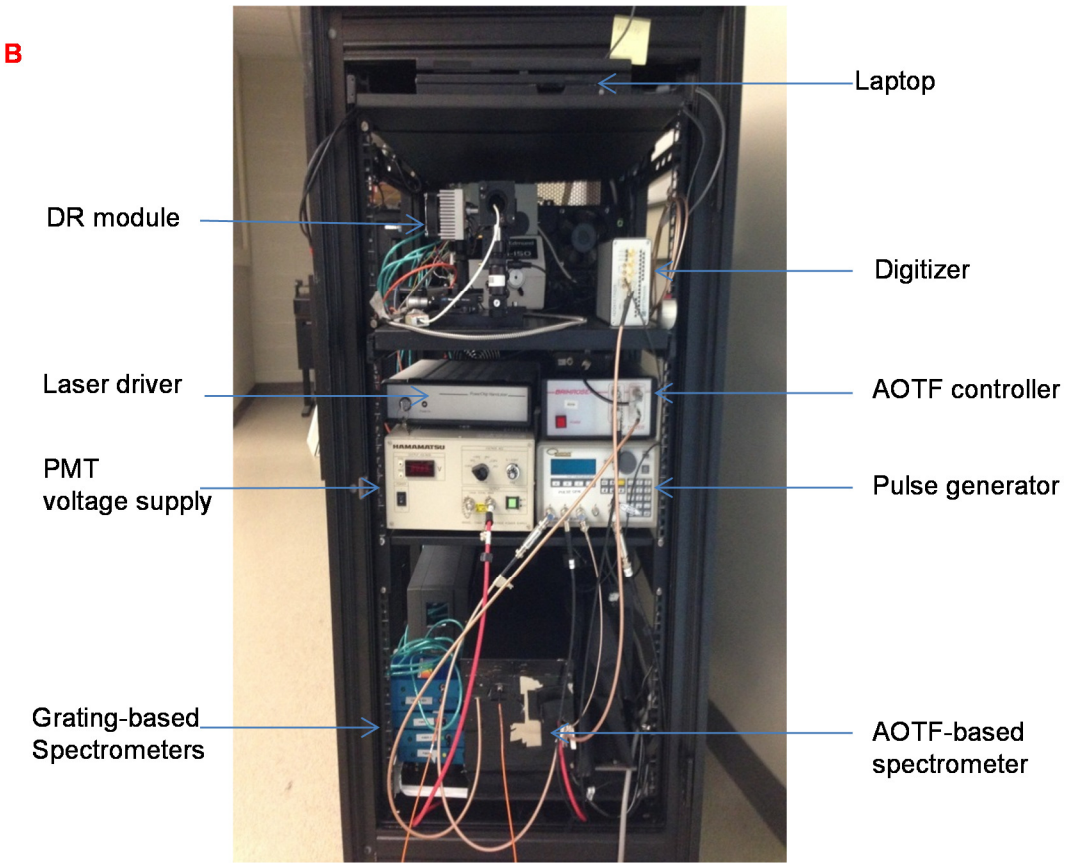

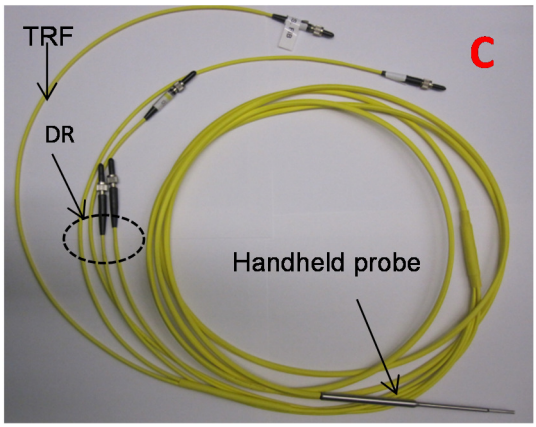

Figure 3-1. Integrated TRF-DR spectroscopy system. (a) Schematic view of the TRF-DR spectroscopy instrument that consists of four modules: the TRF subsystem, the DR subsystem, the dual-mode clinical fibre probe, and the control unit. (b) TRF-DR spectroscopy instrument housed in a mobile cart, making the system compatible with clinical studies. (c) Dual-modality clinical sterilizable fibre optic probe that is used to collect TRF and DR signals from the same tissue volume.

3.1.1. TRF spectroscopy subsystem

A schematic of the TRF subsystem is shown in Figure 3-2. An Nd:YAG laser (PNV-001525-140, Teem Photonics, Meylan, France) at 355 nm with 300 picoseconds (ps) pulse width [full width at half maximum (FWHM)] and 1 kHz repetition rate is used as the excitation light source. The laser beam is attenuated by a neutral density filter [optical density (OD):0.3, ND03A, Thorlabs, NJ] and a custom-made dichroic mirror (CS0238, Lightwaves 2020 Inc, Milpitas, CA) with 70 % reflection at 355 nm at 45˚ incident angle. The laser beam is then focused into the proximal end of a fused silica optical fibre with core diameter of 400 µm and numerical aperture (NA) of 0.12 by a plano-convex lens (LA1951-A, Thorlabs, Newton, NJ). The laser pulse energy illuminated on the sample was adjusted to ~3 µJ to avoid photobleaching.

After laser excitation, fluorescence light is collected by the same optical fibre and is then collimated by the plano-convex lens to a 6 mm diameter beam. An aperture of 6 mm is mounted after the plano-convex lens to block dispersed fluorescence light. The fluorescence beam is transmitted through the dichroic mirror (transmission >90% at 370 to 550 nm) and a long-pass filter (OD > 6 at 355 nm LP02-355RU-25, Semrock, Rochester, NY) to block the backscattered laser light before it is incident on the AOTF (TEAF5-0.36-0.52-S, Brimrose, Baltimore, MD). A selected spectral band of the collimated fluorescence beam is separated into ordinary and extraordinary polarized light, and diffracts toward two concave mirrors respectively. The undiffracted light passes through the AOTF and is blocked by a beam stop. Both diffracted beams at the opposite

sides of the undiffracted beam are detected by a fast-gated microchannel-plate-photomultiplier-tube (MCP-PMT R5916-50, rise time: 180 ps, Hamamatsu Photonics, Japan). The output signal from the MCP-PMT is amplified with a preamplifier (gain: 63 dBm, bandwidth: 50 KHz-1.5 GHz, C5594-12, Hamamatsu Photonics, Japan) and then digitized by a high speed digitizer (ADQ412, 12 bit, 3.6 GS/s, 1.3 GHz bandwidth, SP Devices, Sweden). A pulse generator (QC9512, Quantum Composer, Bozeman, MT) is used to synchronize the laser and MCP-PMT to ensure that the fluorescence decay can be collected within the PMT gating-window. A low-jitter (~100 ps) photodiode (DET10A, Thorlabs, Newton, NJ), which collects the laser scattering light reflected by the neutral density filter, is used to trigger the digitizer. The AOTF takes less than 20 μs to switch the selected wavelength. Therefore, by switching the frequency of the acoustic wave applied on the AOTF crystal, the fluorescence decay signals in the wavelength range of 370 nm to 550 nm are collected rapidly.

After collecting fluorescence decay signals, the AOTF-based spectrometer is set to a non-diffracted wavelength. Therefore, the fluorescence beam passes through the AOTF crystal without any diffracted beam. A mirror mounted on a mirror flipper is placed at 45 degree after the AOTF. When it is flipped to the vertical position, the fluorescence beam is reflected by this mirror into a grating-based spectrometer via a fused silica optical fibre (400 μm core, 0.22 NA) as shown in Figure 3-2(b). In this way, the steady-state fluorescence spectrum can be obtained. The pulse generator is used to control the mirror flipper to switch the data collection mode. The optical components of the TRF subsystem are shielded in a black aluminum box to avoid the effect of room light and to protect the MCP-PMT.

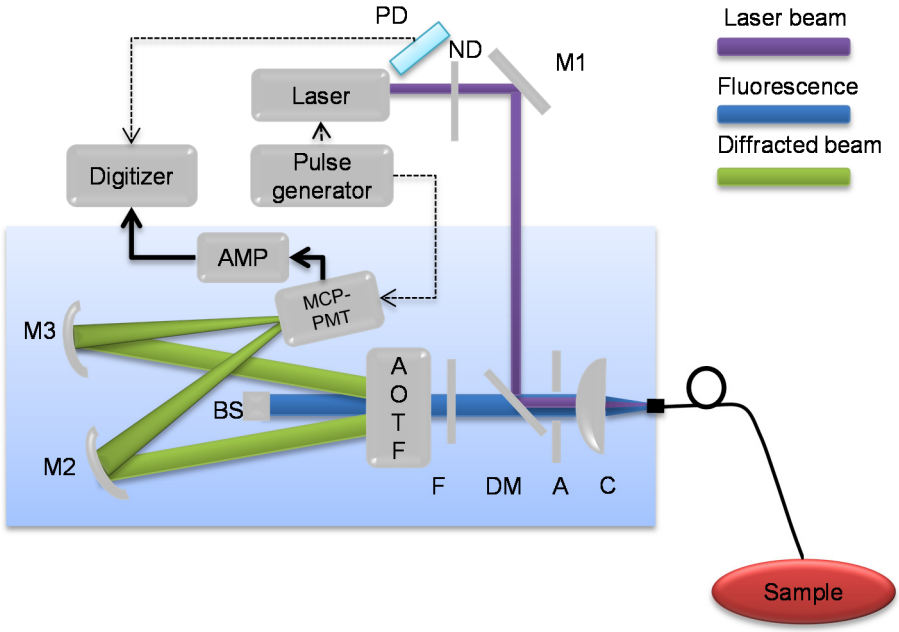

(a)

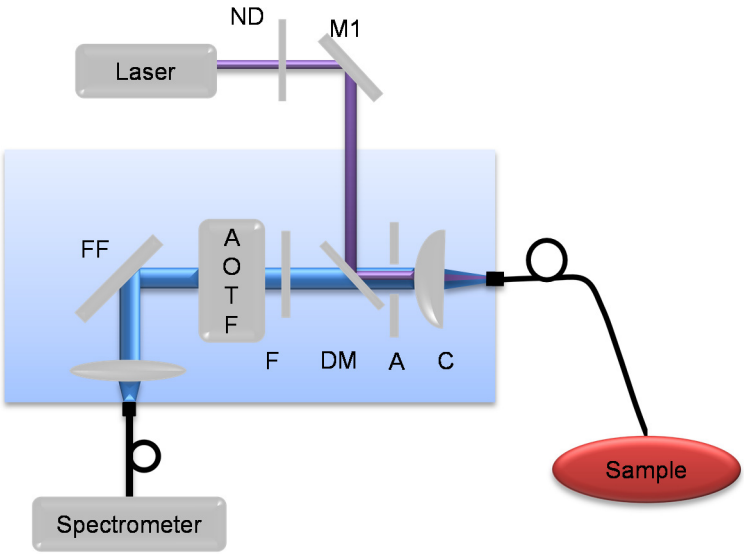

(b)

Figure 3-2. Schematic views of the TRF subsystem. (a) Dynamic fluorescence decay signal collection by the AOTF-based spectrometer. (b) Steady-state spectrum collection by the grating-based spectrometer. M1: flat mirror; M2, M3: concave mirrors; DM: dichroic mirror; C: plano-convex lens; F: long-pass filter; BS: beam stop; FF: mirror flipper; A: aperture; PD: photodiode; AOTF: acousto-optical-tunable-filter; MCP-PMT: multichannel-plate photomultiplier tube; AMP: preamplifier; ND: neutral density filter.

(a) Light source

The Nd:YAG laser at 355 nm with 1 mm^2 beam size is used in the TRF subsystem. The laser pulse energy is 30 μJ, which is too high for *in vivo* applications due to potential thermal damage of tissue and photobleaching of endogenous fluorophores. For example, the fluorescence spectra and lifetime of collagen and elastin changed when the excitation irradiance was above 20 $\mu W/mm^2$ [84]. Therefore, the laser energy is attenuated by the neutral density filter (OD=0.3) and the dichroic mirror (70 % reflectance ratio at 355 nm at 45 degree) before it is coupled into the optical fibre. The laser energy at the fibre tips can be adjusted from 0 to 5 μJ by changing the position of the reflectance mirror (M1) which is mounted on a kinematic holder (KM05T, Thorlabs, NJ). The laser energy measured at different positions along the propagation path of the laser beam is presented in Table 3-1.

Table 3-1. Laser energy at different transmission positions

Position	Laser energy (μJ/pulse)
Laser output	30
After neutral density filter	15
After dichroic mirror	10
After plano-convex lens	8
At the fibre tips	0-5

(b) AOTF-based spectrometer

The AOTF-based spectrometer was designed based on the elasto-optic effect of a birefringent crystal to realize wavelength selection. Briefly, this AOTF-based spectrometer is comprised of three parts: (i) the front light collimation part is used to collimate fluorescence light, block backscattered laser light, and eliminate background noise; (ii) the AOTF crystal component is used to select the diffracted beam at different wavelengths; and (iii) the detector is used to collect weak fluorescence signals in the time-domain by using a fast-gated MCP-PMT. In this section, detailed working principles of these three parts will be described.

A well-collimated incident beam is required for the AOTF to ensure its high diffraction efficiency. Therefore, in this setup, fluorescence light is collimated by the plano-convex lens as shown in Figure 3-3. The fluorescence beam size and divergence angle are calculated in Eq.(3.1) and Eq.(3.2) based on the parameters of the optical fibre and the plano-convex lens. The fluorescence beam has a diameter of 6 mm with a divergence angle of 15 mrad. The diameter increases with the increase of light propagation distance. The AOTF crystal needs to be placed at the position where the incident beam is well-collimated before it diverges greatly. Therefore, the beam size at

various distances away from the plano-convex lens were measured in order to choose a suitable position for the AOTF crystal (Figure 3-4). The beam size is stable at 6 mm in diameter when the transmission distance is 17 cm or less and is dispersed at longer distance. Hence, the AOTF was place at 10 cm after the plano-convex lens.

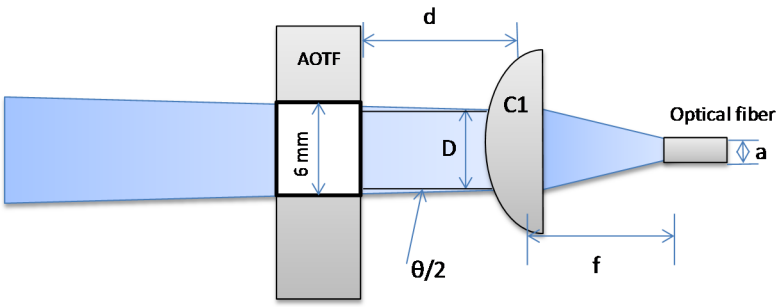

Figure 3-3. Schematic view of fluorescence light collimation using the plano-convex lens C1. D is the collimated beam size, θ is the full divergence angle, f is the focal length of C1, a is the fibre core size, and d is the transmission distance from the lens.

$$\text{Beam size (D):} \quad D = 2 \times f \times NA = 2 \times 25.4 \times 0.12 = 6.09mm \tag{3.1}$$

$$\text{Divergence angle (θ):} \quad \theta = \frac{a}{f} = \frac{400\mu m}{25.4mm} = 15mrad \approx 1° \tag{3.2}$$

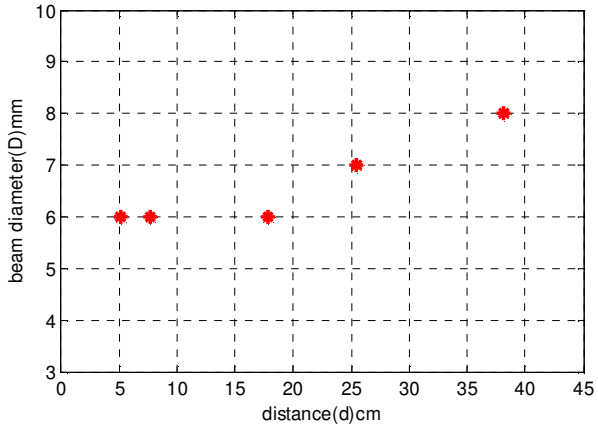

Figure 3-4. Fluorescence beam size was measured over a range of transmission distances. The beam stays collimated when transmitted less than 17 cm from the plano-convex lens.

Background light, which was introduced by the scattering of fluorescence light from the crystal surface and the bulk after the fluorescence, was found at the spatial position of the diffraction beam after the fluorescence beam transmitted through the AOTF crystal. In order to eliminate this background light, an aperture of 6 mm is used in the optical path

after the plano-convex lens. The detailed information of the aperture's function is described in Appendix II. The collimated fluorescence beam is transmitted through the dichroic mirror and the long-pass filter before it is directed incident on the AOTF window. The long-pass filter (OD=6 at 355 nm and transmission >93% in the 357.3-800.8 nm range) ensured high throughput of fluorescence signal, while blocking back-scattered laser light.

The AOTF is an electro-optical device, which works on the principle of Bragg diffraction in a birefringent crystal. When applying an acoustic wave across the crystal, a periodic modulation of the refractive index occurs in the crystal, which acts as a phase grating. A tellurium dioxide (TeO_2) crystal-based noncollinear AOTF is used in the TRF subsystem to obtain diffracted beams in the range of 370-550 nm. The operating principle of the TeO_2-based nonlinear AOTF is illustrated in Figure 3-5. A tunable radio frequency (RF) signal generated from an AOTF controller (VFI-145-90-SPF-B1-C2, Brimrose, Baltimore, MD) is applied to a piezoelectric transducer that is bonded on the crystal, thus introducing an acoustic wave through the crystal. This causes a periodic modulation of the refracted index through the crystal, which make it act as a grating. A random polarized beam (with the velocity of $\boldsymbol{K_i}$) is incident on the TeO_2 crystal with a certain angle θ from the optical axis. The incident light is divided to ordinary and extraordinary beam which have orthogonal polarization property in the birefringent crystal. Due to the differences of refracted indexes between ordinary polarized light (o-ray) and extraordinary polarized light (e-ray), the incident beam is separated into ordinary (o-ray, $\boldsymbol{K_{io}}$) and extraordinary (e-ray, $\boldsymbol{K_{ie}}$) components. The Bragg diffraction occurs when the o-ray and e-ray interact with the acoustic signal individually. The o-ray and e-ray components at the corresponding wavelength are diffracted from the broadband incident beam symmetrically with the orthogonal polarizations as the red arrows ($\boldsymbol{K_{do}}$ and $\boldsymbol{K_{de}}$) show. The rest of light transmits through the crystal at the zero order.

The wave-vectors of the nonlinear acousto-optic interaction for o-ray and e-ray are illustrated in Figure 3-6. This process diffracts two polarized components at a certain wavelength (λ_0) only when the wavelength satisfies the specific momentum-matching conditions [85, 86] for o-ray and e-ray as shown in Eq.(3.3) and Eq.(3.4) respectively:

$$\boldsymbol{K}_{do} = \boldsymbol{K}_{ie} + \boldsymbol{K}_{a}, \tag{3.3}$$

$$\boldsymbol{K_{de}} = \boldsymbol{K_{io}} - \boldsymbol{K_{a}}, \tag{3.4}$$

in which $\boldsymbol{K_{io}}$ and $\boldsymbol{K_{ie}}$, $\boldsymbol{K_{de}}$ and $\boldsymbol{K_{do}}$, and $\boldsymbol{K_a}$ are the wave vectors of the incident beam, diffracted beam, and acoustical wave, respectively. The magnitudes of these wave vectors are $|\boldsymbol{K}_o| = \frac{2\pi n_i}{\lambda_0}, |\boldsymbol{K}_d| = \frac{2\pi n_d}{\lambda_0}, |\boldsymbol{K}_a| = \frac{2\pi f}{V}$, in which λ_0 is the diffracted wavelength in

vacuum, f is the acoustic frequency and V is the acoustic wave velocity, n_i and n_d are the refractive indices for the incident and diffracted beams respectively. For the extraordinary incident component, $n_i=n_e$ and $n_d=n_o$, and for the ordinary incident component, $n_i=n_o$ and $n_d=n_e$. Therefore, the diffracted beam emits from the crystal surface with a small deflection angle away from normal path of the undiffracted beam. Wavelength selection is achieved in the order of a few microseconds by changing the modulating acoustic wave frequency.

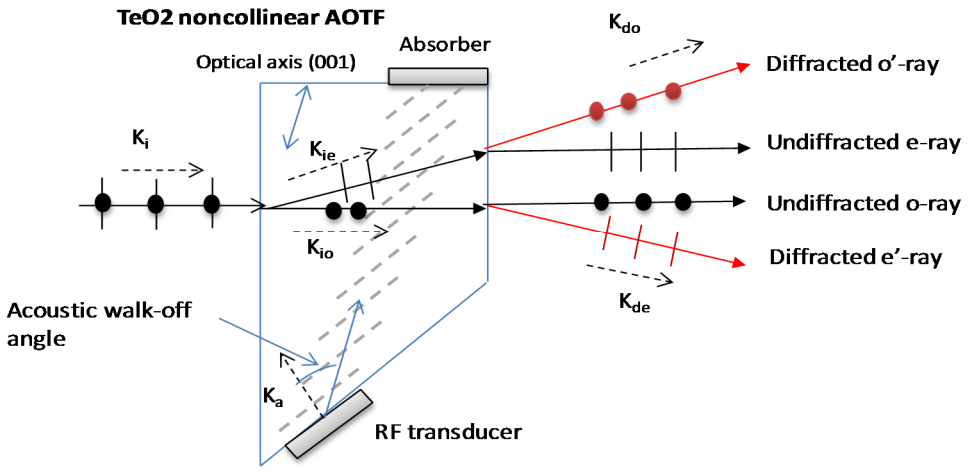

Figure 3-5. The operating principle of the TeO_2 noncollinear AOTF. K_i: the vector of incident beam, K_{ie}: the vector of extraordinary component of incident beam, K_{io}: the vector of ordinary component of incident beam, K_{de}: the vector of the diffracted e-ray, K_{do}: the vector of diffracted o-ray, and K_a: the vector of acoustic wave.

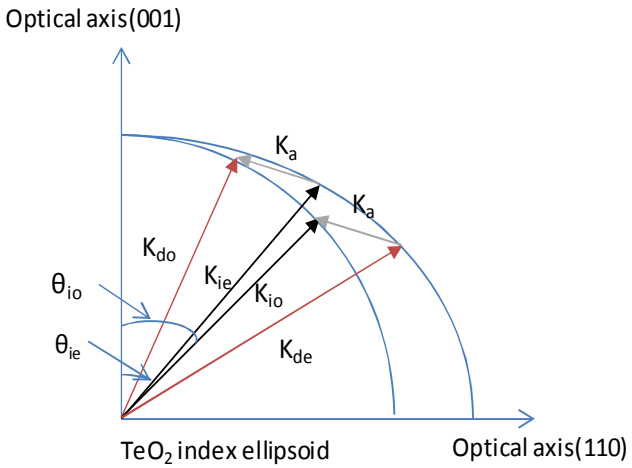

Figure 3-6. Wave-vector diagram of the acousto-optics interaction. K_a: the vector for acoustic wave. K_{do} and K_{de} : the vectors for diffracted o-ray and e-ray, and θ_i : the incident angle.

The incident angular aperture of TeO_2 AOTF is around 4-5 degrees. The deflection angle of the diffracted beam is ~6.4 degrees. The AOTF configuration was designed only for a single polarized beam incident on the AOTF crystal window perpendicularly. In our case, both diffracted beams are used to achieve sufficient throughput. However, based on Eq.(3.3), the diffracted wavelengths are slightly different for the o-ray and e-ray under the same acoustic frequency. By rotating the AOTF by 2 degrees, it is possible to minimize the wavelength differences between the diffracted o-ray and e-ray. Spectral calibration of the AOTF for combining the two diffracted beams are necessary to guarantee that both diffracted beams have the same spectral characteristics. These calibration results will be presented in Section 3.2.

Once the diffracted beams are emitted from the AOTF, they are focused onto the gated MCP-PMT by two concave mirrors. The optical paths of the o-ray and e-ray diffracted beam were designed identically to avoid temporal broaden of the decay signal. The gated MCP-PMT consists of a photocathode, an MCP, and an anode. Once the light is incident on the photocathode, the photoelectrons emitted from the photocathode enter the MCP. MCP is a thin disk that consists of a large number of glass capillaries with 6 μm diameter bundled in parallel [88]. The second emission occurs when the photoelectrons hit on the wall of the MCP capillaries in which each channel acts as an independent electron multiplier. Hence, a large number of electrons are emitted out from the MCP. Due to the narrow channel diameters of the MCP, the electrons actually travel with nearly the same path length, thus the transit time spread (TTS) of MCP-PMT is much smaller than that of the dynode-based PMT [88]. The gated MCP-PMT used in the TRF subsystem has a short TTS of ~90 ps. It allows us to collect a short pulse in a few hundreds of picoseconds. The gating time can be set in the range of 5 ns-10 μs to improve the data collection efficiency of MCP-PMT. Due to the large timing jitter of the laser beam, the gating time of MCP-PMT is set at 6 μs to ensure that all fluorescence decay signals can be collected [89]. The preamplifier with a power gain of 63 dBm and bandwidth of 50 kHz-1.5 GHz is used to amplify the output signal from the MCP-PMT as well as eliminate the low frequency noise such as the ambient background with 50 Hz frequency. This feature ensures the feasibility of this system in the operating room (OR) where the ambient light is on during surgery. The AOTF-based spectrometer is housed in a black aluminum box to protect the PMT under the room light operation condition and shield the system from electromagnetic distortion.

The analog signal from the preamplifier is acquired by the high-speed digitizer with the sampling rate of 3.6 GS/s and the bandwidth of 1.3 GHz. The digitizer is triggered by a photodiode before the fluorescence signal arrives. The amplitude range of the digitizer

is from +50 mV to -750 mV. The acquired fluorescence signals are saved in the large buffer on the digitizer board during the acquisition and then transfer to computer, which ensured the real-time data acquisition. To check the capability of the digitizer in acquiring fluorescence decay accurately, the digitizer with various sampling rates and amplitude resolutions were compared. The results will be described in Section 3.2.

(c) Time synchronization of fluorescence decay acquisition

The fluorescence decay signals are collected at 37 wavelengths in the spectral range of 370-550 nm with 5 nm intervals. Ten pulses are averaged at each wavelength. The timing synchronization of the measurement of fluorescence decay is shown in Figure 3-7. The AOTF controller is used as a master control. When the RF frequency on the AOTF is switched, a 32 µs synchronization signal is generated simultaneously to trigger the pulse generator. The pulses that are generated from pulse generator Channel A and Channel B are used to trigger the laser and open the gate of MCP-PMT, respectively. A pulse with pulse-width of 50 µs was used as the laser trigger signal, whereas a pulse with pulse-width of 6 µs and delay of 115 µs relative to trigger signal of laser is set as the MCP-PMT gated signal [89]. The photodiode, which captured the scattered laser light from the neutral density filter, is used to trigger the digitizer. The fluorescence decay signal arrives at the digitizer about 40 ns later than the trigger signal due to the transmitted time of laser and fluorescence light through the four-meter length fibre optic probe. Once the digitizer acquires the fluorescence decay signal, only a fluorescence signal segment (~50 ns) is saved into the buffer of the digitizer.

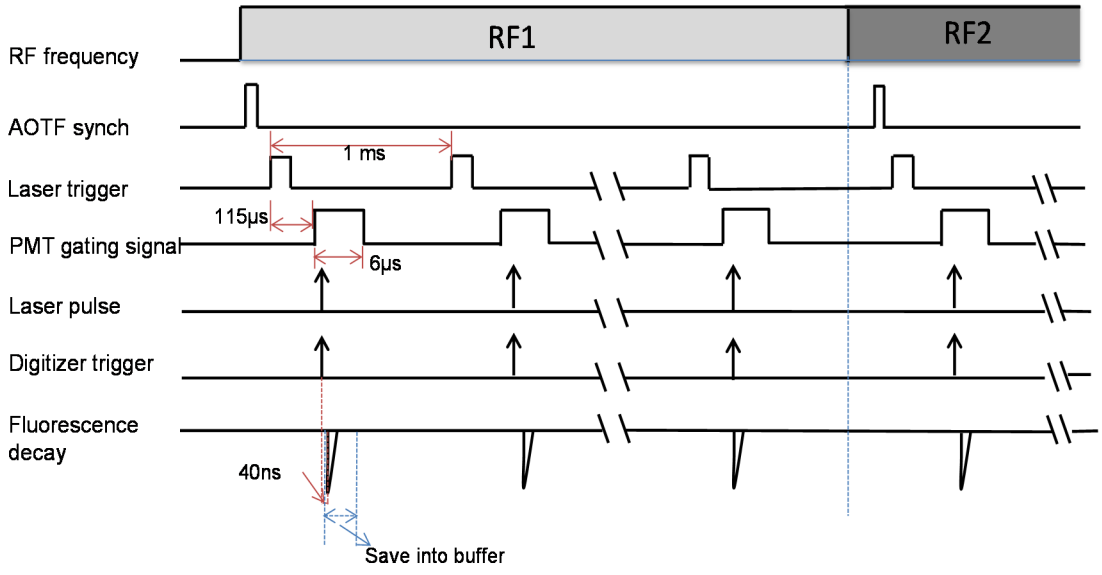

Figure 3-7. Timing synchronization of the fluorescence decay acquisition in the TRF subsystem.

3.1.2. DR spectroscopy subsystem

A spatially resolved DR spectroscopy subsystem (Figure 3-8) was built to investigate the optical properties of biological tissue in the UV-VIS wavelength region. Three high-power UV LEDs (370 nm, 385 nm, and 400 nm, Lumibright, Innovation Optics, Woburn, MA) and a 150 W tungsten-halogen lamp (MI-150, Edmund Optics, Barrington, NJ) was combined as the DR light source to measure the optical properties in the UV-VIS range. Three LEDs are mounted on a PCB board and collimated by a light coupler to guarantee the homogenous wavelength distribution. The LED power can be adjusted by a homemade PWM power controller. The output beam of LEDs and halogen lamp are combined into a beam by a dichroic mirror with the cutoff wavelength of 425 nm (DLMP425, Thorlabs, NJ). The spectrum of the broadband light source is shown in Figure 3-9. The combined light beam is split by a 20/80 beam splitter (FOS-400-0102-80/20-123, Fibersense and Signals, San Jose, CA). 20% of the light is used as a reference light; the rest light illuminates the sample via a 200 μm core fibre probe. In addition, a shutter is mounted before the optical fibre coupler to control the light illumination. Four independent spectrometers (BLUEwave, StellarNet, Tampa, FL) are used to collect the diffuse reflectance spectra at three source-detector distances as well as the reference channel. This configuration is able to set the integration time for each channel individually to obtain sufficient signals without optical attenuators, making the system much easier to control during the clinical studies.

The background noise is also measured and subtracted from measured DR spectra. These spectra are then normalized by the reference light to obtain intensity variation over the measured spectral range. The diffuse reflectance spectrum R can be calculated as:

$$R = (R_m - R_{bkg})/R_{ref} \tag{3.5}$$

where R_{ref} is the reference spectra, R_{bkg} is the background noise, and R_m is the measured diffuse reflectance spectra.

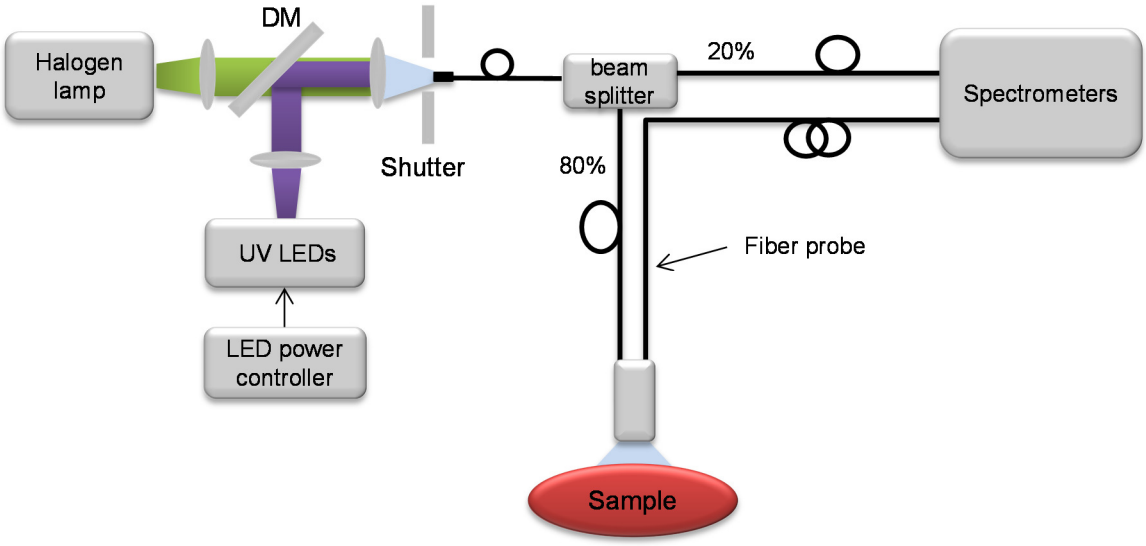

Figure 3-8. Schematic view of the DR spectroscopy subsystem. The light source includes a halogen lamp and three UV LEDs (370 nm, 385 nm, and 405 nm). Four spectrometers are used to collect the reference light and diffuse reflectance spectra at different source-to-detector distances. DM: dichroic mirror.

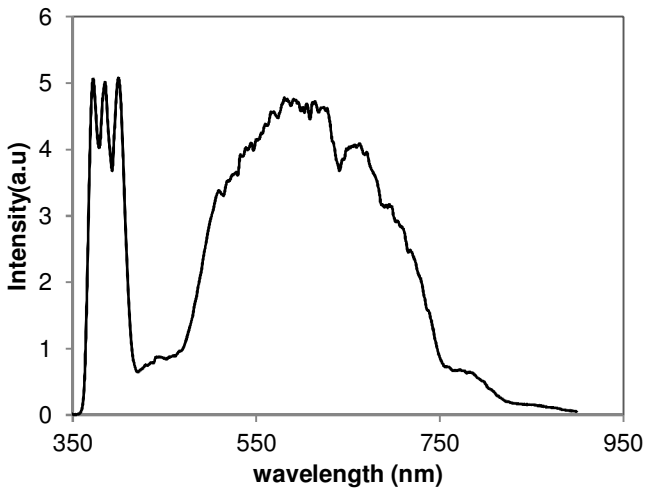

Figure 3-9. The spectrum of the combined UV-VIS light source.

3.1.3. Dual-modality fibre optic probe

A dual-modality fibre optic probe was designed to collect fluorescence and diffuse reflectance signals in a small tissue volume. A schematic view of the probe tips is shown in Figure 3-10a. An optical fibre with a core diameter of 400 µm and NA of 0.12 is placed at the centre of probe. It is used for the laser excitation and fluorescence collection of the TRF subsystem. An optical fibre with a core diameter of 200 µm and NA of 0.22 placed

at the side of probe tips (as the red dot shows) is used as the light source for the DR subsystem. The other three fibre bundles are used to collect the DR signals from three source-detector distances of 0.23 mm, 0.59 mm, and 1.67 mm. The arrangement of fibres was designed using the Monte Carlo simulation to accurately recover the optical properties from tissue [65]. As shown in Figure 3-10b, the diameter of the fibre probe is 2 mm. A neurosurgeon can hold this probe by hand to measure TRF and DR signals during surgery. The fibre probe is in direct contact with the sample surface in clinical studies.

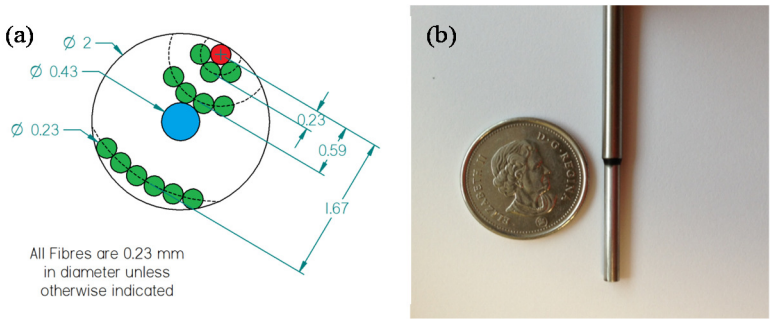

Figure 3-10. Dual-modality fibre optic probe. (a) The schematic view of fibre optic probe tip. DR source fibre was placed as red circle shows for a broadband illumination at 355-800 nm. DR detector fibres were arranged in three bundles at the different source–detector distances as green circles show, while blue indicates the TRF fibre (contributed by Derek Cappon [65]). (b) The photograph of the probe that can be held by the surgeon to collect signals in surgery.

3.1.4. Integrated system control program

A system control program generated in VC++ is used to conduct the data acquisition, and display measured results during clinical studies. The flow chart of data acquisition is shown in Figure 3-11. The system components, including digitizer, AOTF controller, LED controller, pulse generator, are initialized at first. TRF-DR system collects the fluorescence decay signals, fluorescence steady-state spectra, and diffuse reflectance spectra in sequence after system initialization. The pulse generator is used to switch the data collection mode. After measurement, the TRF and DR data are saved in different files for the off-line analysis. The controller programming software interface (GUI) is shown in Figure 3-12. The initial results of fluorescence spectra and diffuse reflectance spectra are shown in the GUI right after the data collection. The data acquisition time is ~500 ms to collect 407 fluorescence decay pulses, whereas the data acquisition times of the steady-state fluorescence and diffuse reflectance signals depend on the integrated times of spectrometers. The total data acquisition time is within 2 seconds, which ensured the compatibility of the TRF-DR system with intraoperative measurements.

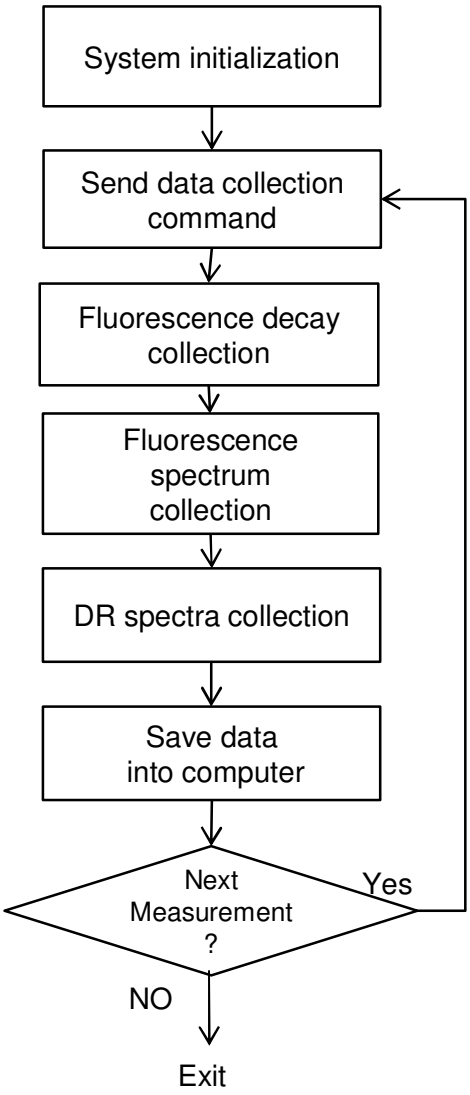

Figure 3-11. The flow chart of data collection by the TRF-DR spectroscopy system. The system is first initialized to set the data acquisition parameters. The fluorescence decay and spectrum, as well as DR spectra are acquired in sequence. The total data acquisition time is within 2 s.

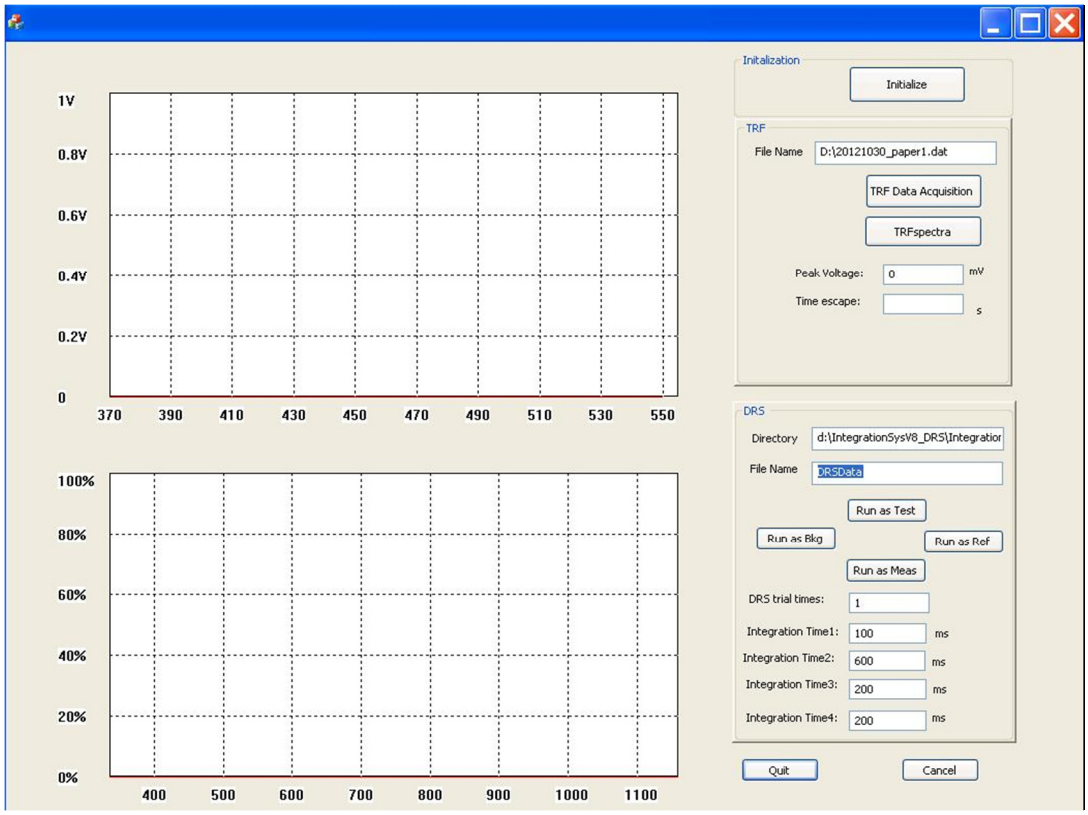

Figure 3-12. Software GUI of the integrated TRF-DR spectroscopy system. The TRF and DR signals are collected in sequence and displayed immediately after measurement.

After data acquisition, raw data were processed in an off-line program. The detailed data analysis, including numerical Laguerre deconvolution to remove the system response and calculation of the average lifetime values, are conducted after the experiment in graphical user interface software programmed in MATLAB (MathWorks Inc, Natick, MA). The fluorescence intrinsic response function (IRF) can be extracted from measured signals by using the Laguerre-based deconvolution method, which will be discussed in Chapter 5. This method can calculate the fluorescence lifetime accurately and quickly without an assumption of the fluorescence decay curve [92]. The intensities at different wavelengths are obtained by integrating the signals over the decay time. In addition, the steady-state spectrum can also be measured from the conventional grating-based spectrometer. Optical properties were recovered from spatially resolved DR spectra by using the inverse Monte Carlo approach described in Ref [65]. This hybrid look-up table/Mono Monte Carlo algorithm accounts for boundary effects resulting from the change in refractive index at the edge of the probe [65].

3.1.5. Clinical layout and safety

The TRF-DR spectroscopy system is housed in a mobile cart as shown in Figure3-1b. The DR subsystem is mounted at the first shelf, the electronic components of TRF subsystem are placed at the middle shelf, and the AOTF-based spectrometer is mounted on the bottom shelf. An uninterruptible power supply [(UPS) APC Back-UPS XS 1500VA, American Power Conversion, West Kingston, RI] is used to provide instant protection in the event of momentary power interruptions to prevent the loss of data. In addition, six fans are used to maintain the temperature in the cart.

The TRF-DR spectroscopy system strictly adheres to the safety guidelines. A medical isolation transformer (ISB-120C, Toroid Co., Salisbury, MD) is used to isolate the patient and surgeon from a potential electric shock and protect our system from electronic power change. The fibre optic probe needs to be kept sterilized before the surgery and during the measurement. The laser energy and light source power are used under the safety level to avoid the thermal damage of biological tissue [93, 94]. The laser energy is measured by a power meter before clinical studies and adjusted to <3μJ to avoid the photobleaching of endogenous fluorophores and potential thermal damage of biological tissue.

3.2. System calibration

3.2.1. TRF susbsystem calibration

The calibration of the TRF subsystem mainly includes: 1) the spectral response of AOTF-based spectrometer, 2) the intensity response, 3) the temporal response, 4) the effects of digitizer performance on the lifetime accuracy, and 5) the signal-to-noise ratio as a function of averaged pulse.

(a) Spectral response of AOTF-based spectrometer

The basic principle of AOTF has been described in Section 3.1.2. Both o-ray and e-ray diffracted beams are collected to improve the throughput. Due to the differences of refractive index between the o-ray (n_o) and e-ray (n_e) in the TeO_2 birefringent crystal, both peak wavelengths of two diffracted beams are not completely identical. Moreover, the calibration results provided by the AOTF manufacturer were optimized only for the extraordinary polarized incident light, which may not be applicable for the double beam configuration. Thus, it is necessary to characterize the spectral responses for both diffracted beams and minimize their differences.

The spectral responses of both diffracted beams across the spectral region of interest were calibrated using a tungsten-halogen lamp (HL-2000, Ocean Optics, Clear water, FL), which was shining onto the distal end of the fibre probe. The diffracted beams in the spectral range of 370-550 nm with 5 nm intervals were measured by a spectrometer

(OEM-400, Newport, Irvine, CA) with 0.3 nm spectral resolution. The relationship between the RF signal and diffracted wavelength was characterized for both diffracted beams as shown in Figure 3-13. The diffracted wavelength was inversely proportional to the RF signal. By carefully adjusting the AOTF position and angle, the differences of peak wavelength between two diffracted beams was minimized within 1 nm as shown in Figure 3-14. The peak wavelength of the o-ray diffracted beam was slightly larger than that of the e-ray due to the $n_e > n_o$ in the TeO_2 crystal. Moreover, the diffraction efficiency of AOTF is depends on the RF power and varies with wavelength. The diffraction efficiency increases with the increase of the RF power, but it could saturate when the RF power exceeds the saturation power level as shown in Figure 3-15. The saturation causes two diffraction peaks and broadens the bandwidth of diffracted beam. Since the saturation power changes at different wavelengths, the RF power needs to be set individually at each wavelength. Therefore, the RF frequencies and maximum powers were measured and saved into a look-up table that can be recalled for wavelength selection during the data acquisition. The detailed look-up table of the RF frequency and power for each wavelength can be found in Appendix II.

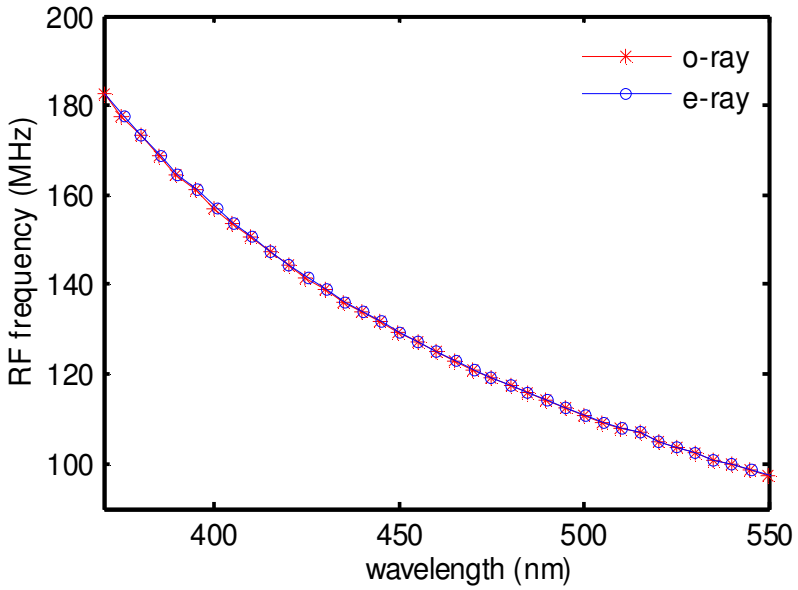

Figure 3-13. The relationship between the RF frequency and the diffracted wavelength of o-ray and e-ray diffracted beams. The diffracted beam of AOTF was calibrated from 370 nm to 550 nm corresponding to the RF frequency range of 90-190 MHz. The RF frequency decreased with the increase of diffracted wavelength.

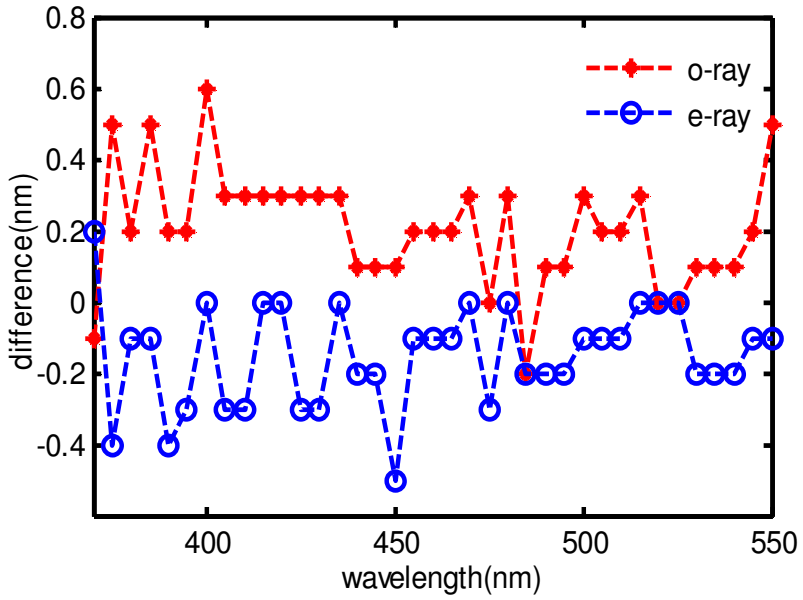

Figure 3-14. Differences between ordinary (o-ray) and extraordinary (e-ray) diffracted beams in the observed spectral region. The differences are smaller than 1 nm. The peak wavelength of o-ray is slightly larger than that of e-ray due to $n_e > n_o$ of the TeO_2 crystal.

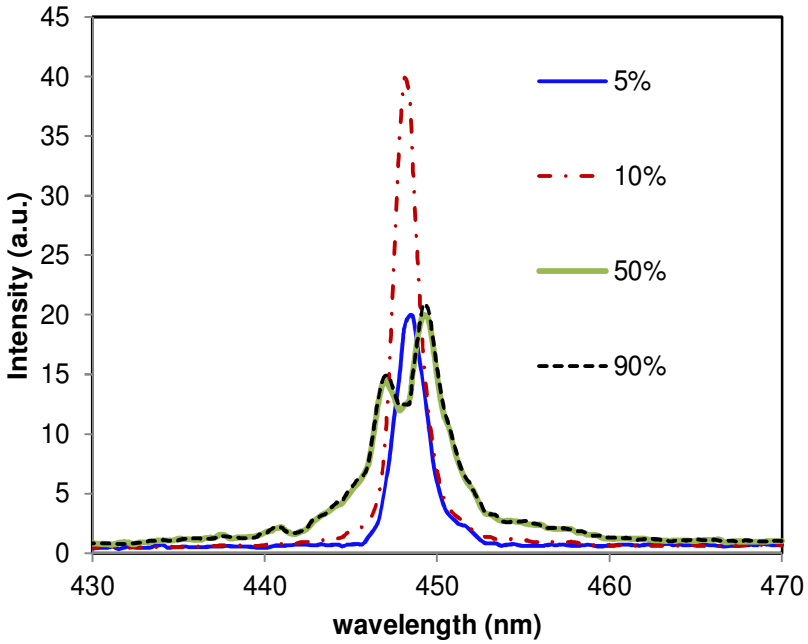

Figure 3-15. The diffracted beams at 448 nm with different RF power amplitudes. The saturation occurs when RF amplitude increases.

The spectral resolution of the AOTF-based spectrometer is dependent on the diffracted beam bandwidth that is related to its central wavelength. The bandwidth shape of a noncollinear AOTF is ideally a Sinc-squared function and the bandwidth (FWHM) can be approximated by

$$\Delta\lambda = \frac{0.9\lambda^2}{\Delta n L \sin\theta_i} \tag{3.6}$$

where λ is the central wavelength of the diffracted beam, L is the acousto-optic interaction length, $\Delta n = n_e - n_o$ is the difference of refractive index between e-ray and o-ray, and θ_i is the light incident angle [86]. The bandwidths of the diffracted beams were measured from 390 nm to 550 nm with 20 nm intervals. It is within the range of 1-2.5 nm and increases at longer wavelengths (Figure 3-16), which is in good agreement with the prediction of Eq.(3.6).

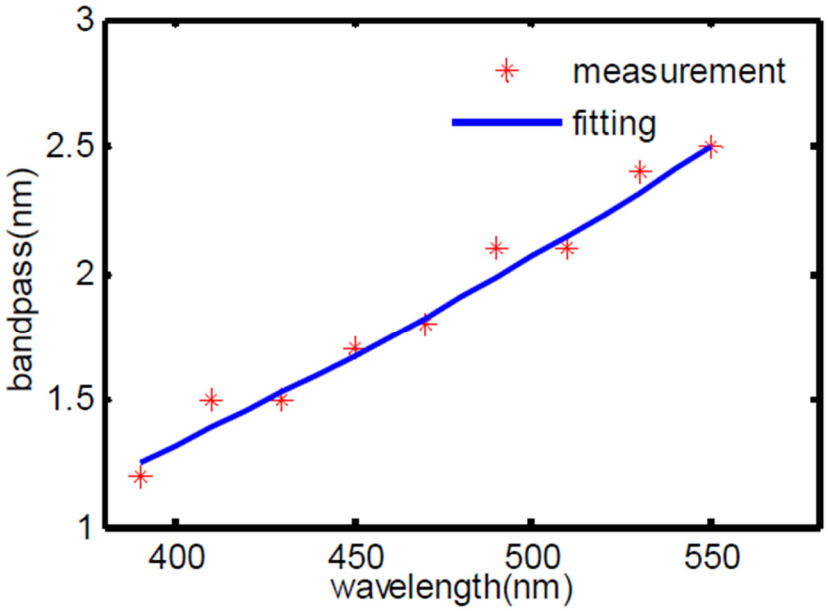

Figure 3-16. The bandwidths of the diffracted beams at different wavelengths. The bandwidth was measured from 390 nm to 550 nm at 20 nm intervals (red stars). The bandwidth increases with increasing the central wavelength, which is good agreement with the calculation results (blue curve).

In order to assess the performance of the AOTF-based spectrometer, the fluorescence signals from fluorescein solution were measured. Both the diffracted beams and combined beam were measured at its emission peak of 515 nm as Figure 3-17 shows. The o-ray and e-ray diffracted beams had differences in spectral intensity and peak

wavelengths (about 0.3 nm). The total fluorescence intensity increased by combining two beams together and the bandwidth of combination beam increased to 2.5 nm. The optical path lengths of both diffracted beams were designed to be identical, such that there is no broaden introduced by combining those decays together as shown in the inset figure of Figure 3-17.

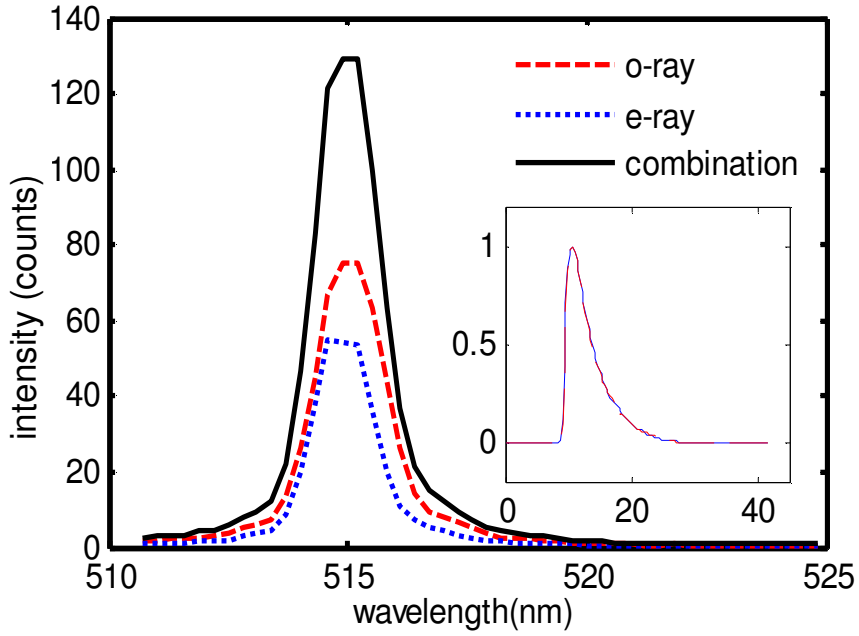

Figure 3-17. AOTF diffracted beam characterization using the fluorescein solution. The peaks for both diffracted beams have slight differences. The ordinary diffracted beam (red curve) has a peak at 515 nm, while extraordinary diffracted beam (blue curve) has peak at 514.4 nm. Combining these two diffracted beam (black curve) can increase the fluorescence intensity and bandwidth. Inset figure is the fluorescence decays of two diffracted beams (x-axis unit: ns, y-axis unit: normalized amplitude).

(b) Intensity response of AOTF-based spectrometer

The intensity response of the TRF subsystem is contributed by the AOTF, the MCP-PMT, and other optical components such as optical fibre. The intensity response calibration was carried out according to the calibration procedure described in Ref [16]. A calibrated halogen lamp (HL-2000-CAL, Ocean Optics) was used as a broadband light source standard. The spectrum of this lamp was measured by a well calibrated spectrometer with 5 nm spectral resolution as a reference. The intensity of this lamp at each selected wavelength was then measured by the TRF subsystem. The correction coefficient can be calculated as

$$S(\lambda) = M_{lamp}(\lambda) / T_{lamp}(\lambda) \quad (3.7)$$

where $T_{lamp}(\lambda)$ is the spectral intensity measured by the calibrated spectrometer, $M_{lamp}(\lambda)$ is the spectral intensity measured by the TRF subsystem, and $S(\lambda)$ is spectral intensity correction coefficient as shown in Figure 3-18. The TRF subsystem has higher intensity response between 430 nm and 460 nm. Therefore, after the fluorescence spectrum is collected by the TRF subsystem, the background and non-uniformity of the instrument intensity response can be corrected using Eq.(3.7). Thus, the corrected spectrum $C(\lambda)$ can be calculated by

$$C(\lambda) = \frac{M(\lambda) - \mathrm{B}(\lambda)}{\mathrm{S}(\lambda)} \quad (3.8)$$

where $M(\lambda)$ is the measured fluorescence emission and $B(\lambda)$is the background signal.

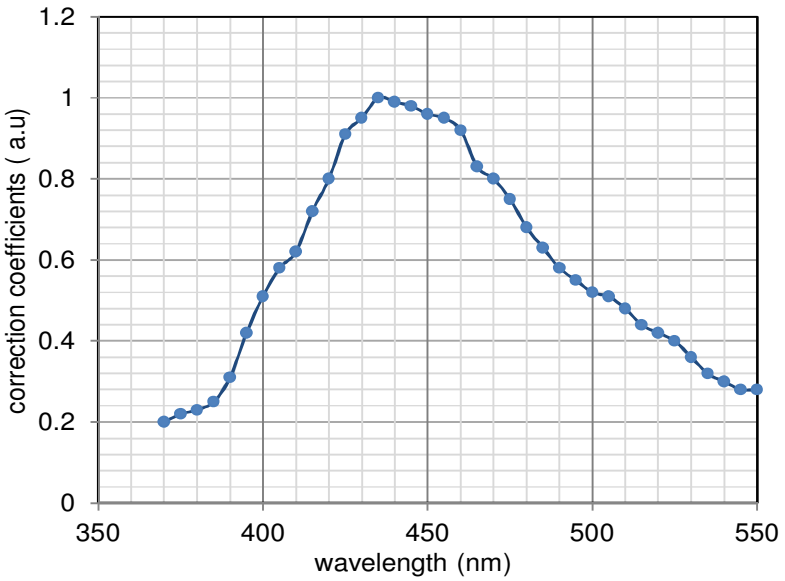

Figure 3-18. The spectral correction coefficients of the AOTF-based spectrometer. The system has the highest intensity response at 435 nm.

(c) Temporal response of the TRF subsystem

The fluorescence lifetime values of endogenous fluorophores in biological tissue are in the range of a few hundred picoseconds to tens of nanoseconds. Therefore, a temporal resolution of less than a few hundred picoseconds is required for the TRF subsystem to measure fluorescence decays accurately. The temporal resolution of the TRF subsystem is determined by the temporal response of the MCP-PMT, the preamplifier, the digitizer and

the optical components especially the optical fibre. The temporal response function of each element can be assumed as a Gaussian distribution. The system temporal resolution can be calculated by adding the squares of temporal response of each element [91]:

$$\Delta t^2 = \Delta t_{digitizer}^2 + \Delta t_{trigger}^2 + \Delta t_{PMT}^2 + \Delta t_{amplifier}^2 + \Delta t_{optical}^2 \quad (3.9)$$

where the rise times are 270 ps for the digitizer, 100 ps for the photodiode trigger, 180 ps for the MCP-PMT, and 233 ps for the preamplifier. The temporal dispersion of the optical components was mainly contributed by the optical fibre probe. Both the chromatic dispersion and the model dispersion in the fibre optic probe broaden the fluorescence decays in the time-domain. The fluorescence decays at different wavelengths arrive at the detector at different time due to the chromatic dispersion. The time-delay introduced by the chromatic dispersion is less than 10 ps for a diffracted beam with 2.5 nm bandwidth (FWHM). The model dispersion broadens the fluorescence beam due to the different transmission paths in the fibre. The time-delay introduced by model dispersion is around 66 ps for the fluorescence light in the visible spectral range when it transmit through a 4 mater length fibre 0.12 NA.

The temporal response induced by the different elements was determined by measuring their influence on the bandwidth (FWHM) of a narrow laser pulse which can be approximated as a delta function). Practically, considering the influence of the illuminated laser pulse and system temporal response to the fluorescence measurement, a 355 nm laser pulse with the bandwidth of 0.3 ns FWHM was measured by the TRF subsystem. A diffused standard (SRS-10, Labsphere, NH) was used to reflect the laser illumination light back into the optical fibre. The long-pass filter was removed in this measurement. The diffracted wavelength of the AOTF was set at 370 nm which can captured a portion of the laser light without damaging the MCP-PMT. The temporal response of the 355 nm laser is 0.8 ns as shown in Figure 3-19a. This measured result was used in the deconvolution analysis to eliminate the effects of system and laser from measured fluorescence decay signal (Figure 3-19b). The detailed deconvolution method used to retrieve the intrinsic response function will be described in Chapter 5.

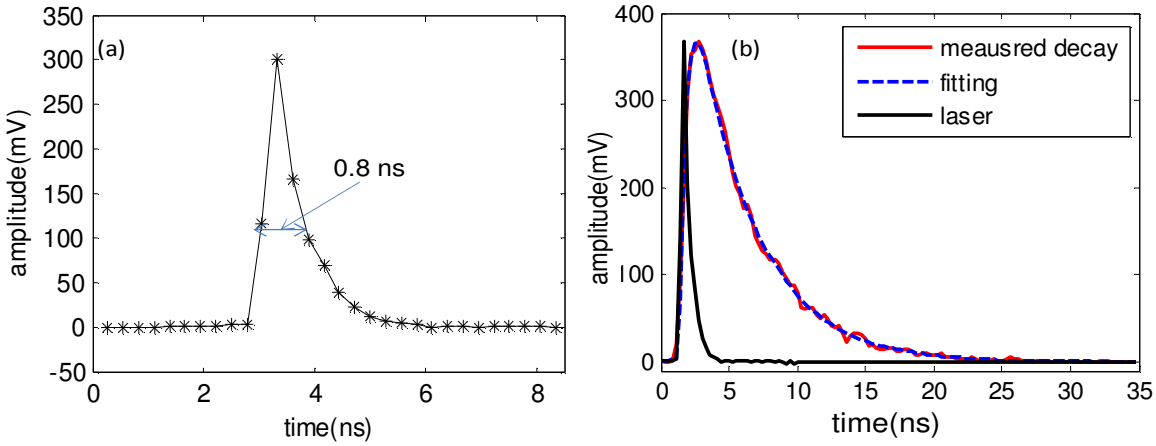

Figure 3-19. Temporal resolution measurement of TRF subsystem. (a) The laser beam at 355 nm with pulse width of 300 ps was measured by the TRF subsystem to get a response pulse of 0.8 ns in FWHM. (b) Deconvolution of the measured fluorescence decay with the laser response signal.

(d) Effect of digitizer properties on fluorescence lifetime accuracy

The parameters of the digitizer, including the sampling rate, the bandwidth and the amplitude resolution, influence the accuracy of the fluorescence acquisition. Amplitude resolution introduces the quantization noise resulting from the quantization process. On the other hand, sampling rate and bandwidth of the digitizer determine its temporal resolution in retrieving the analogue signal. To investigate how these parameters affect the fluorescence signal acquisition, the simulation and experiment of the fluorescence signal sampling using different digitizers were carried out.

Fluorescence decay acquisitions were simulated to assess the digitizer performance. Hundreds of decays were generated for each lifetime value (2 ns, 5 ns, and 10 ns). The signal amplitudes of the fluorescence decays were set as 80% of full amplitude scale of the digitizer. The digitizer with both 8 bit and 12 bit amplitude resolution were simulated under the different sampling rates of 1, 2, 3, and 6 GS/s. The quantization noise was uniformly distributed between ± ½ least significant bit (LSB) with a mean of zero and a standard deviation of $1/\sqrt{2^{N-1}}$ LSB (~0.29 LSB). Therefore, the quantization error of the 12 bit digitizer is extreme smaller than that of 8 bit digitizer. The bandwidth was set as half of sampling rate to meet the Nyquist–Shannon sampling theorem to avoid aliasing. Random noise and jitter were set according to the TRF subsystem measurement results in which the jitter was about 0.1 ns and the noise level was 1%. The detailed parameters used in the simulation are presented in Table 3-2.

The effects of the amplitude resolution and temporal resolution on the fluorescence acquisition are shown in Figure 3-20. The errors of fluorescence lifetime decreased with

increasing the sampling rate of digitizer. The lifetime errors in 12 bit amplitude resolution were 50 times smaller than that of 8 bit when the quantization error is only considered (Figure 3-20a and 3-20b). However, this feature was not observed when the noise and jitter were considered into the simulation as shown in Figure 3-20c and 3-20d. The lifetime errors were mainly contributed by the sampling rate of the digitizer. In addition, the lifetime error increased quickly when using a low sampling rate especially for the fast decay signal. The results suggest that the digitizer performance is highly dependent on the sampling rate rather than the amplitude resolution especially for fast fluorescence decay signals. Hence, the digitizer with 12 bit, 3 GS/s can provide an accuracy acquisition.

Table 3-2. Parameters for digitizer simulation

Amplitude resolution	8 bit	12 bit
Quantization noise	1/(2^8) LSB	1/(2^{12}) LSB
Random noise	1%(2.57 LSB)	1% (40 LSB)
Jitter	0.1ns	0.1ns
Sampling rate	1, 2, 3 and 6 GS/s	1, 2, 3 and 6 GS/s

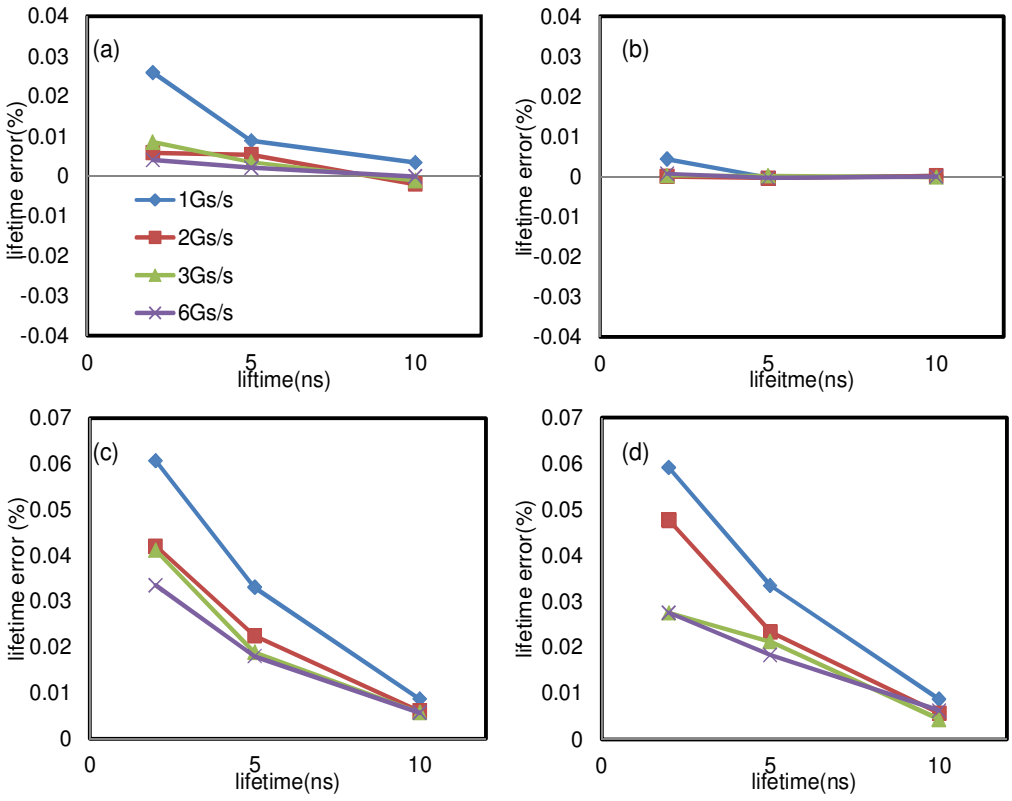

Figure 3-20. Simulation results of fluorescence lifetime using the digitizer with different amplitude

resolution and temporal resolution. (a) and (b) are the simulation results without jitter and noise for 8 bit and 12 bit amplitude resolution, respectively. (c) and (d) are the simulation results with jitter and noise.

The comparison of the ADQ 412 high-speed digitizer (3.6 GS/s sampling rate and 1.3 GHz bandwidth) and the DPO 7254 (40 GS/s sampling rate and 2.5 GHz bandwidth) oscilloscope was investigated and the results are shown in Table 3-3 [43]. The ADQ 412 high-speed digitizer could achieve the same performance as the DPO 7254 oscilloscope when estimating the fluorescence lifetime values in the range of sub nanoseconds to several nanoseconds. However, the standard error of fluorescence lifetime estimated by the ADQ 412 digitizer is twice as large as that of the DPO 7254 oscilloscope. The simulation and experimental results demonstrated that the fluorescence decay signal can be accurately retrieved using the ADQ 412 high-speed digitizer.

Table 3-3. The lifetime values of standard fluorescence dyes estimated by ADQ 412 digitizer and DPO 7254 oscilloscope

Fluorescence sample	ADQ 412 12 bit, 3.6 GHz (ns)	Tektronix 8 bit, 40 GHz (ns)	Reference lifetime (ns)
9-CA (ethanol)	11.8 ± 0.06	12.1 ± 0.04	11.85
Lucifer yellow (NaOH)	4.9 ± 0.06	5.1 ± 0.03	4.9~5.1
Fluorescein (ethanol)	4.0 ± 0.06	4.0 ± 0.01	4.1
Paper	0.9 ± 0.02	0.9 ± 0.01	N/A

(e) Signal-to-noise ratio as a function of averaged decay pulse numbers

The autofluorescence signal of biological samples is very weak. Therefore, averaging a number of decay pulses at each wavelength can improve the SNR to decrease the uncertainties in the fluorescence lifetime values. In order to investigate the relationship between the averaged pulse numbers (N) and SNR, the fluorescence decays of the fluorescein solution were measured at 515 nm with averaged pulse numbers ranged from 5 to 2000. The SNR is defined as the ratio of the peak intensity and its standard deviation. Each measurement was repeated ten times. In Figure 3-21a, the SNR increases with the increase of averaged pulse numbers following to $\sqrt{N}$ dependence as predicted by the Poisson distribution [97]. Similarly, in Figure 3-21b, the standard deviation of the lifetime values decreases with the increase of the averaged pulse numbers. The relative standard deviation of the calculated lifetime is <5% when averaging 10 or more pulses together, which ensures to retrieve the lifetime correctly. However, averaging more pulses will increase the data acquisition time. Therefore, ten fluorescence decay pulses are averaged at each wavelength during the TRF spectroscopy measurement to keep balance between the SNR and data acquisition time.

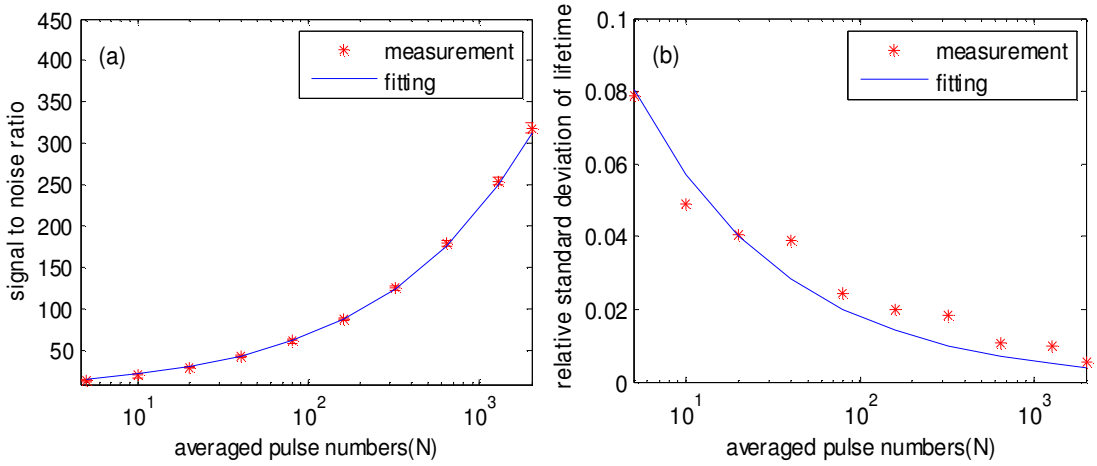

Figure 3-21. Signal-to-noise characterization of the TRF subsystem performed on the fluorescein decay in different averaged pulse numbers (N = 5, 10, 20, 40, 80, 160, 320, 640, 1280 and 2000). (a) The signal-to-noise ratio increases with the increase of averaged pulse numbers, which is proportional to $\sqrt{N}$. (b) The relative standard deviation of calculated lifetime over 10 measurements decreases with the increase of averaged pulse numbers, which is inversely proportional to $\sqrt{N}$. Therefore, more averaged pulses could improve the precision of lifetime measurement.

(f) Linearity, sensitivity and dynamical range

The linearity of the TRF subsystem depends on the response of the MCP-PMT and the preamplifier. It can be determined by evaluating the distortion of amplified output signal as a function of the amplitude of the input signal. To determine the linearity of the TRF subsystem, fluorescence signals of 10^{-5} M 9-cyanoanthracene (9-CA) solution at its emission peak at 435 nm were measured. The fluorescence signals were acquired at different amplitudes from 10 mV to 700 mV which corresponding to different PMT gains**.** The relationship between the amplitudes of fluorescence signals and the supply voltages is shown in Figure 3-22. The results were constant with the PMT response given by manufacturer. Moreover, the bandwidth (FWHM) of the decay signal kept constant at different signal levels (Figure 3-22) in the amplitude measurement range of the digitizer.

The sensitivity of the TRF subsystem was determined by measuring the fluorescence emission as the concentration of the fluorescence solution gradually decreased. The sensitivity is defined as the lowest fluorescein concentration that could yield accurate lifetime. The fluorescence emissions of the fluorescein solution were measured at different concentrations in the range of 10^{-3} -10^{-8} M. For each concentration, ten pulses at 515 nm were acquired. The SNR of the fluorescence decay for each concentration was calculated and is shown in Table 3-4. The lifetime value of the fluorescein is 4 ns. We can

see that our system is able to retrieve fluorescence lifetime values from the 10^{-7} M fluorescein solution with a SNR of 23.

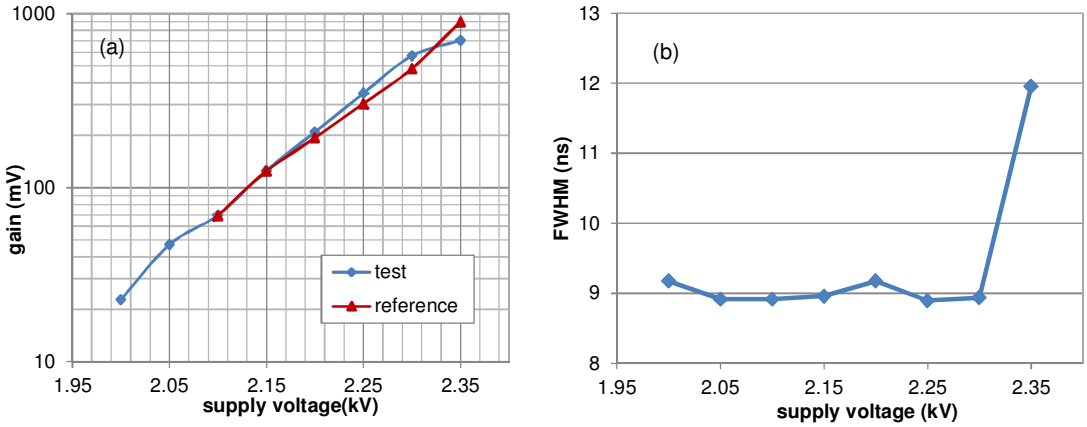

Figure 3-22. The linearity response of the TRF system. (a) The linearity of PMT gain and output signal (limited by the digitizer amplitude), (b) The relationship of the pulse width (FWHM) and the amplitude of output signal.

Table 3-4. Signal-to-noise ratio (SNR) and lifetime value of each concentration solution

concentration (M)	SNR	lifetime values (ns)
10^{-3}	664	3.9±0.1
10^{-4}	266	4.1±0.2
10^{-5}	148	4.1±0.2
10^{-6}	43	4.0±0.4
10^{-7}	23	3.8±0.5
10^{-8}	9	2.3±1.1

The signal dynamical range (D) of the TRF subsystem was calculated by

$$D = \frac{S_{max} - N}{N} \tag{3.10}$$

where S_{max} is the maximum signal level achievable without saturation in PMT and digitizer and N was the noise level of PMT [98]. The dynamical range of TRF subsystem determined in this way was 3 decades under the PMT high voltage of 2200 V.

3.2.2. DR subsystem calibration

It is important for the spectrometer to have a linear response to the amount of light captured for different intensity measurements. The linearity between spectrometer photon counts and input intensity was measured as shown in Figure 3-23. A halogen light source

was incident on a spectrometer via a fibre with 200 µm core. The spectrometer photon counts were measured as the input light power decreased within a constant integration time of 100 ms. The intensity of incident light was also measured by a power meter before it was measured by the spectrometer. This experimental result shows that the spectrometer response is linearly proportional to the incident light intensity before it saturated.

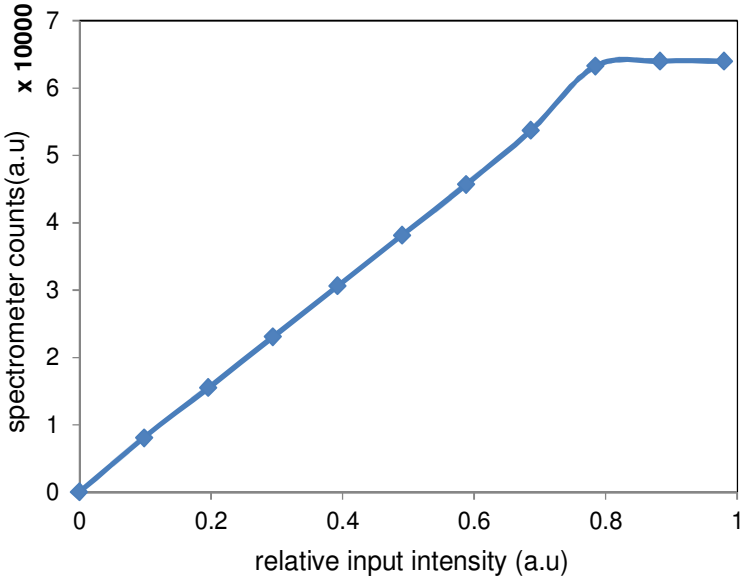

Figure 3-23. Linearity of the spectrometer. The spectrometer photon counts were measured with gradually change incident light intensity. The spectrometer measurement is linear proportional to the incident light intensity before the saturation.

3.3. Summary

The integrated TRF-DR spectroscopy instrument was developed for *in vivo* optical biopsy studies. The fluorescence lifetime and spectrum, as well as diffuse reflectance spectra could be collected by using a custom-made clinical sterilizable fibre optic probe in sequence within 2 s. The system spectral and temporal properties have been calibrated to optimize its performance.

The spectral resolved capability of the TRF subsystem was realized by using the AOTF-based spectrometer to switch the wavelength of diffracted beam within several microseconds. This configuration dramatically deceases the data acquisition time compared to the grating-based system used in the previous study [16]. Moreover, compared to band-pass filter-based configurations that collect fluorescence signals in limited spectral bands, this design allows us to choose the interested wavelength without

any physical modification of the setup. This ensures this system is much feasible to choose the different wavelengths according to clinical requirements. Time-resolved capability of the TRF subsystem is realized using a high sensitive MCP-PMT and a high-speed digitizer. The calibration results indicate that the TRF-DR system can retrieve the fluorescence decay signal down to a lifetime of a few hundred picoseconds.

In the DR subsystem, a broadband light source was designed by combining three UV LEDs and a halogen lamp, which can be used to investigate the optical properties of the biological tissue in the UV-VIS spectral range. Four independent spectrometers was used to acquire the spatially resolved diffuse reflectance signals at different source-detector distances as well as reference light. In this configuration, it is feasible to adjust the diffuse reflectance light intensity for each channel individually and quickly. The dual-modality fibre optic probe was used to retrieve the optical properties of the biological tissue accurately, meanwhile it also allows the collection of TRF and DR signals at the same location.

In the next chapter, the performance of the TRF-DR system that is validated using standard fluorescence dyes and fluorescence tissue phantoms will be presented in details.

Chapter 4

Integrated TRF-DR spectroscopy system validation

The development and calibration of the integrated TRF-DR spectroscopy instrument were described in Chapter 3, which demonstrated its potential to be used as an intraoperative tool for tumour margin detection. In this chapter, the performance of the system was validated using standard fluorescence dyes, biomolecules, and liquid tissue phantoms. The validation results of the TRF subsystem are presented in Section 4.1. The effects of optical properties on fluorescence signals were investigated using fluorescent liquid phantoms with different optical properties, and are presented in Section 4.2.

4.1. TRF subsystem validation

The performance of the TRF subsystem was validated through standard fluorescence dyes and biomolecules with well-characterized fluorescence spectral and lifetime properties. In this section, the sample preparation and measurement procedure are described, followed by the measurement results.

4.1.1. Sample preparation

The standard fluorescence dyes, which are in a broad emission wavelength range of 370-550 nm and a broad lifetime range of 2.5-12 ns, were used to validate the performance of the TRF subsystem. The fluorophores included 9-cyanoanthracene (9-CA) (emission peak: 445 nm, lifetime: 11.8 ns, 15276, Sigma-Aldrich, St Louis, MO), fluorescein (emission peak: 515 nm, lifetime: 4.1 ns, 46955, Sigma-Aldrich, St Louis, MO), coumarin-6 (emission peak: 500 nm, lifetime: 2.5 ns, 442631, Sigma-Aldrich, St Louis, MO), and Lucifer yellow (emission peak: 540 nm, lifetime: 5 ns, 62642, Sigma-Aldrich, St Louis, MO). The stock solution of each fluorescence dye with 10^{-3} M concentration was first prepared from its powdered form. The 9-CA, fluorescein, and coumarin-6 were dissolved in ethanol, while the Lucifer yellow was dissolved in NaOH. Stock solutions were further diluted into various concentrations used in the TRF measurement.

To evaluate the ability of TRF subsystem to detect the endogenous fluorescence signals from biological tissue, some biomolecules including β-Nicotinamide adenine dinucleotide reduced disodium salt hydrate (NADH, N8129, Sigma-Aldrich, St Louis, MO), flavin adenine dinucleotide disodium salt dehydrate (FAD, F6625, Sigma-Aldrich, St Louis, MO), and collagens I and III, were measured. The NADH and FAD were dissolved in 10^{-5} M phosphate buffered saline (PBS) solutions individually, and the collagens were measured in powdered form. All samples were kept refrigerated before and after measurement.

4.1.2. Measurement procedure

These liquid solutions were measured in plastic cuvettes (1 cm ×1 cm × 4 cm). The fibre optic probe tip was positioned perpendicularly at 1 mm above the surface of solution. The collagens were placed in a non-fluorescent petri dish. The fibre probe was in direct contact with the surface of the collagens. The laser pulse energy at the fibre probe tip was measured using a power meter (3-sigma, Coherent, Santa Clara, CA) before fluorescence measurements and was adjusted to 2.5 μJ and 2 μJ for standards fluorescence dyes and biomolecules respectively to avoid photobleaching. Fluorescence decay signals at 37 wavelengths in the wavelength range of 370-550 nm with 5 nm intervals were measured to generate a steady-state fluorescence spectrum. Fluorescence lifetime values were calculated using deconvolution methods, while fluorescence intensity was calculated by integrating the decay over the acquisition time at each wavelength.

4.1.3. Results

(a) System validation on fluorescence standards

Four standard fluorescence dyes were measured by the TRF subsystem. The background measured from the pure ethanol or NaOH solution under the same measurement procedure was subtracted from the steady-state fluorescence spectra. The lifetime value at the emission peak of each sample was calculated using both Laguerre-based deconvolution and single exponential deconvolution methods as summarized in Table 4-1. The lifetime values calculated using the Laguerre-based deconvolution method had larger standard deviations than the results of the single exponential deconvolution method, but both calculation results were in agreement with Refs [16,95]. These results indicate that the TRF subsystem has the ability to resolve the fluorescence lifetime accurately.

Table 4-1. Lifetime values of Standard Fluorescence dyes

Fluorophore	Solution	Fitting results (ns)		Reference (ns)16
		Exponential	Laguerre	
9-CA	Ethanol	11.5±0.4	11.8±1.9	11.7-11.85
Fluorescein	Ethanol	4.1±0.1	4.1±0.8	4.1
Coumarin-6	Ethanol	2.9±0.1	3.1±0.6	2.5
Lucifer yellow	NaOH	4.9±0.1	5.1±0.9	4.9~5.7

Autofluorescence signals from biological tissue are usually contributed by several endogenous fluorophores that have the overlapped emission spectra. To demonstrate the ability of the TRF subsystem to resolve the fluorescence from a sample with complex fluorescent components, a series of mixed solutions with two distinct fluorophores was prepared. The first group of mixed solution included 1 mL of 10^{-4} M 9-CA and 1 mL of 10^{-3} M fluorescein. These two fluorescent dyes have distinct emission wavelengths and lifetime values. As shown in Figure 4-1, 9-CA and fluorescein can be resolved spectrally and temporally from the fluorescence spectrum and lifetime values of the mixed solution. Two intensity peaks at 445 nm and 515 nm were observed in the spectrum corresponding to the emission peaks of 9-CA and fluorescein respectively. The lifetime value of 11.95 ns at 445 nm was mainly contributed by 9-CA, whereas the lifetime value of 4 ns at 515 nm that was predominantly contributed by fluorescein. In addition, the lifetime values changed with the emission contribution ratio of these two fluorophores in the spectral range of 480-520 nm as the green curve shows.

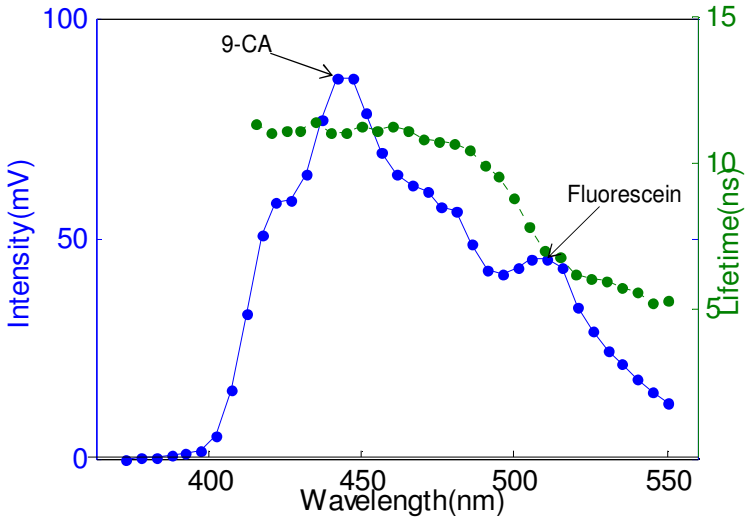

Figure 4-1. The spectrum and lifetime of the mixed solution of 10^{-4} M 9-CA and 10^{-3} M fluorescein with the volume ratio of 1:1. Two emission peaks (black arrows) are found at 445 nm and 515 nm in the spectrum

corresponding to the emission peak of 9-CA and fluorescein respectively. The lifetime decreases from 11.95 ns at 445 nm to 4 ns at 515 nm corresponding to the changes in the contribution ratio.

To investigate the relationship between fluorescence lifetime and different fluorophores contributions in overlapped emission spectra, the other group of mixed solutions of fluorescein and coumarin-6 with the same emission spectrum but distinct lifetime values were prepared. Five different mixed solutions with various concentration ratios of fluorescein and coumarin-6: 1.0/0, 0.75/0.25, 0.5/0.5, 0.25/0.75, and 0/1.0, were measured by the TRF subsystem. Both fluorescein and coumarin-6 had a strong emission between 510 nm and 530 nm (Figure 4-2a). The averaged lifetime values for these five solutions were linearly proportional to the change of the concentration ratio (Figure 4-2b). These results illustrate that our system is able to retrieve the relative contributions of different fluorescent components quantitatively.

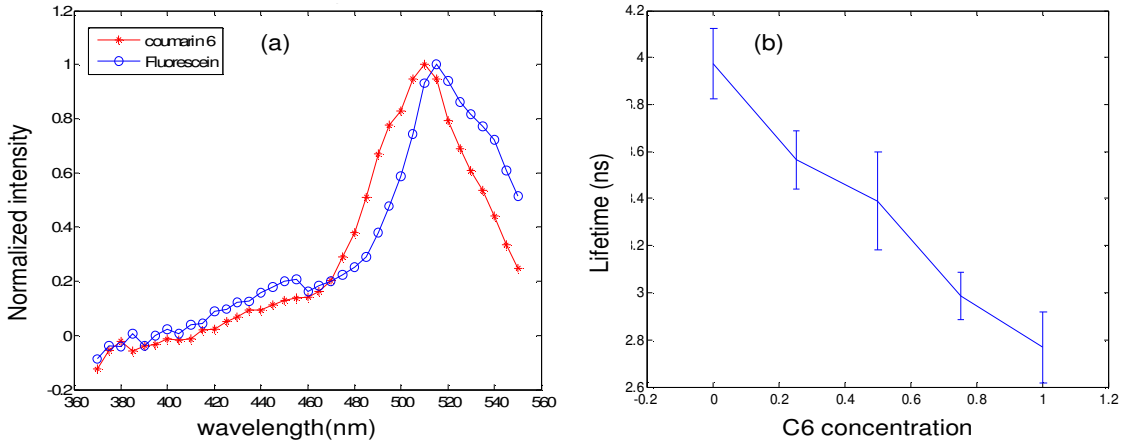

Figure 4-2. Fluorescence spectra and lifetime values of the mixed solutions with different concentration ratios. (a) The emission spectra of fluorescein and courmain-6. (b) Fluorescence lifetime values of the mixed solutions linearly varied with the concentration ratio.

(b) System validation on biological molecules

The capability of the TRF subsystem in resolving the endogenous fluorescence of biological tissue was validated using several biological molecules including NADH, FAD, and collagens type I and type III. The fluorescence decay curves were fitted by the Laguerre-based deconvolution method and bi-exponential deconvolution method to retrieve intrinsic response functions. The fluorescence spectra and lifetime of the biomolecules are shown in Figure 4-3. In this figure, the NADH has a broadband emission spectrum with an emission peak at 450 nm and lifetime of 0.61 ns, while FAD has the relatively narrow emission spectrum with an emission peak at 520 nm and lifetime of 2.91 ns. The lifetime values of FAD decreased at the short wavelengths due to

the low signal-to-noise ratio. The emission peak was around 440 nm for both collagens I and III, whereas the lifetime values are distinct. Collagen type III had a larger lifetime value than collagen type I. In addition, the lifetime of collagen I decreased quickly at the longer wavelengths compared to collagen type III. The lifetime values of the biological molecules agreed with Ref [16] except that the NADH had higher value than reported results, which was limited by the temporal resolution of the TRF subsystem. However, NADH is usually bonded with protein in cells or tissue and the lifetime of NADH changes according to its bonding status. For example, the fluorescence lifetime of NADH in mitochondria (2.8 ns) was much longer than that of pure solution (0.43 ns) [41]. Therefore, the TRF subsystem is capable of retrieving the NADH component from biological tissue. Collagen usually has short and long lifetime components that can be observed from the bi-exponential fitting results. These results indicate that our TRF subsystem is able to retrieve the spectral and lifetime characteristics of biomolecules that are the endogenous fluorophores in biological tissue.

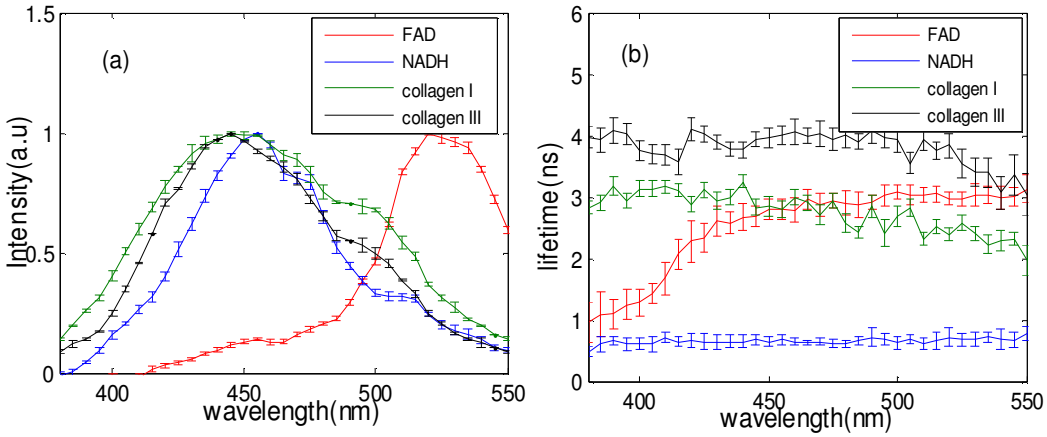

Figure 4-3. TRF subsystem characterization on the biological molecules. (a) The spectra of NADH, FAD and Collagens (type I and III) with emission peaks at 450 nm, 520 nm, 445 nm, and 445 nm, respectively. (b) The lifetime values for the different biological molecules over the observed spectral range.

Table 4-2. Endogenous fluorophores lifetime measurements

Fluorophore	Lifetime (ns)			Reference [16]	
	Laguerre	Bi-exponential			
FAD	2.9 ± 0.1	---		2.3~2.86	
NADH	0.6 ± 0.1	---		0.3~0.4	
Collagen I	2.8 ± 0.1	1.0 ± 0.1	5.1 ± 0.3	0.6	4.9

4.2. Effect of optical properties on fluorescence signals

Using quantitative fluorescence spectroscopy for optical biopsy studies is challenging due to the difficulties in interpreting fluorescence signals in biological tissue having high scattering and absorption properties. Therefore, the measured fluorescence signals may not reflect the real features of endogenous fluorophores. In order to investigate the effects of optical properties on the fluorescence measurements, several experiments were carried out using tissue-simulating phantoms with different optical properties.

4.2.1. Tissue phantoms preparation

A series of tissue-simulating liquid phantoms was prepared to reveal the effects of optical properties on the fluorescence measurements. Intralipid (20%, Baxter Corp, Toronto, Canada) was used as a scattering material, while India ink was used as the absorber. The Intralipid and India ink were diluted by deionized water to obtain different concentrations. Two sets of liquid phantoms were prepared. The optical properties of these tissue-simulating phantoms were measured using a steady-state spatially resolved diffuse reflectance system [96].

In order to investigate the effect of the scattering coefficients on the fluorescence spectral and lifetime measurements, the first phantom group (group A) was prepared with the same absorption coefficient and different scattering coefficients. The India ink with a concentration of 0.003% v/v was used for each phantom to obtain a constant absorption coefficient of 0.02 mm^{-1}. The Intralipid concentration of 1% v/v, 1.2% v/v and 1.4% v/v were used in different phantoms corresponding to the reduced scattering coefficients of 1.5 mm^{-1}, 1.8 mm^{-1}, and 2.1 mm^{-1} at 515 nm. In order to investigate the effect of the absorption coefficient on the fluorescence measurements, the second phantom group (group B) with same scattering coefficient and different absorption coefficients was prepared. The Intralipid concentration of each phantom was 1.2% v/v to obtain a reduced scattering coefficient of 1.8 mm^{-1}. The India ink concentration varied from 0 to 0.012% v/v to obtain the absorption coefficients in the range of 0 to 0.06 mm^{-1} at 515 nm in different phantoms.

The fluorescein with an emission peak at 515 nm and a lifetime value of 4.1 ns was added into these liquid phantoms to obtain a concentration of 0.1 mM. The optical properties of the fluorescent phantoms were also measured after adding the fluorescein dye in order to confirm that the fluorescein dye did not affect the optical properties.

4.2.2. Measurement procedure

The steady-state fluorescence spectra were measured using the grating-based

spectrometer, while the fluorescence decay signals at 515 nm were collected using the AOTF-based spectrometer. The liquid phantom with a volume of 4 mL was measured in a plastic cuvette (1 cm × 1 cm × 4 cm) for which the size was much larger than the transport mean free path at wavelengths of interest. The fibre probe was in contact with the surface of the liquid solution perpendicularly. Five steady-state spectra and 2000 fluorescence decays were acquired for each phantom. The background fluorescence signal of each phantom (contributed by the Intralipid) was also measured and subtracted from the steady-state fluorescence spectra.

4.2.3. Results

(a) Effect of scattering properties

To investigate the effect of the scattering property on the fluorescence signal measurement, the fluorescence spectra and decays were collected from the phantom group A. The steady-state fluorescence spectrum and normalized decay curve of each phantom are shown in Figure 4-4. It is observed that the spectral shape did not change with the reduced scattering coefficient, while the fluorescence intensity decreased with the increase of the reduced scattering coefficient (Figure 4-4a). The fluorescence decay curve did not have significant differences at different reduced scattering coefficients. The lifetime values are shown in Table 4-3. The lifetime values calculated from the fluorescence decay signal kept constant over the reduced scattering coefficients when a digitizer with the sampling rate of 3.6 GS/s was used to acquire the fluorescence signals. The standard deviation of the lifetime value decreased due to the decrease of signal-to-noise ratio of the fluorescence signal.

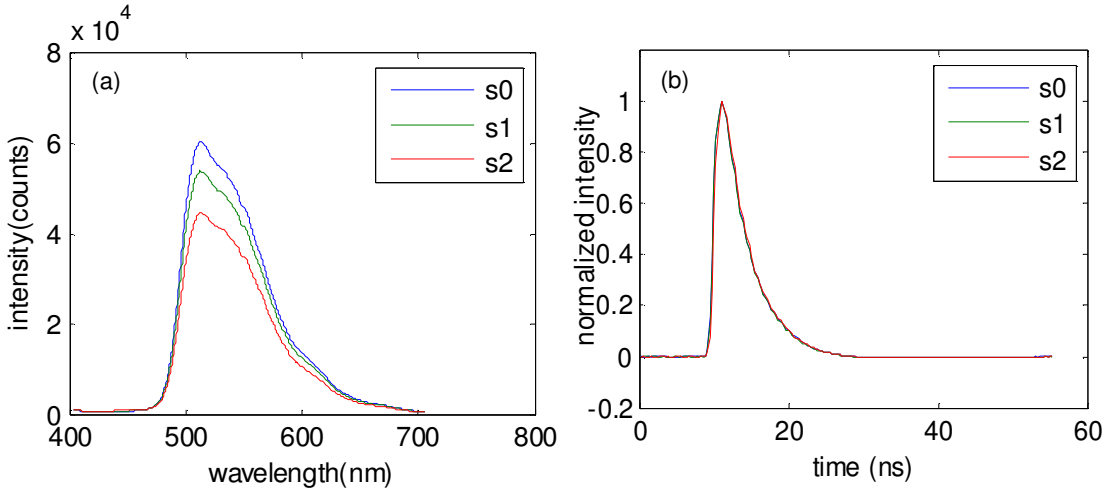

Figure 4-4. The fluorescence signals measured from liquid phantoms with different scattering properties. (a) Fluorescence emission spectra. (b) Fluorescence decays are normalized at peak intensity. The fluorescence

decay curve did not change with the reduced scattering coefficient, while the fluorescence decay curve did not change with the reduced absorption coefficient.

Table 4-3. Fluorescence lifetime estimation for the phantom group A with different reduced scattering coefficients

Phantom label	Optical properties @515nm		Fluorescein Concentration (mM)	Lifetime (ns)
	Reduced scattering (mm^{-1})	Absorption (mm^{-1})		
s0	1.5	0.02	0.1	4.1 ± 0.1
s1	1.8	0.02	0.1	4.0 ± 0.1
s2	2.1	0.02	0.1	4.0 ± 0.1

(b) Effects of absorption properties

To understand the effect of absorption on fluorescence spectra and decay signals, the tissue phantom (group B) was measured. Figure 4-5a presents the fluorescence spectra of five tissue phantoms with different absorption coefficients. With the increase of absorption coefficients, the fluorescence intensity decreased gradually, whereas the fluorescence decays did not change as shown Figure 4-5b. The fluorescein lifetime values calculated from the fluorescence decays of the different tissue phantoms are presented in Table 4-4, which are in good agreement with the lifetime value in the pure fluorescence solution. Optical properties of each liquid phantom are also presented in Table 4-4.

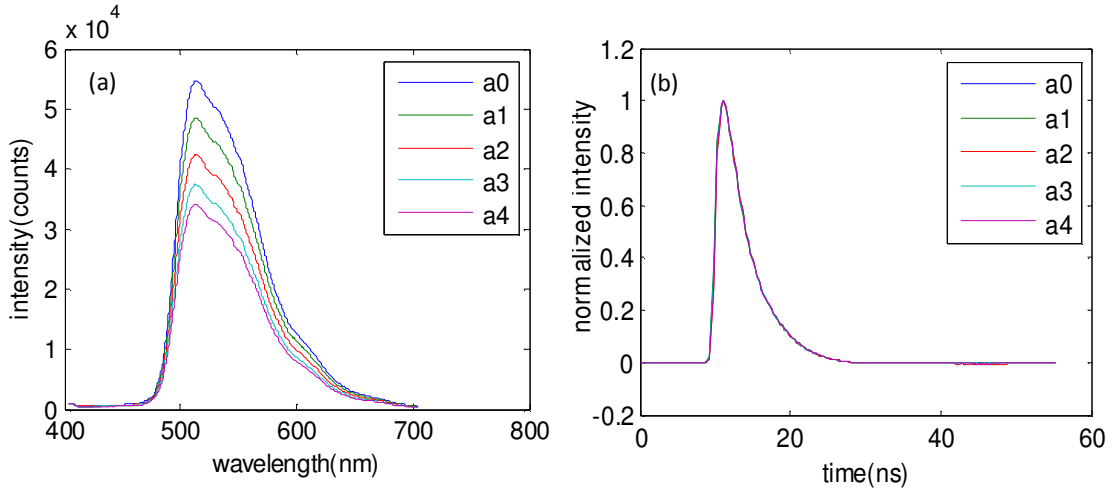

Figure 4-5. The fluorescence signals measured from the liquid phantoms with same scattering properties but different absorption properties. (a) Fluorescence emission spectra. (b) Fluorescence decays were normalized at peak intensity. The spectra intensity decreased with the absorption coefficients, while the fluorescence decay curve did not change with the absorption properties.

Table 4-4. Fluorescence lifetime estimation for the phantom group B with different absorption coefficients

Sample label	Optical properties @ 515 nm		Fluorescein Concentration (mM)	Lifetime (ns)
	Reduced scattering (mm^{-1})	Absorption (mm^{-1})		
a0	1.8	0	0.1	4.0 ± 0.1
a1	1.8	0.02	0.1	3.9 ± 0.1
a2	1.8	0.04	0.1	3.9 ± 0.1
a3	1.8	0.05	0.1	3.9 ± 0.1
a4	1.8	0.06	0.1	3.9 ± 0.1

The effects of optical properties on the fluorescence measurements were investigated experimentally in this section. The experimental results showed that by using the single optical fibre for laser illumination and fluorescence collection, the fluorescence lifetime did not change with the optical properties, whereas the fluorescence intensities were altered by the scattering and absorption properties. These results were in good agreement with simulation and experiment results in Ref [83] in which a Monte Carlo model was used to simulate the fluorescence transmission in the turbid tissue with various optical properties [83]. Therefore, only the distortion of the fluorescence intensity needs to be corrected from measured fluorescence signals in our future studies.

4.3. Summary

This chapter demonstrates the performance of the integrated TRF-DR spectroscopy using the tissue phantoms. The integrated TRF-DR spectroscopy system is capable of retrieving the fluorescence features accurately from the standard fluorescence dyes and biological molecules. According to fluorescence measurements under different scattering and absorption conditions, fluorescence lifetime is much more robust with the changes in optical properties when the single optical fibre is used for laser illumination and fluorescence collection. However, the fluorescence intensity is significantly altered by the changes in optical properties. Therefore, to obtain intrinsic fluorescence information of biological tissue, it is necessary to retrieve the intrinsic fluorescence spectral intensity from the turbid tissue.

Chapter 5

A Robust Laguerre-based deconvolution method for biological fluorescence decay

Autofluorescence signals of biological tissue are contributed by several endogenous fluorophores with overlapped emission spectra. In addition, the autofluorescence signals usually have low signal-to-noise ratio compared to the signals from exogenous fluorescent dyes. Therefore, an accurate and fast method is needed to retrieve the fluorescence lifetime and amplitudes from measured fluorescence signals. Multi-exponential-based deconvolution methods are mostly used to retrieve the fluorescence characteristics with a specific assumption of a decay function. However, Laguerre-based deconvolution methods, based on the orthonormal Laguerre functions, do not need any assumption of a decay function and can provide a unique fitting result. Thus, the Laguerre-based deconvolution methods may be used as alternative methods to the multi-exponential-based methods for clinical studies. The original Laguerre function (OLF)-based deconvolution method provides a way to estimate the IRF quickly, but it often fails when the decay signal has low signal-to-noise ratio [107]. In order to solve this problem, in this chapter, a robust constraint Laguerre function (CLF)-based deconvolution method is optimized by constraining the least squares fitting using fluorescence decay profiles. In addition, a fast Laguerre parameters selection method is developed to enable real-time data analysis during clinical studies.

Detailed fluorescence lifetime acquisition mechanisms and deconvolution methods are presented in Section 5.1. The mathematical models of the CLF-based deconvolution method are presented in Section 5.2. Moreover, a series of Laguerre parameters such as Laguerre scale parameter α and the total number of Laguerre functions are discussed in Section 5.3 in order to optimize the fitting performance. A look-up table was created to select suitable Laguerre scale parameters in real-time. Finally, CLF-based deconvolution method was performed using standards fluorescence dyes and biological molecules in Section 5.4.

5.1. Introduction

5.1.1. Time-resolved fluorescence deconvolution

The time-resolved fluorescence (TRF) technique, which acquires the dynamic fluorescence decay signal over a certain time scale, is used extensively to monitor the changes of biochemical compositions and structures in tissues and cells [6]. Once a short laser pulse excites the biological sample, the fluorescence light that is emitted from the biological sample is collected by a TRF system. The measured fluorescence decay is usually altered by both the system response and the laser pulse. As illustrated in Figure 5-1, the measured fluorescence pulse $F(t)$ can be described as the convolution of the excitation laser pulse I_0(t), the fluorescence impulse response function IRF(t), and the system response function S(t):

$$F(t) = I_0(t) \otimes IRF(t) \otimes S(t) \tag{5.1}$$

Practically, the excitation pulse $I_0(t)$ is usually measured using the same TRF system. Thus, the measured excitation pulse $I(t)$ from TRF system is actually the convolution of $I_0(t)$ and $S(t)$. Therefore, the measured fluorescence signal $F(t)$ can be described as the convolution of $I(t)$ with $IRF(t)$ [16].

$$F(t) = I(t) \otimes IRF(t) \tag{5.2}$$

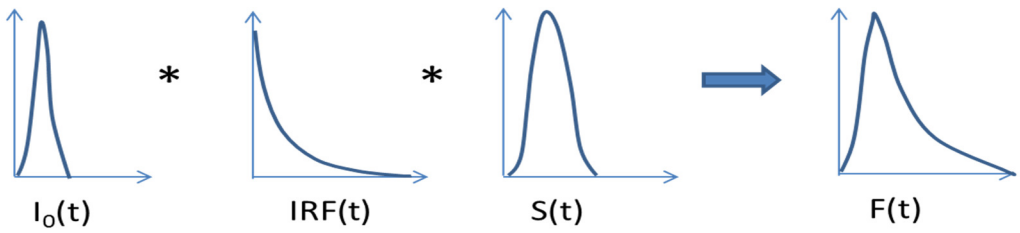

Figure 5-1. The deconvolution mechanism for the TRF measurement. I(t): the excitation laser pulse, IRF(t): the impulse response function of fluorescence, S(t): the system response function.

5.1.2. Deconvolution methods for IRF

An accurate and fast method plays an important role in retrieving the IRF from the measured fluorescence signal. A number of deconvolution methods have been investigated for this purpose [92, 101-109]. Some of these methods assume a specific function form of the fluorescence decay curve, such as multi-exponential deconvolution [101]. In contrast, some methods retrieve the IRF without any direct assumption, such as the stretched exponential method [102], the Fourier [103] and Laplace transform methods [104], as well as the Laguerre function (LF)-based deconvolution methods [92,109].

Multi-exponential methods are commonly used to estimate the fluorescence lifetime of biological samples [15]. However, the multi-exponential methods are limited in three aspects when estimating the fluorescence properties of clinical data. First, it is very hard to assume an exact exponential model for the autofluorescence signals which are contributed by the complex endogenous fluorophores in biological samples. Second, the fitting result is not unique due to the non-orthogonal exponential functions. Hence, the fitting result may not give a correct physical interpretation of the fluorescence signal. Third, the multi-exponential models use a nonlinear least squares fitting that is time-consuming and hence may not be suitable for real-time clinical studies.

The Laguerre-based deconvolution method use a set of Laguerre functions to predict the IRF of the measured fluorescence signal. It has been used to retrieve fluorescence properties in many studies [6, 92]. Several distinct properties of the Laguerre functions make it much more suitable to fit the fluorescence decays:

- The Laguerre functions are a complete orthonormal basis over the time interval of [0, ∞). This property guarantees the uniqueness of the fitting result for fluorescence decays in the time-domain.
- The exponential components in the Laguerre functions make this basis more suitable for exponential decay signals [105].
- The Laguerre-based deconvolution method is based on the linear least squares fitting which is much faster than the nonlinear least squares fitting used in the multi-exponential method because the regression in the nonlinear least squares fitting is time-consuming.

A recent study also demonstrated that the Laguerre-based deconvolution method achieves the best sensitivity compared to other deconvolution methods such as the bi-exponential deconvolution method or the area-under-the-intensity method [106]. However, there are still limitations when applying the Laguerre-based deconvolution method in biological measurements.

- Larger number of data points for the fluorescence decay acquisition are needed to satisfy the orthonormality of LFs, however, this prolongs the data acquisition time.
- The lifetime values of the autofluorescence are in the range of hundreds of picoseconds to several nanoseconds. This means different Laguerre scale parameters are required for different fluorescence signals to obtain the optimal fitting results.
- High-order LFs are usually able to resolve the fluorescence decay with complex components. However, high-order LFs basis introduces an oscillation in the fitting

results and causes an over-fitting problem especially for data with low SNR [107].

In order to solve the problems of the Laguerre-based deconvolution method, Liu *et al*. [107] presented a simple solution by using the physical profiles of the fluorescence decay to constrain the fitting process. This method can be used to keep the fitting results smooth, but it still fails under the low signal-to-noise condition. Therefore, in this chapter, we further optimized the Laguerre-based deconvolution method to address this problem. In addition, a fast Laguerre parameters selection method was developed to enable real-time data analysis during clinical studies. The performance of method was validated through simulations and experimental data.

5.2. Theory

5.2.1. Laguerre-based deconvolution model

In a TRF spectroscopy system, a fluorescence decay is digitized by a high-speed digitizer to obtain the discrete digital signal. Therefore, the relationship of the measured fluorescence signal and the IRF in Eq.(5.2) can be rewritten as:

$$y(n) = \mathrm{T}\sum_{m=0}^{K-1} h(m)x(n-m) \quad n=0,.....K-1. \tag{5.3}$$

where *K* is the data length, *T* is the data sampling interval, *h(m)* is the fluorescence IRF, *x(m)* is the measured laser pulse, and *y(n)* is the measured fluorescence signal. The IRF, *h(m),* can be expressed using the discrete LF basis:

$$h(n) = \sum_{j=0}^{L-1} C_j b_j^{\alpha}(n) \tag{5.4}$$

where $b_j^{\alpha}(n)$ is the j^{th} order LF, C_j is the Laguerre expansion coefficient (LEC) that is indicated the contribution of the j^{th} order LF in the fitting result, and *L* is the total numbers of LFs used in the IRF fitting. $b_j^{\alpha}(n)$ is defined as:

$$b_j^{\alpha}(n) = \alpha^{\frac{n-j}{2}}(1-\alpha)\sum_{k=0}^{j}(-1)^k \binom{n}{k}\binom{j}{k}\alpha^{j-k}(1-\alpha)^k \; n \geq 0 \tag{5.5}$$

in which α is the Laguerre parameter within the range of 0-1. The number of zero-crossings of each Laguerre function equals its order as shown in Figure 5-2a. In addition, the zero order of LFs with different α is shown in Figure 5-2b. As indicated in the figure, the convergence speed of the Laguerre function decreased with the increase of the α. It is also observed that the peak amplitude of the Laguerre function increases with the decrease of α. Therefore, it is possible to obtain an optimal fitting result by choosing a suitable α. In addition, the Laguerre functions are an orthonormal polynomial basis,

where $[b_j^{\alpha}(n)]^T \cdot b_j^{\alpha}(n) = 1, [b_j^{\alpha}(n)]^T \cdot b_i^{\alpha}(n) = 0$, *i,j*=1..*M*. This property ensures the uniqueness of the fitting result at certain *L* and α. By inserting Eq.(5.5) to Eq.(5.4), the measured fluorescence signal can be rewritten as:

$$y(n) = T\sum_{m=0}^{k-1}\left(\sum_{j=0}^{L-1} c_j\, b_j^{\alpha}(m)\right)x(n-m)$$

$$= \sum_{j=0}^{L-1} c_j \left(T\sum_{m=0}^{k-1} b_j^{\alpha}(m)x(n-m)\right)$$

$$= \sum_{j=0}^{L-1} c_j v_j\,(n) \tag{5.6}$$

where $v_j(n) = T\left(\sum_{m=0}^{k-1} b_j^{\alpha}(m)x(n-m)\right)$ is the convolution of the excitation laser pulse with the Laguerre basis. Eq. (5.6) can also be rewritten as:

$$\begin{bmatrix} y(0) \\ y(1) \\ \vdots \\ y(K-1) \end{bmatrix} = \begin{bmatrix} v_0^{\alpha}(0) & v_1^{\alpha}(0) & \cdots & v_{L-1}^{\alpha}(0) \\ v_0^{\alpha}(1) & v_1^{\alpha}(1) & \cdots & v_{L-1}^{\alpha}(1) \\ \vdots & \vdots & \ddots & \vdots \\ v_0^{\alpha}(K-1) & v_0^{\alpha}(K-1) & \cdots & v_{L-1}^{\alpha}(K-1) \end{bmatrix} \times \begin{bmatrix} c_0 \\ c_1 \\ \vdots \\ c_{L-1} \end{bmatrix} \tag{5.7}$$

Eq.(5.7) can be further simplified as:

$$y = VC \tag{5.8}$$

in which *V* is a matrix with dimension of *K*×*L*, $C = [c_0, c_2, c_3 \ldots c_{L-1}]^{-1}$ is the Laguerre expansion coefficient vector, and *y* is the estimated decay curve. Therefore, the least squares fitting problem can be written as:

$$\text{Minimize } W\|\hat{y} - VC\|^2 \tag{5.9}$$

where *W* is weight factor that can be estimated by the $1/\delta^2$, in which δ^2 is the variance of the fluorescence signals that can be obtained from repetitive measurements [108], and $\hat{y}$ is the measured signal. Finally, the *C* can be solved as:

$$C = (V^T W V)^{-1} V^T W \hat{y} \tag{5.10}$$

5.2.2. The relationship between LECs and fluorescence compositions

Once the Laguerre expansion coefficients are obtained, the intrinsic fluorescence decay can be written as:

$$h(n) = \sum_{j=0}^{L-1} c_j b_j^{\alpha}\,(n) \tag{5.11}$$

The relationship of the LECs and the fluorescence composition was described by Jo *et al.* [92]. Each fluorescent component contributing to the measured fluorescence signal can

be predicted by the Laguerre function as:

$$S_k(n) = \sum_{j=0}^{L-1} a_{k,j} b_j^{\alpha}(n), k = 1..M \quad (5.12)$$

where S_k(n) is the normalized IRF of the k^{th} fluorescence decay component and $a_{k,j}$ is the Laguerre coefficient for the k^{th} fluorescence component. The IRF of the measured fluorescence decay $h(n)$ is the weighted sum of the normalized IRF of each fluorophore as:

$$h(n) = \sum_{k=1}^{M} A_k s_k(n) \quad (5.13)$$

where A_k is the contribution of the k^{th} components. Thus, by inserting Eq.(5.12) into Eq.(5.13), the IRF $h(n)$ can be expressed as:

$$h(n) = \sum_{k=1}^{M} A_k \left(\sum_{j=0}^{L-1} a_{k,j} b_j^{\alpha}(n)\right) = \sum_{j=0}^{L-1} \left(\sum_{k=1}^{M} A_k a_{k,j}\right) b_j^{\alpha}(n) \quad (5.14)$$

Comparing Eq.(5.14) with Eq.(5.11), the relationship between the Laguerre coefficients and the contribution of fluorescence components can be described as:

$$c_j = \sum_{k=1}^{M} A_k a_{k,j} \quad (5.15)$$

In practice, if we know the components of the measured fluorescence signal, $a_{k,j}$ can be estimated by fitting the intrinsic fluorescence for the individual component. Thus, the relative contribution of the individual biochemical component A_k can be calculated from Eq.(5.15). It is worth pointing out that this method only works when the fluorescence component number is less than the total number of Laguerre functions in the fitting to obtain a unique solution.

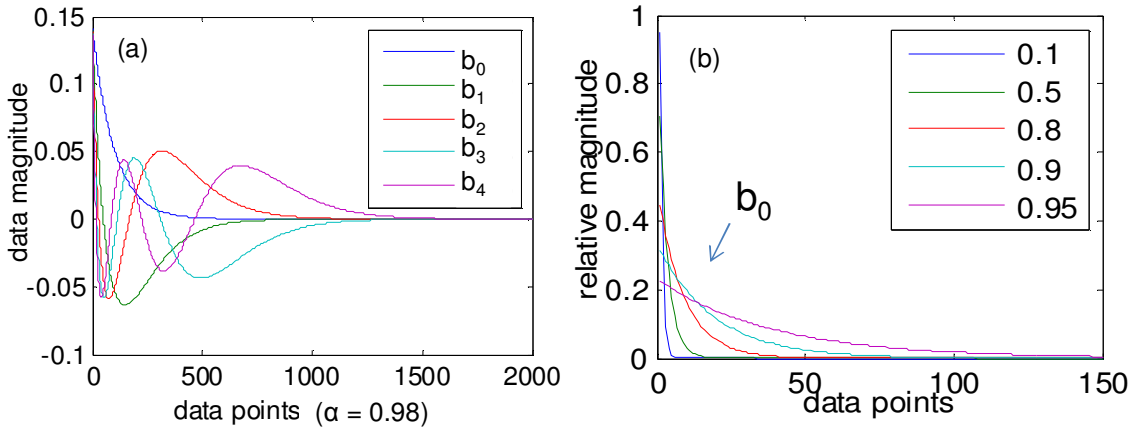

Figure 5-2. Laguerre functions. (a) First five orders Laguerre functions with α=0.98. (b) Zero order Laguerre function b_0 with various α values.

5.2.3. Laguerre-based deconvolution optimization

The solution obtained from Eq. (5.10) is called the OLF-based deconvolution method. This is not ideal for fluorescence signals with low SNR, where an attempt is made to fit the noise and hence introduces an oscillation phenomenon in the fitting results. To address these problems, the profiles of fluorescence decays may be used to constrain the least squares fitting in Eq.(5.9). As we mentioned in Section 2.4, the IRF of a complex fluorescence decay can be considered as a sum of many single exponential decays as:

$$h(t) = \sum_{i=1}^{M} A_i e^{-t/\tau_i}, \text{ i=1...}M \tag{5.16}$$

where A_i and τ_i are the amplitude contribution and lifetime for each component respectively. $h(t) \geq 0$ when t is in the time interval of $[0, \infty)$. The first order and second order derivatives of $h(t)$ can be expressed as :

$$h'(t) = (-1)\sum_{i=1}^{M} \frac{A_i}{\tau_i} e^{-t/\tau_i}, \text{ i=1...}M \tag{5.17}$$

$$h''(t) = \sum_{i=1}^{M} \frac{A_i}{\tau_i^2} e^{-t/\tau_i}, \text{ i=1...}M \tag{5.18}$$

Both A_i and τ_i are larger than zero, such that $h'(t) \leq 0$ and $h''(t) \geq 0$. Thus, two intrinsic properties of fluorescence decay profiles can be observed: (i) the fluorescence decay is a monotonic non-increasing function in the interval $0 \leq t < \infty$; and (ii) the decay slope of $h(t)$ decreases over the time scale. In order to use these two properties to constrain the least squares fitting (Eq.(5.9)), the third derivative of $h(t)$ was introduced. Thus, the properties can be expressed as:

(a)*:* $lim_{t\to\infty} h(t) = 0, lim_{t\to\infty} h'(t) = 0, lim_{t\to\infty} h''(t) = 0,$

(b)*:* $h'''(t) \leq 0$, $h'''(t)$ *is the third derivative of* $h(t)$.

Liu *et al*. [107] applied the constraint (b) to the least squares fitting in Eq.(5.9), but actually cannot satisfy the $h'(t) \leq 0, h''(t) \geq 0$ during the fitting process. By adding other constraints simplified from (a): $\lim_{t\to\infty} h''(t) = 0$, on the fitting processing, the properties of $h'(t) \leq 0, h''(t) \geq 0$ can be achieved. Hence, the least squares fitting subjected to constraints (a) and (b) are used in this study. A constrained least squares fitting process can be used to predict the Laguerre expansion coefficient C:

$$\begin{aligned} &\text{Minimize } W\|\hat{y} - VC\|^2 \\ &\text{Subject to } (BC)''' \leq 0, lim_{t\to\infty}(BC)'' = 0 \end{aligned} \tag{5.19}$$

where W is the weighted factor, B is the Laguerre function matrix which has dimension of

$K \times L$, and C is the Laguerre expansion coefficient vector. In addition, this method also requires the fluorescence decay to fall to zero at the end of the data length in order to satisfy constraint (b). The problem in Eq.(5.19) is solved by using the Matlab function *lsqlin*, in which an active-set regression algorithm is used to search the optimization results under the constraints [110]. Once the Laguerre expansion coefficient C is estimated, the IRF $h(k)$ can be computed from Eq.(5.4), while the average lifetime can be calculated as:

$$\tau_{avg} = \frac{T.\sum_{n=0}^{K} k \cdot h(k)}{\sum_{n=0}^{K} h(k)}, \tag{5.20}$$

where K represents the data length of the decay curve and T is the sampling time interval. The algorithm was implemented in MATLAB®. A flowchart of the Laguerre-based deconvolution method is shown in Appendix III.

5.3. Optimization of Laguerre functions

The parameters in the Laguerre-based basis, including the data length, the Laguerre scale parameter α, and the Laguerre orders, play very critical roles towards attempting an accurate fit of the fluorescence decay signal. A series of studies was carried out to optimize these parameters in order to choose a suitable Laguerre-based. Section 5.3.1 describes the simulated data and the optimal parameters are described in Section 5.3.2.

5.3.1. Simulation data

In order to validate the performance of the Laguerre-based deconvolution method, a number of decays with different lifetimes were simulated using single- or multi-exponential functions as:

$$h(t) = A_i \sum_{i=1}^{M} e^{-t/\tau_i} \tag{5.21}$$

where t is the sampling point of the fluorescence signal (in the TRF subsystem, the total sample points are 200 with the sampling intervals of 278 ps); M is the number of exponential components; A_i is the relative amplitude contribution of each component and $\sum_{i=1}^{M} A_i = 1$; τ_i is the lifetime value for the i^{th} exponential component. The lifetime values of simulated decays are in the range of 0.5-6 ns, which are similar to the lifetime values of endogenous fluorescence from biological tissue [16]. The fractional contribution for the i^{th} component is given by:

$$f_i = \frac{A_i \tau_i}{\sum_{k=1}^{M} A_k \tau_k} \times 100\% \ , i = 1, \ldots, M \tag{5.22}$$

in which $\sum_{i=1}^{M} f_i$=1. The averaged lifetime can be calculated as:

$$\tau_{avg} = \sum_{i=1}^{M} f_i \, \tau_i \tag{5.23}$$

To simulate the TRF measurement, the simulated intrinsic fluorescence signal is convolved with the measured laser pulse $I(t)$. In addition, the random noise and timing-jitter introduced by the TRF subsystem were also considered in the simulations as expressed in Eq.(5.21)

$$F(t) = \left\{ \mathrm{I(t)} \otimes \sum_{i=1}^{K} e^{-t/\tau_i} + N \right\} \otimes J \tag{5.24}$$

where N is the noise and J is the jitter. Different noise levels are added to the simulated data to obtain different SNRs in the range of 10-100 based on actual experimental data. A timing-jitter of 100 ps is also considered in the data simulation.

5.3.2. Parameters optimization

The parameters of the Laguerre-based deconvolution, including the data truncation length, the Laguerre scale parameter α, and the total numbers of Laguerre functions L, must to be considered before conducting the deconvolution. These parameters are chosen based on two practical conditions. First, averaged lifetime values of the endogenous fluorophores often vary in a large range from a few hundreds of picoseconds (*e.g.* 0.4 ns for free NADH) to several nanoseconds (*e.g.* ~4.5 ns for collagen). Second, it is preferred to fit all decay curves using same Laguerre function basis. The method of choosing a set of Laguerre functions with fixed orders and α for the fluorescence decays within a broad lifetime range are discussed in detail.

(a) Truncation length

Time-resolved fluorescence decays need to be truncated properly before the deconvolution. The truncation length should ensure that all fluorescence decays decay to zero. Endogenous fluorescence lifetime values are in the range of hundreds of picoseconds to several nanoseconds. Therefore, the truncation length was chosen about 50 ns in this study (200 data points at 3.6 GS/s sampling rate).

(b) Zero-delay baseline

Due to the chromatic dispersion and the timing jitter of the TRF subsystem, the signals at different wavelengths arrived at the PMT at different time. Therefore, a zero-time shift or delay is often observed between the fluorescence decay and laser response function. The mismatched baseline usually causes an inaccurate fitting result. To solve this problem, the decay curve and the fitting model are first aligned at the rising edge before the deconvolution calculation. Second, a number of potential delay values

were assumed and the Laguerre-based deconvolution is performed at each delay value. The delay value with the lowest normalized mean-squared error is taken as the optimal delay between the fitting model and the fluorescence decay.

(c) Upper boundary of α

The Laguerre scale parameter α determines the convergence speed and peak amplitude of Laguerre functions (Figure 5-2b). It can be chosen between 0 and 1 if the fluorescence decay is collected over an infinite time scale. Practically, the fluorescence decay signal only can be acquired in a finite data length. Marmarelis *et al.* [105] suggested that the α should be chosen to ensure that all LFs converge to zero over a limited sampling points to guarantee the orthonormality of the LFs. Based on this suggestion, the upper boundary of α (α_{upper}) was calculated for different orders of LFs and the number of data points as shown in Table 5-1. The α_{upper} decreases with the increase of the Laguerre orders or decrease in the number of the data points. An optimal α for a specific decay curve should be smaller than α_{upper}.

Table 5-1. Upper-boundary for α with different LF dimensions

LF orders	α_{upper}	
	200 points	160 points
4	0.9	0.896
8	0.842	0.802
12	0.776	0.728

(d) Look-up table for an optimal α value

Autofluorescence signals usually have a broad lifetime range between hundreds of picoseconds to several nanoseconds. The Laguerre scale parameter (α) needs to be chosen individually for each decay curve to obtain an accurate fitting result. Dabir *et al.*[109] provided an method that treated α as a variance in the fitting process and optimized it using a nonlinear regression for each fluorescence decay curve. The parameters α for the fluorescence decays in the lifetime range of 0.5-6 ns were investigated using this optimization method. The fitting results were highly correlated with the 'true' values and fall into the 95% confidence range as shown in Figure 5-3a. However, the optimized parameter α varies in a large range for different lifetime values (*e.g.* α=0.54 for 0.5 ns lifetime value, α=0.87 for 6 ns) (Figure 5-3b). In clinical studies, a single α is preferred to fit all fluorescence decays in order to investigate the variation of fluorescence component using the Laguerre expansion coefficients.

In order to choose a suitable Laguerre scale parameter α to fit fluorescence decay signals, a series of simulations was carried out. Fluorescence decay signals in the lifetime

range of 0.5-6 ns with 0.5 ns intervals were generated at different SNRs of 50, 100, and 200. Different Laguerre scale parameters α in the range of 0.6 to 1 were used to fit the simulated data. The acceptable α values for different lifetimes were calculated and summarized into a look-up table. This look-up table is then used to choose a suitable parameter α during clinical studies. Figure 5-4 gives an example of how to generate a look-up table of α when L is equal to 8. The estimated lifetime error was calculated as a function of lifetime values and α (Figure 5-4a). If the lifetime bias is smaller than 5% of the true value, then the corresponding α can be considered as an acceptable choice (Figure 5-4b). The relationship between α and lifetime values is also presented in two dimensional diagram (Figure 5-4c), in which the grey color presents the acceptable α ranges. For the fast decay signals, the upper boundary of α needs to be considered when choosing a suitable parameter, whereas the bottom boundary of α needs to considered for slow decays. Therefore, an α value is adequately chosen to minimize the lifetime error over all measured lifetimes, such as α=0.75 can achieve a minimum lifetime error in the lifetime range of 0.5-6 ns as the blue double arrows shown in Figure 5-4c. During the clinical study, the FWHM of each decay curve is first calculated, and then the expectation of FWHM over all decay signals is calculated to choose the corresponding α from the look-up table.

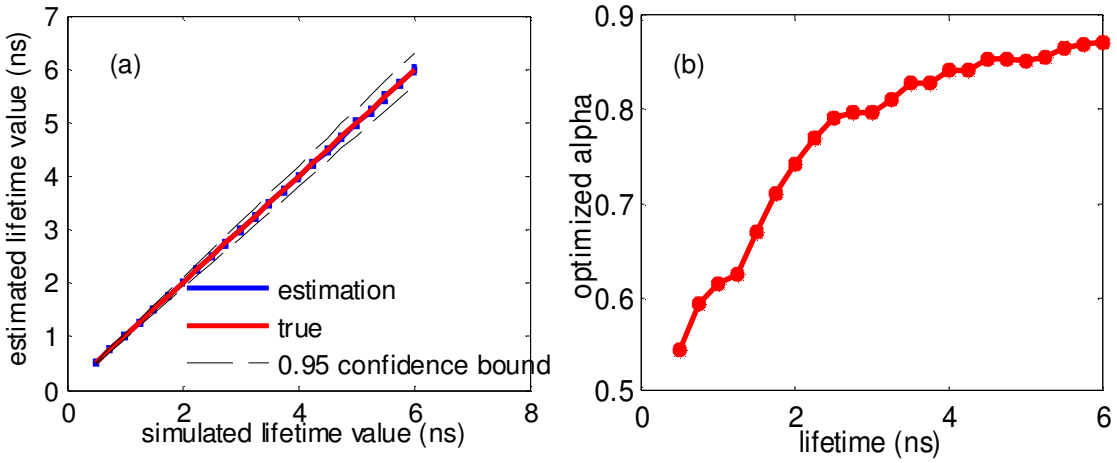

Figure 5-3. Estimation results for different lifetime values using the optimization alpha method with Laguerre orders (L) of 6. (a) The correlation between the estimation results and the simulated lifetime values. The estimated values fall into the 95% confidence interval of the 'true value'. (b) The optimized alpha for different lifetime values in the range of 0.5-6 ns. A small alpha is needed for decay with short lifetime values (*e.g.* α=0.51 for the lifetime of 0.5 ns, α=0.79 for the lifetime of 6 ns).

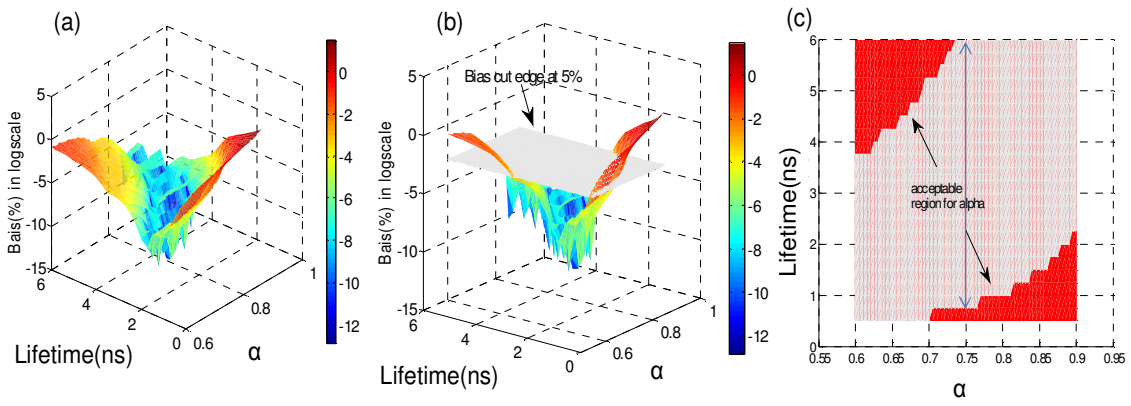

Figure 5-4. The α boundaries for different lifetime values (a) The lifetime error obtained from the simulation values. (b) The lifetime bias with 5% bias boundary. (c) Two-D diagram of (b) shows the upper and bottom boundaries of the α for different lifetime values.

5.3.3. Comparison of Laguerre basis with different orders

As we mentioned in the introduction, high-order LFs may provide an accurate estimation of the IRF because it is sensitive to the small changes of the decay curves. However, the OLF-based deconvolution method usually relied on the low-dimensional (orders ≤ 5) LFs to avoid an over-fitting problem in previous studies [92,109]. This problem can be solved using the CLF-based deconvolution method. In this section, the reliability of the high order Laguerre function basis in fitting fluorescence decays with a large lifetime range is investigated.

The IRFs were simulated by using a fast decay (lifetime τ_1=1 ns) and a slow decay (lifetime τ_1=5 ns) component. The fluorescence decays with different averaged lifetime values were generated by varying the contribution of these two components. The relative contributions of the slow and fast decay components changed gradually from 1:0 to 0:1 to obtain a linear variation of averaged lifetime from 1 ns to 5 ns. A hundred of decay curves were generated for each lifetime value. The CLF-based deconvolution with different parameter sets, including (L=4 and α=0.85), (L=8 and α=0.82), and (L=12 and α=0.78), were used to fit the simulated data. The reduced chi-squared (χ^2_{red}) was used to evaluate the goodness-of-fit [110]:

$$\chi^2_{red} = \frac{1}{(N-L)\sigma^2}\sum_{t=0}^{N-1}(y(t) - y'(t))^2 \qquad (5.25)$$

where N is the data length, L is the number of Laguerre functions, σ^2 is the variance of the observation; $y(t)$ is the simulation signal; and $y'(t)$ is the fitting result. A value of χ^2_{red} close to 1 indicates a good fitting result [110]. Applying the CLF-based

deconvolution method to the simulated decay curves, the goodness-of-fit results of different Laguerre functions basis were calculated (Figure 5-5a). We can see that the goodness-of-fit stays around 1 over the different lifetime values when using the Laguerre functions with higher orders (L=8 and 12), whereas the goodness-of-fit becomes larger for the Laguerre function with the orders of 4. The averaged lifetime values and fraction ratios predicted by different LFs basis are shown in Figures 5-5b and Figure 5-5c, respectively. We can see that, high Laguerre orders (L=8 and 12) provide a better estimation of the lifetime values and the fraction ratios than low Laguerre orders (L=4). These results indicate that the high-order LFs are more robust when fitting the decay curves yielding a large lifetime range using a constant Laguerre scale parameter α.

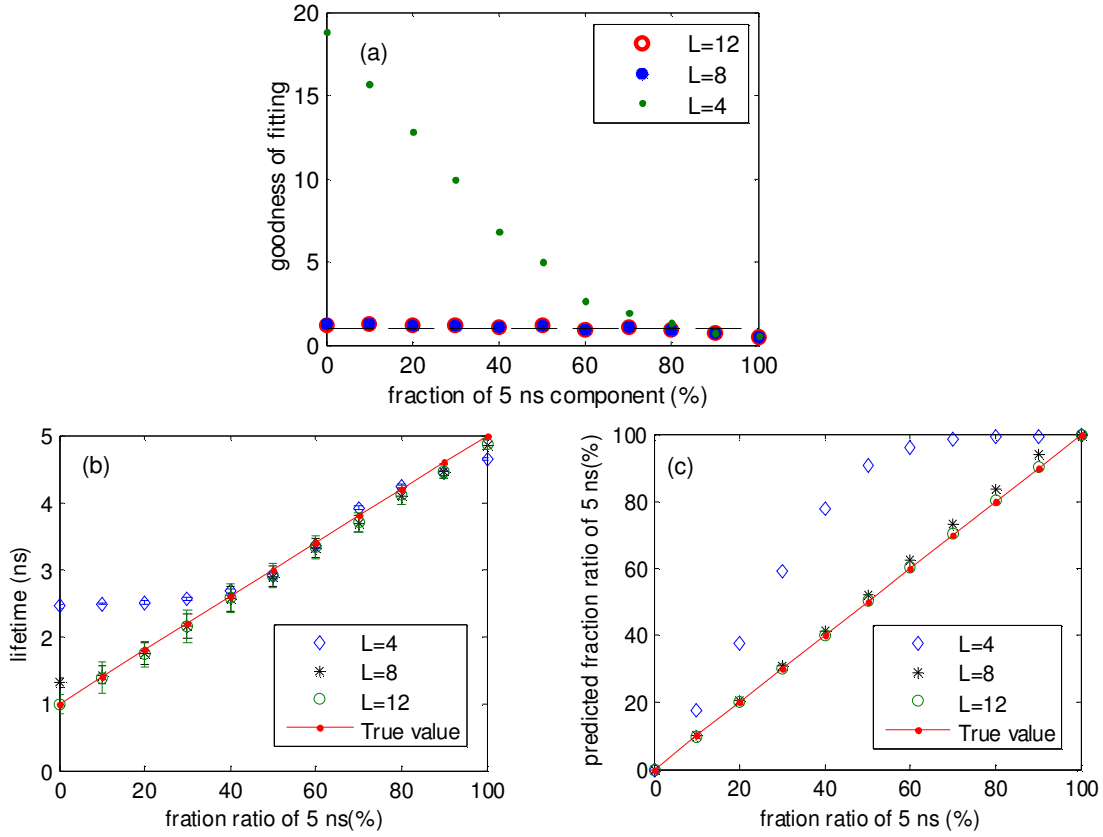

Figure 5-5. (a) Reduced chi-squared (χ^2_{red}) goodness-of-fit of CLF in different LFs sets (L=4, α=0.85), (L=8, α=0.82), and (L=12, α=0.78) for the simulated data with two lifetime components (1 ns and 5 ns) and different fractional contributions. (b) Prediction of averaged lifetime values by different LFs sets. (c) Predicted fraction ratios of 5 ns component.

5.3.4. Comparison of different deconvolution methods

The performance of the CLF-based deconvolution method was demonstrated using

the simulated fluorescence signals with the averaged lifetime of 1 ns at different SNRs (10, 20, 50, and 100). The OLF-based and single exponential based deconvolution methods were also carried out for the purpose of comparison. The parameters and deconvolution methods used in the comparison are listed in Table 5-2. Multi-exponential deconvolution has the most number of fitting parameters and uses nonlinear least squares regression. The CLF-based deconvolution method has the same fitting parameters as the OLF-based deconvolution, but is constrained by the decay profile.

Table 5-2. Summary of analysis methods examined in this comparison

Analysis Method	Output parameters	Optimization algorithm	Constraints
Multi-exponential deconvolution	$A_1 \ldots A_{n-1}$, $\tau_1 \ldots \tau_n$	Iterative nonlinear least squares	$0 < \tau_n < \infty$
Original Laguerre deconvolution	$C_0 \ldots\ldots\ldots C_{m-1}$	Linear regression (non-iterative)	None
Robust Laguerre deconvolution	$C_0 \ldots\ldots\ldots C_{m-1}$	Linear regression (iterative)	Decay profiles

LFs (L=12 and α=0.60) were used for both OLF- and CLF-based deconvolution methods. The fitting results are shown in Figure 5-6. Both OLF- and CLF-based deconvolution methods fit the decay curve signals accurately when the signals had high SNR. However, with the decrease of SNR, the oscillation phenomena appeared on the OLF-based fitting results, whereas the CLF-based fitting results were more robust as shown in Figure 5-6d. The lifetime bias and error of these three methods are shown in Figure 5-7. The bias and standard error obtained by the single exponential-based deconvolution method were 5 times lower than that of the Laguerre-based deconvolution methods. In addition, the CLF-based deconvolution method achieved smaller bias and standard error comparing to the OLF-based deconvolution method at low signal-to-noise.

To compare the performance of CLF- and OLF-based deconvolution methods in a large lifetime range, hundreds of decay curves were generated for different lifetime values (0.5 ns, 1 ns, 3 ns, and 5 ns) with SNR of 100. The OLF-, CLF- (L=12 and α=0.76) and single exponential-based deconvolution methods were applied to retrieve the fluorescence lifetime values. The residuals of the estimated lifetime values are shown in Figure 5-8. The results obtained from the single exponential-based and the CLF-based deconvolution methods were much closer to the true values than the results obtained from the OLF-based deconvolution method. Both the OLF- and CLF-based deconvolution methods had larger fitting errors when fitting the decays with lifetime smaller than 1 ns. The computation times of these three methods when fitting 407 fluorescence decays were 0.4 s, 0.9 s, and 10 s for OLF-based deconvolution, CLF-based deconvolution, and single

exponential based deconvolution respectively. This study demonstrates that the CLF-based deconvolution method is able to provide more accurate fitting results for different lifetime and SNR than the OLF-based deconvolution method.

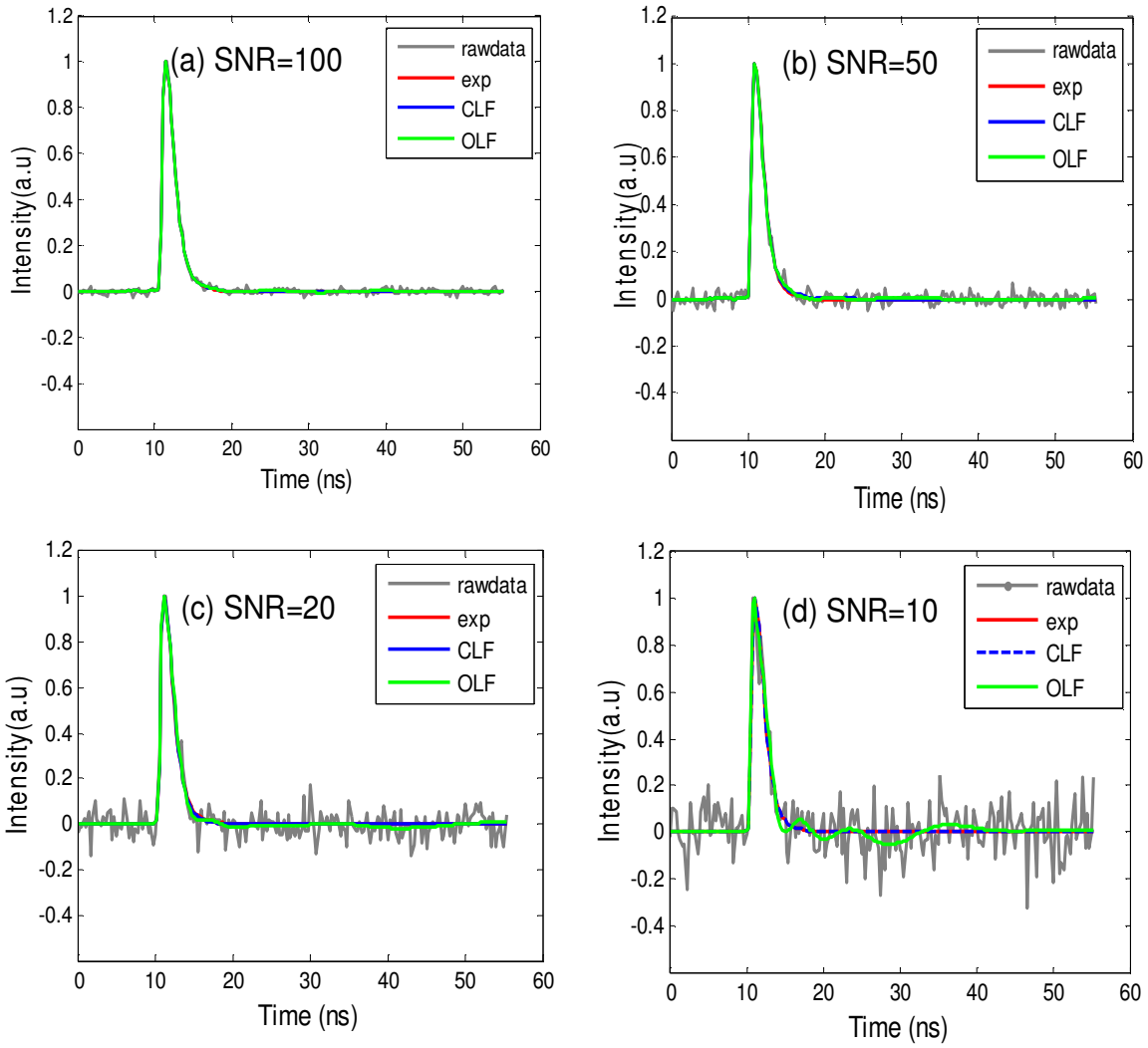

Figure 5-6. The fitting results of OLF- the CLF-based deconvolution (L=12 and α =0.60), and the single exponential deconvolution methods for the decay curve with lifetime of 1 ns at different SNR levels:(a) SNR=100, (b) SNR=50, (c) SNR=20, and (d) SNR=10. The fitting results of the OLF-based deconvolution method begin oscillating at low SNR as shown in (c) and (d), whereas the CLF-based deconvolution mehtod is more robust at different SNR levels and can achieve the same performance as the single exponential-based deconvolution method.

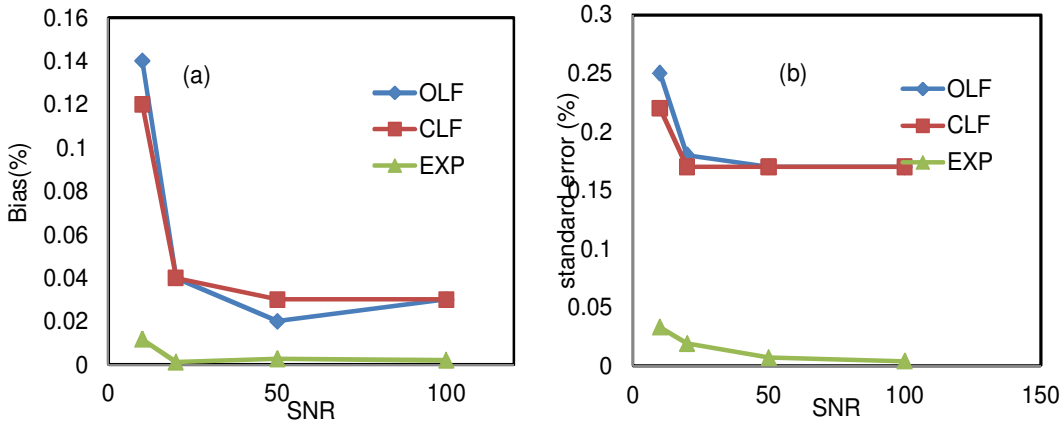

Figure 5-7. The bias (a) and standard error (b) of the estimated fluorescence lifetime using different deconvolution methods at different SNR levels (10, 20, 50, and 100). The CLF-based deconvolution method obtained lower bias and standard error compared to the OLF-based deconvolution in low SNR conditions.

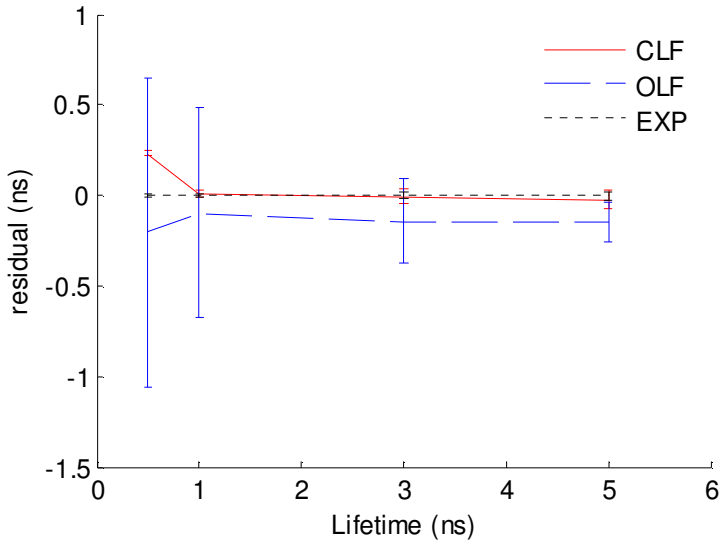

Figure 5-8. Comparison between the simulated lifetime values and the estimated lifetime values using different fitting methods including the single exponential, CLF-, and OLF-based deconvolution methods. The CLF-based deconvolution method provided the same performance as the single exponential based deconvolution methods except in the short lifetime of 0.5 ns.

5.4. Experimental validation

5.4.1. Experiment setup and sample preparation

(a) Instrument

The TRF subsystem was used to collect fluorescence decay signals as described in Section 3.2. A 355 nm pulse laser (pulse width: 300 ps (FWHM)) was used as the excitation light source. The fluorescence decays in the wavelength range of 370-550 nm were collected in sequence by using an AOTF-based spectrometer and a high sensitivity detector. Finally, the fluorescence decay signals were acquired by a high-speed digitizer and saved into a computer for further analysis.

(b) Fluorescence standards and biological molecules

The standard fluorescence dyes were selected to cover a wavelength range of 360-550 nm including fluorescein (emission peak: 515 nm and lifetime: 4 ns) and 9-cyanoanthracene (9-CA, emission peak: 445 nm and lifetime: 11.8 ns) dissolved in ethanol. Moreover, biomolecules were also used to validate the performance of the deconvolution method. These samples included NADH (emission peak: 450 nm and lifetime: 0.4 ns) and FAD (emission peak: 520 nm, lifetime: 2.7 ns) that were dissolved in PBS. The laser pulse energy was 2 μJ/pulse to avoid photobleaching.

(c) Data processing

A graphical user interface (GUI)-based software was developed in MATLAB for on-line data analysis during clinical studies. These raw data were first processed to obtain the expected data format and to eliminate the noise before deconvolution. The OLF-, CLF-based deconvolution methods, and multi-exponential-based deconvolution method were all implemented in the data analysis. The detailed flowcharts of this software are presented in Appendix III.

5.4.2. Validation Results

In order to check the robustness of the CLF-based deconvolution method on the fluorescence signals with broad lifetime values, both CLF- and OLF-based deconvolution methods were used to fit the measured signals. Figure 5-9 shows fluorescence fitting results of the standard fluorescence dyes and biomolecules at their emission peaks. The measured laser pulse and intrinsic response function are also presented. Five Laguerre expansion orders were used for CLF- and OLF-based deconvolution methods to retrieve the IRF. Different Laguerre scale parameters α were used for different decay signals (0.18, 0.65, 0.75, and 0.92 for NADH, FAD, Fluorescein and 9-CA, respectively). The CLF-based deconvolution method provided better fitting results compared to the OLF-based method when fitting the fast fluorescence decays such as NADH (Figure 5-9a) and FAD (Figure 5-9b). The IRFs obtained by the OLF-based method had a slight oscillation which did not occur when using CLF-based methods. Both methods provided

the same performance when fitting the slow decay curves such as Fluorescein (Figure 5-9c) and 9-CA (Figure 5-9d).

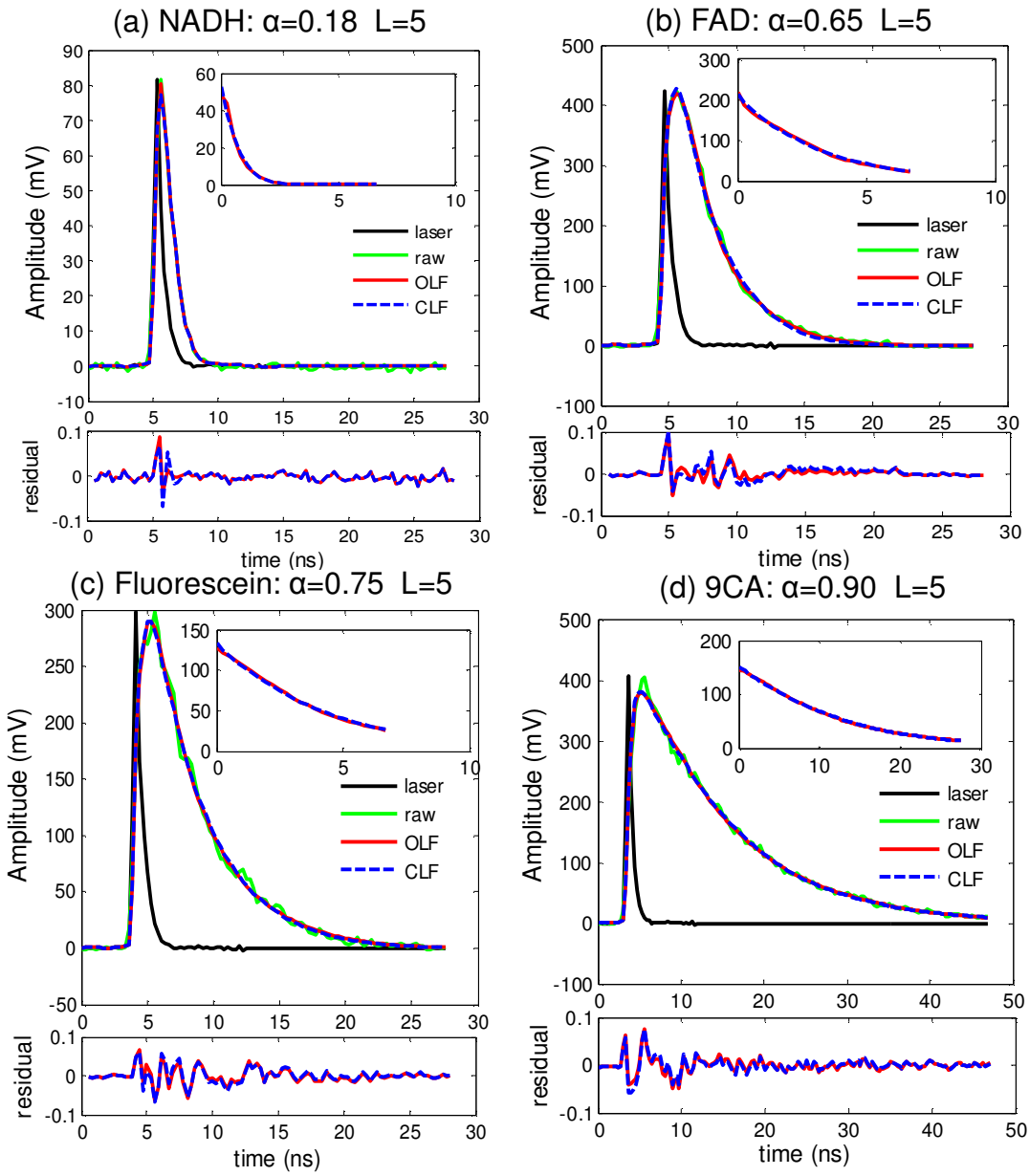

Figure 5-9. The OLF- and CLF-based deconvolution methods were used to retrieve the IRF for fluorescence standards and biomolecules ((a)-(d): NADH, FAD, fluorescein, and 9-CA). The IRFs are shown in the inset figures (x-axis: time (ns), y-axis: amplitude (mV)). The CLF-based deconvolution method improves the fitting results for the decay curves with short lifetime values such as NADH and FAD, and keeps the same performance as OLF-based method for the decay curves with long lifetime values such

as fluorescein and 9-CA.

In order to check the robustness of the CLF-based deconvolution method on the signals with low SNR, the OLF-, CLF-, and single exponential-based deconvolution methods were used to fit the fluorescence decay signals of the FAD over a broad spectral range. The steady-state spectrum is shown in Figure 5-10a, in which the intensities are very low in the short wavelength range of 370-420 nm. Figure 5-10b presents the lifetime values obtained by different deconvolution methods. We can see that the CLF-based deconvolution method can provide more reliable lifetime values than the OLF-based deconvolution method at short wavelengths. This method maintains the same performance with the single-exponential deconvolution method.

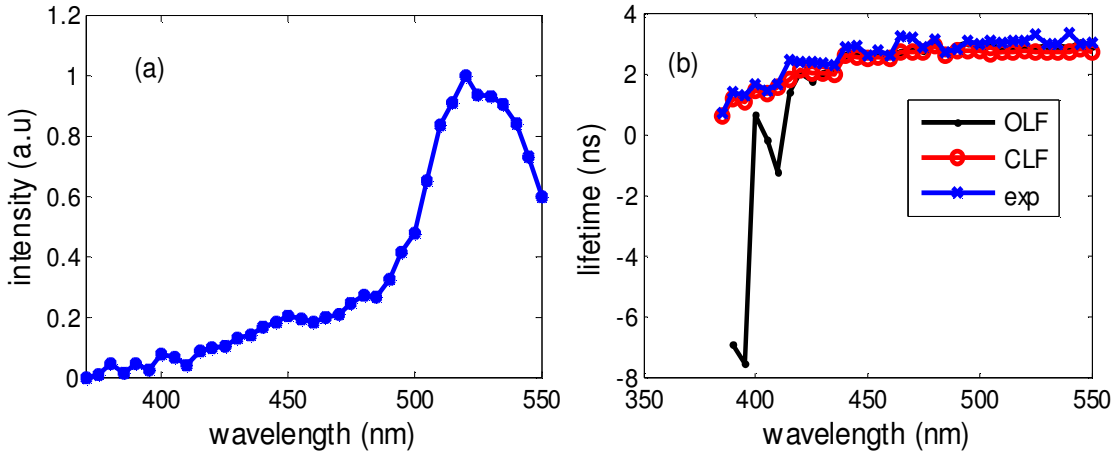

Figure 5-10. The OLF-, CLF- (a=0.75, L=5), and single exponential-based deconvolution methods performed on the fluorescence emission of FAD. (a) The steady-state spectrum of FAD has low SNR at short wavelengths (370-420 nm). (b) The lifetime values were obtained by three deconvolution methods over the observed spectral range. The CLF-based method is more robust than the OLF-based method at low SNR and maintains the same performance with the exponential deconvolution method.

5.5. Summary

In this chapter, a robust constraint Laguerre (CLF) -based deconvolution method was optimized by using the profiles of fluorescence decays to constrain the least squares fitting. This method solves the over-fitting and oscillation problems occurred in the OLF-based deconvolution method when fitting the decay signal with low SNR or using the high-order Laguerre functions. In order to optimize the fitting performance, different parameters, such as the total numbers of the Laguerre functions (L) and Laguerre scale parameter (α), were optimized for different fluorescence signals. A look-up table with

optimal Laguerre scale parameters α for different lifetime values was generated based on the simulated signals in the lifetime range of 0.5-6 ns (Figure 5-4). This look-up table can be used to choose a comprehensive scale parameter during clinical studies in real-time. In addition, simulated results also showed that the high-order Laguerre basis is much more robust than the low-order Laguerre basis in fitting the fluorescence decays with broad lifetime values (Figure 5-5). The performance of various deconvolution methods was validated on the standard fluorescence dyes and biomolecules. The results showed that the CLF-based deconvolution method had better fitting results than the OLF-based deconvolution method especially for decay curves with low SNR (Figure 5-10). In the next chapter, a pilot clinical study will be presented to investigate the relationship between the fluorescence and reflectance signals and the diagnostic results for brain tumour.

Chapter 6

A pilot *ex vivo* brain tumour study

This chapter presents a pilot *ex vivo* study of brain tumour using both time-resolved fluorescence spectroscopy and diffuse reflectance spectroscopy. This clinical study, including sample preparation and experiment procedures, are presented in Section 6.1. Fourteen patients were investigated in this study, while only the eight patients presented as meningiomas and high-grade gliomas were investigated. Section 6.2 presents the data analysis methods including data processing, feature selection, and classification, followed by the analysis results in Section 6.3. Several features including fluorescence intensity ratios, lifetime values, and Laguerre coefficient ratios at different wavelengths were selected using one-way ANOVA statistical analysis. The support vector machine (SVM) was used to classify the different tissue types. The results show that the meningiomas grade I can be distinguished from meningioma grade II with the sensitivity and specificity of both 100%.

6.1. Introduction

Gliomas and meningiomas are two primary brain tumour types. Surgery is the common treatment. However, it is a challenge to resect the tumour totally because of their tendency to infiltrate into the surrounding normal tissue making identification of tumour margins difficult. Fluorescence and diffuse reflectance spectroscopy have been studied for brain tumour margin detection in many clinical studies [6, 22], which demonstrated the potential of these techniques as intraoperative tools for neurosurgery. In order to study the fluorescence and diffuse reflectance properties of brain tumours, a pilot study on the *ex vivo* brain specimens was carried out using time-resolved fluorescence (TRF) and diffuse reflectance (DR) spectroscopy. The fluorescence and diffuse reflectance characteristics of various brain tumour types are investigated. Moreover, the fluorescence spectral and time-resolved features were used to discriminate the tumour types.

6.2. Methods and materials

6.2.1. Sample

Fourteen patients were involved in this study. The clinical protocol was approved by

the McMaster Research Ethics Board. Tumour specimens taken from the patients at surgery were transported immediately and were investigated within one hour after excision. During experimental measurements, the samples were kept in a petri dish and soaked using some drops of saline to keep moist. After measurements, the samples were stored in the buffered formalin for pathological examination.

6.2.2. Instruments

Autofluorescence and diffuse reflectance signals were measured by a TRF spectroscopy system [43] and a spatially resolved DR spectroscopy system, respectively. For the time-resolved fluorescence measurements, a 355 nm pulsed laser was used as the excitation light source. A bifurcated fused silica fibre optic probe was used to deliver the laser light and collect the fluorescence light as shown in Figure 6-1a. A single optical fibre with a 600 μm core diameter placed at the centre of the probe tips was used for the laser excitation, while twelve fibres with 200 μm core surrounding the single fibre were used to collect the fluorescence. The fluorescence light was passed through an acousto-optic-tunable-filter (AOTF) -based spectrometer and was then detected by a fast-gated MCP-PMT and finally digitized by an oscilloscope (DPO 7254, 40 GS/s sampling rate, 2.5GHz bandwidth, Tektronix) [43]. By switching the frequency of acoustic wave on the AOTF crystal, fluorescence signals can be collected in the spectral range of 370-550 nm with 5 nm intervals. For the diffuse reflectance measurements, a halogen lamp with the spectral range of 500-1000 nm was used as the light source. One single optical fibre was used for the light illumination, while six other fibres were used to detect DR signals at various source-detector distances (Figure 6-1b). All optical fibres used in the DR measurement have the core diameter of 200 μm and NA of 0.22. The DR spectra were diffracted by a spectrograph, and then captured by a cooled CCD-based camera. An optical attenuator was used to adjust the DR intensity for each detection channel to obtain sufficient SNR. A portion of light (20%) from the light source was used as a reference light to normalize the DR spectra.

6.2.3. Experimental procedure

The tissue samples were placed in a non-fluorescent petri dish as Figure 6-1c shows. Two probes were held by a translation stage that was used to adjust the distance between the probes and the sample. The DR fibre probe was in contact with the surface of the sample perpendicularly, while the TRF fibre probe was placed at 0.5 cm above the surface of the sample with a 45 degree in order to decrease the distortion of the laser back-scattering light (Figure 6-1c). Time-resolved fluorescence and diffuse reflectance signals were measured in sequence. In order to avoid the thermal damage of biological tissue and the photobleaching of endogenous fluorophores, the laser output energy at the

fibre tips was measured by a power meter (3-sigma, Coherent, Santa Clara, CA) and adjust to 3 μJ/pulse. The fluence of each laser pulse was 1.24 μJ/mm^2 on an area of 2 mm^2 on the surface of sample. Autofluorescence signals were collected at 37 wavelengths from 370 nm to 550 nm with 5 nm intervals. An average of 10 pulses was used at each wavelength to improve the signal-to-noise ratio. The TRF data acquisition time was 4 s for a single-point measurement. The room light was turned off to decrease background during the DR spectra measurement. Ten measurements were also averaged to improve the signal-to-noise ratio for DR spectra. The background noise was also measured with same setting after the collection of DR spectra. The investigated location were marked using the biological ink after the experiment. The samples were fixed in the buffered formalin for further histopathological analysis.

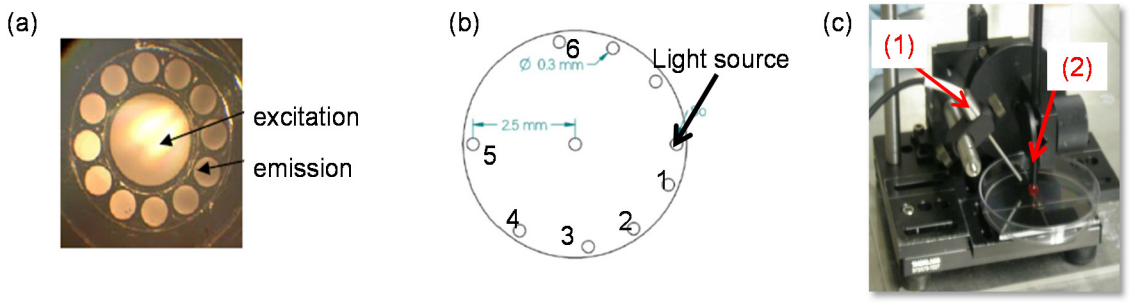

Figure 6-1. Fibre optical probe tips and the measurement setup in the *ex vivo* brain tumour study. (a) Fibre arrangement at the bifurcated fibre tips for the TRF spectroscopy. (b) Fibre arrangement at DR probe tips. (c) The setup of the experiment, in which the fibre optic probes for TRF (1) and DR (2) spectroscopy held by a translation stage.

6.2.4. Diagnostic results

Various tumour types, including gliomas, meningiomas, and metastatic tumour etc., were investigated using the TRF and DR techniques. Only the samples from eight patients diagnosed as meningiomas and high-grade gliomas were analyzed in this study. Specifically, high-grade gliomas (HGG), including glioblastoma multiform (TRF examination numbers N=5), glioblastoma post therapy (N=10), recurrent anaplastic oligodendroglioma (N=5), and anaplastic oligodendroglioma (N=2), were investigated to characterize their fluorescence and diffuse reflectance properties. Meningiomas, including grade I (N=9) and grade II atypical meningioma (N=7), were studied as well. Table 6-1 shows the detailed diagnostic results and data numbers for TRF and DR measurements.

Table 6-1. Diagnostic results

Tumour type	Pathological results	Patients	TRF	DRS
Meningiomas	grade-I	P10, P09	9	0
	grade-II	P06	7	4
HGG	anaplastic oligodendroglioma	P02	2	1
	recurrent anaplastic oligodendroglioma	P08	5	0
	glioblastoma	P12, P13	5	4
	glioblastoma post therapy	P07	10	4

6.3. Data analysis

The measured signals were analyzed after clinical study. The fluorescence spectral and lifetime were calculated using the robust Laguerre-based deconvolution method as explained in Chapter 5. Afterwards, the statistic and classification method were applied to investigate the feasibility of differentiating the different tissue types using spectroscopic features.

6.3.1. Data preprocessing

For the fluorescence measurement, the SNR of fluorescence decays at the emission peak was in the range of 4 dBm to 20 dBm with an average of 10 dBm. For the TRF measurement, the intrinsic response function (IRF) of the fluorescence was extracted from the measured fluorescence decay using the robust Laguerre function-based deconvolution method. A Laguerre functions basis (L=5 and α=0.967) was used to fit the measured fluorescence decays. Three parameters at each wavelength, including integrated intensity (I_λ), fluorescence average lifetime ($\tau_{avg\lambda}$), and normalized Laguerre expansion coefficients ($LECs_\lambda$), were calculated to characterize the fluorescence properties of each tissue type. The integrated intensity can be calculated by averaging the IRF over the observed time scale. To eliminate intensity variation that was introduced by the measurement geometry of fibre probe, the intensity spectrum was normalized at its emission peak wavelength. The average lifetime (τ_{avg}) was calculated as:

$$\tau_{avg} = \frac{T.\sum_{n=0}^{N} n.h(n)}{\sum_{n=0}^{N} h(n)}, \quad (6.1)$$

where $h(n)$ is the IRF, N is the number of measured data points, and T is the sampling time intervals which are 25 ps in this study. In addition, normalized Laguerre expansion coefficients (LECs) can also be used to estimate the fluorescence components ratio as

discussed in Section 5.2.

In the context of DR spectroscopy measurement, the background noises were first subtracted from the measured DR spectra. Afterwards, the DR spectra were normalized by the reference spectrum to obtain the corrected diffuse reflectance spectra. The optical properties, including scattering and absorption coefficients, can be retrieved from the diffuse reflectance spectra. In this study, only the spectra at selected source-detector distances were presented to characterize the properties of the brain tumours without extracting the optical properties from the measured spectra.

6.3.2. Features selection

Due to lack of diffuse reflectance measurements of certain tumour types, only the fluorescence features were used to differentiate the tumour types. In order to find significant features that provide better discrimination performance, the univariate analysis of variance (one-way ANOVA) was used to evaluate the fluorescence characteristics (I_λ, τ_λ, LEC-0_λ, LEC-1_λ, LEC-2_λ, and LEC-3_λ) at each wavelength λ for different tissue types as defined by the diagnostic results. The statistically significant features were selected if the p-value <0.05 from the ANOVA analysis. All statistical analysis was conducted using MATLAB.

6.3.3. Classification

Linear support vector machine (SVM) is used to classify two different groups in this study. SVM was a supervised classification method. The training data groups are first supervised to obtain a classification model. This classification model is further used to classify measured data into different types. In this training step, a hyperplane is optimized to separate training data into two classes based on some samples of training data. These samples are known as support vector. As Figure 6-2 shows, a hyperplane, which can be presented as $\langle w, x\rangle + b = 0$, is used to classify the training data, where x is the training sample, the vector w determines a direction perpendicular to the hyperplane, while varying the value of b moves the hyperplane parallel to itself [113]. The w and b are called the weight vector and bias, respectively. The optimized hyperplane is obtained by choosing a suitable w and b to maximize the margin between the observed support vectors. As shown in Figure 6-2, the grey hyperplane can also be used to correctly classify the training data into to two groups. However, the margins from the samples to the hyperplane are not maximum distance. Thus, a new set of w and b are needed to maximize the margin between two groups as the bold black line shows.

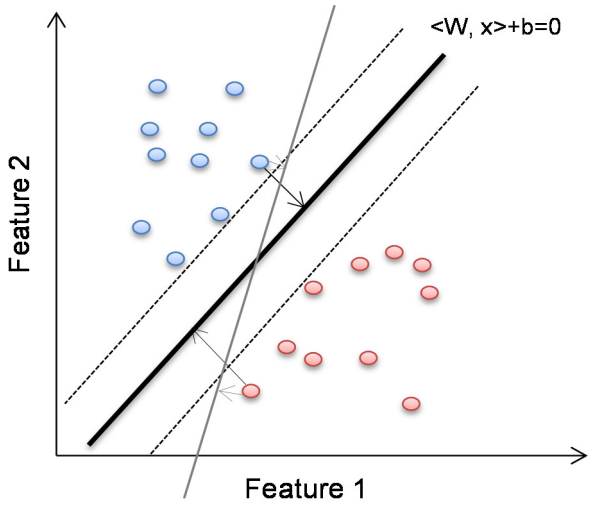

Figure 6-2. Diagram of Linear SVM

In order to estimate the performance of classification, the leave-one-out cross validation method was used to calculate the error between the classification results and the predict groups based on the diagnosis results. In this method, a sample was excluded from the database to be used as test sample and the rest of the data was used as training sample. This method avoids drastic reduction in sample size within both training group and test group, thus making it suitable for the classification with limited sample numbers. Finally, the sensitivity and specificity were calculated for each tissue type to evaluate the classification performance. All classifications were implemented using MATLAB.

$$\text{Sensitivity} = \frac{\text{true positives}}{\text{true postives+false negatives}} \tag{6.2}$$

$$\text{Specificity} = \frac{\text{true negatives}}{\text{true negaives+false postivies}} \tag{6.3}$$

6.4. Results

6.4.1. Autofluorescence characteristics of different tissue types

The averaged fluorescence spectra, lifetime, and LECs parameters for the meningiomas and HGG are presented in Figure 6-3. Both meningiomas and HGG have broad emission spectra with the emission peaks at 450 nm. The meningiomas have higher intensity at 390 nm compared to the HGG due to the high concentration of collagen. The attenuations of the intensity of meningiomas and HGG at 415 nm are caused by the absorption of hemoglobin from the biological tissue and blood. The meningiomas and

HGG have significant differences in their time-resolved fluorescence characteristics. The lifetime of meningiomas varies across the observed spectrum. The lifetime is around 3.5 ± 0.2 ns at 390 nm but decreases slightly to 3.4 ± 0.1 ns at 410 nm, and then increases slowly to 3.7± 0.2 ns at 540 nm. The lifetime values at short wavelength and longer wavelength are contributed by collagen and lipid respectively. On the contrary, lifetime values of HGG decreases slightly across the observed spectrum with an average lifetime of 3 ns. The LECs of meningiomas differ from that of HGG; this indicates the difference of the decay components for meningioma and HGG. For example, the zero order of Laguerre expansion coefficient (LEC-0) of the meningiomas is higher than that of HGG, which indicates more slow decay components in the meningiomas. In order to investigate the detailed autofluorescence characteristics of different tumour types, the subtypes of meningiomas and the subtypes of HGG are also presented in the following discussion.

(a) Meningiomas

The fluorescence characteristics of grade I and grade II meningiomas are shown in Figure 6-4. The grade I meningioma has high intensity at 400 nm but low intensity after 450 nm compared to the grade II meningioma. The lifetime of grade I meningioma is 3.8 ± 0.1 ns at 380 nm. It decreases with the increase of wavelength, and then keeps constant around 3.3 ± 0.1 ns after 500 nm. On the other hand, the lifetime of grade II meningioma decreases from 3.8 ± 0.1 ns at 385 nm to 3.3 ± 0.1 ns at 405 nm, and then increases rapidly to 4.4 ± 0.1 ns at 525 nm, which is mainly contributed by the lipid in the meningioma tissue. This feature indicates that the grade II meningioma has higher lipid concentration compared to grade I meningioma. In addition, LEC-0 of the grade I meningioma is higher than that of grade II meningioma in the short wavelength range of 370-450 nm, but keep similar at longer wavelengths. LEC-1s of these two tumour types are slightly different at short wavelengths, but increase with same trend after 450 nm. These characteristics can be used to differentiate the grade I and grade II meningiomas.

(b) High-grade gliomas

Different types of HGG, including glioblastoma multiform (GBM), GBM post therapy, anaplastic oligodendroglioma (AOD), and recurrent AOD, were investigated to reveal the fluorescence characteristics of malignant glioma tumours (Figure 6-5). All types of HGG have the similar spectra and lifetime trends across the observed spectral range, except for the GBM that has lower lifetime values than the other three types. The AOD and the recurrent AOD have similar spectra and lifetime features. The GBM has lower lifetime value compared with the GBM post therapy specimens. The GBM has slightly lower lifetime at 450 nm compared to the AOD. The Laguerre expansion coefficients of the AOD and GBM vary with the same trends except for the LEC-1 of

GBM which is lower than that of the AOD in longer wavelength. This indicates that the GBM has more fast-decay components than the AOD because of the changes in the concentration of FAD.

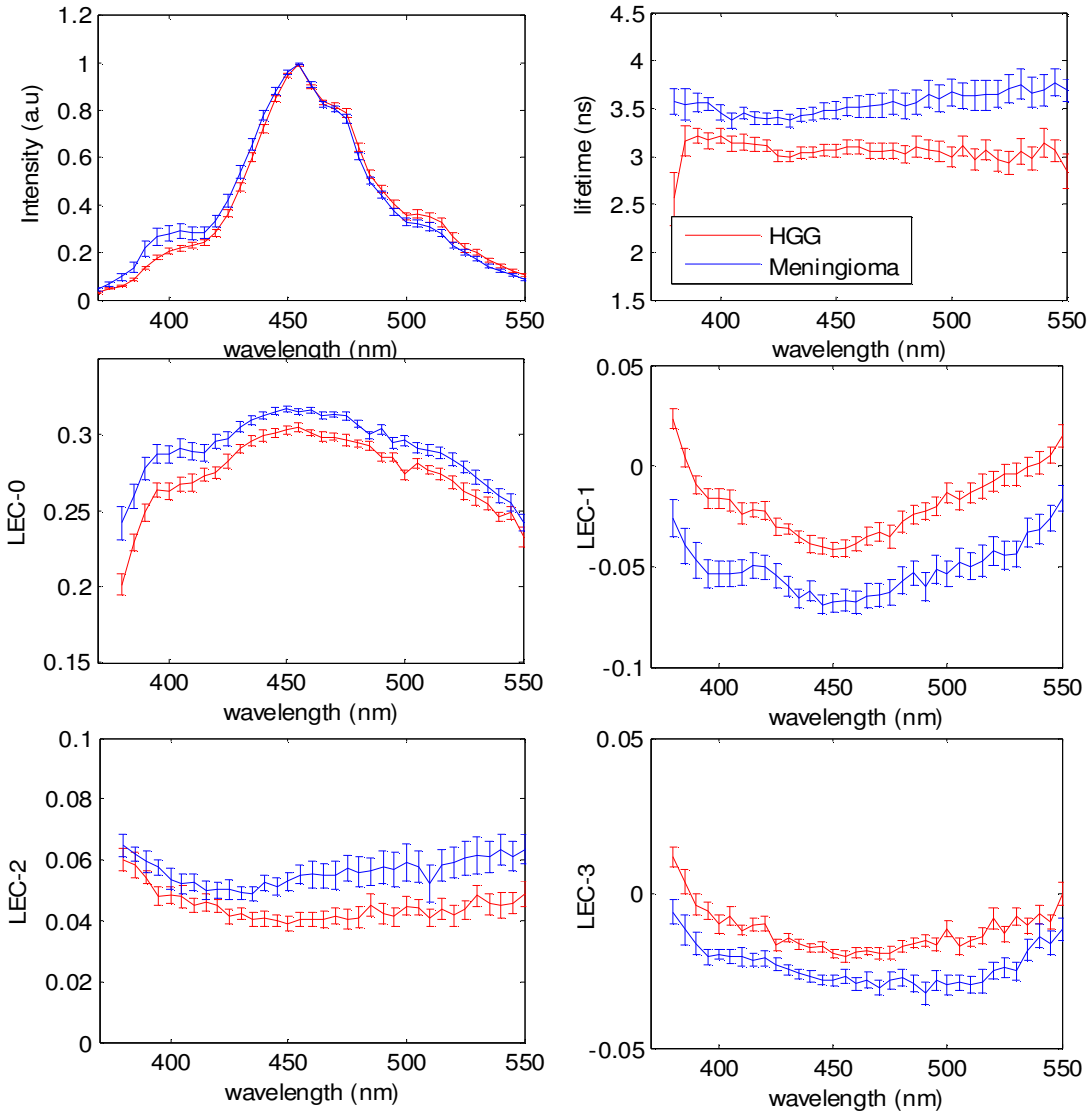

Figure 6-3. Autofluorescence characteristics of the HGG and meningiomas: (a) normalized spectrum, (b) average lifetime, and (c)-(f)Normalized Laguerre expansion coefficients (from (c) to (f): LEC-0, LEC-1, LEC-2, and LEC-3). (mean ± standard error).

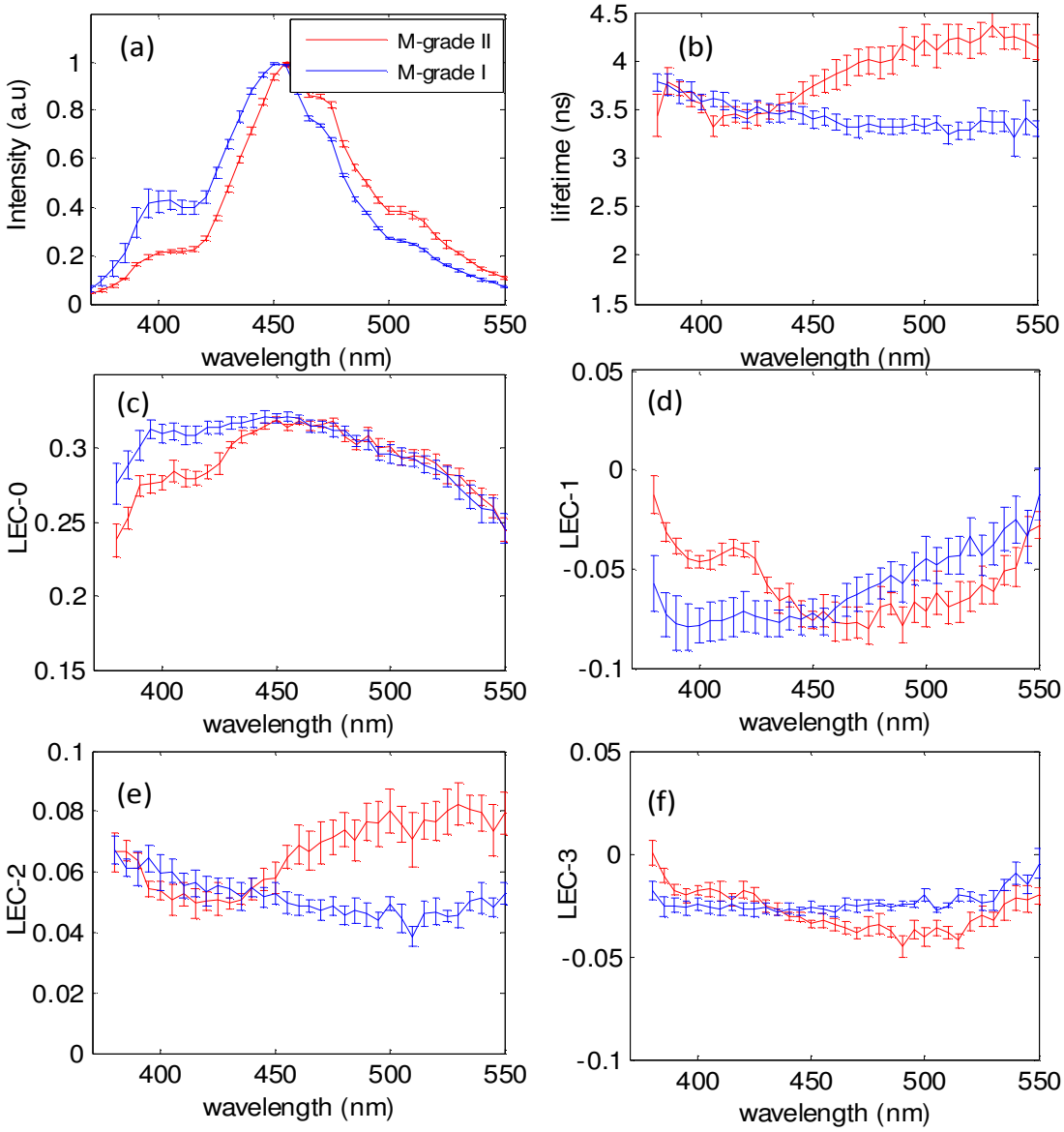

Figure 6-4. Autofluorescence characteristics of the meningioma subgroups: (a) steady-state spectra, (b) average lifetime, (c)-(f) normalized Laguerre expansion coefficients (from (c) to (f): LEC-0, LEC-1, LEC-2, and LEC-3).

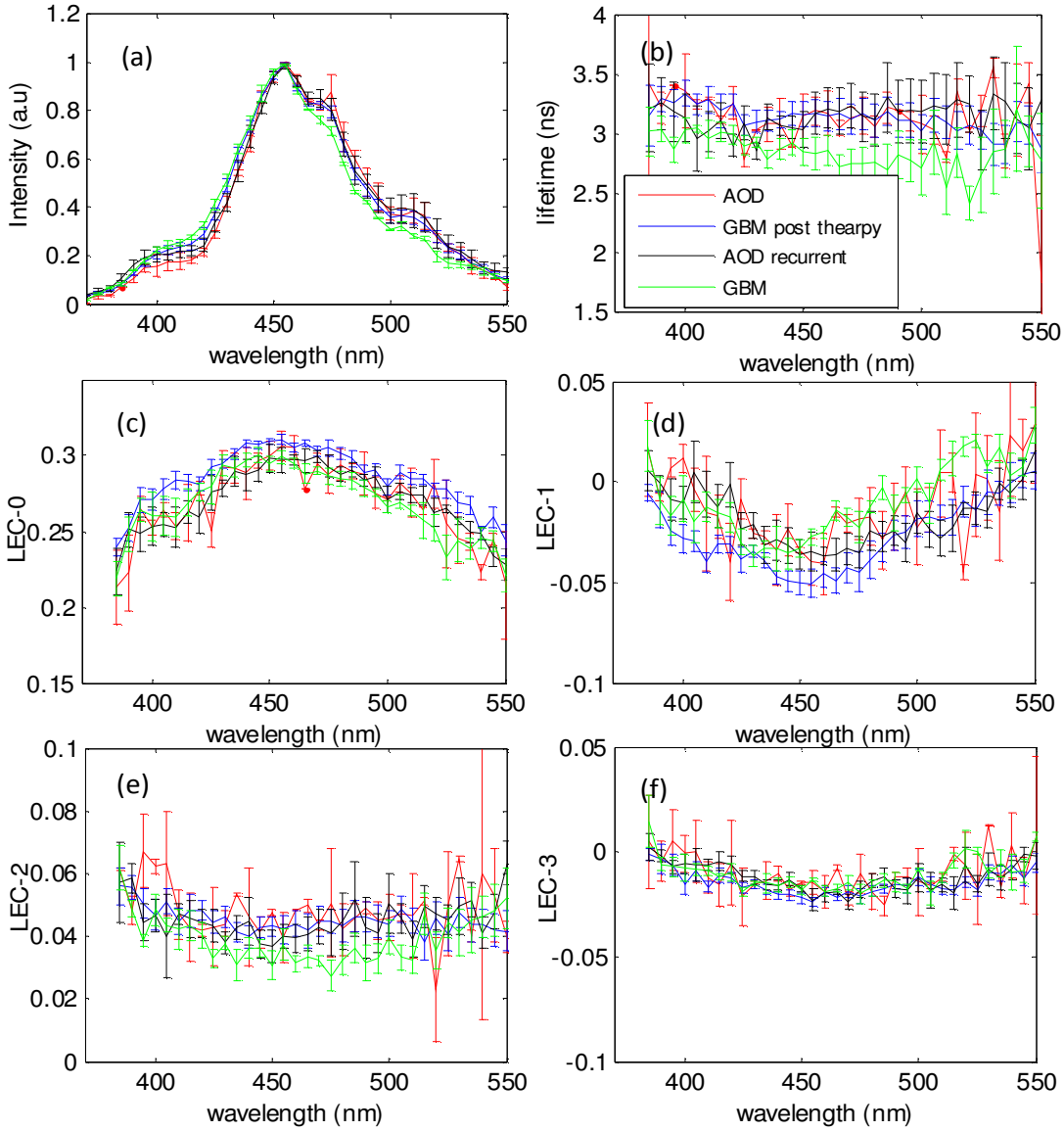

Figure 6-5. Autofluorescence characteristics of the HGG subgroups : (a) steady-state spectra, (b) average lifetime, and (c)-(f) normalized Laguerre expansion coefficients (from (c) to (f): LEC-0, LEC-1, LEC-2, and LEC-3).

6.4.2. Diffuse reflectance characteristics of different tissue types

The spatially resolved diffuse reflectance spectra were measured at the same location as the fluorescence measurement. The diffuse reflectance spectra at different source-detector distances for the meningiomas and HGG are shown in Figure 6-6 (a) and Figure 6-6(b) respectively. The diffuse reflectance spectral intensities decrease over the source-detection distance. Theoretically, optical properties can be retrieved from the

spatially resolved diffuse reflectance spectra [64]. However, due to the low signal-to-noise ratio and high blood absorption of the sample, optical properties could not be retrieved correctly. Figure 6-7 shows the normalized diffuse reflectance spectra at the source-detector distance of 1 mm for the meningiomas and HGG. The spectral intensities decrease between 520 nm and 580 nm representing the blood absorption. The meningiomas have slightly higher scattering light than that of HGG in the wavelength range of 700-800 nm. These features can be used to differentiate the tumour types. However, the diffuse reflectance spectra are only collected for several samples, it is insufficient to classify the tissue types. Hence, only the fluorescence features are used in the classification of different tissue types in the following section.

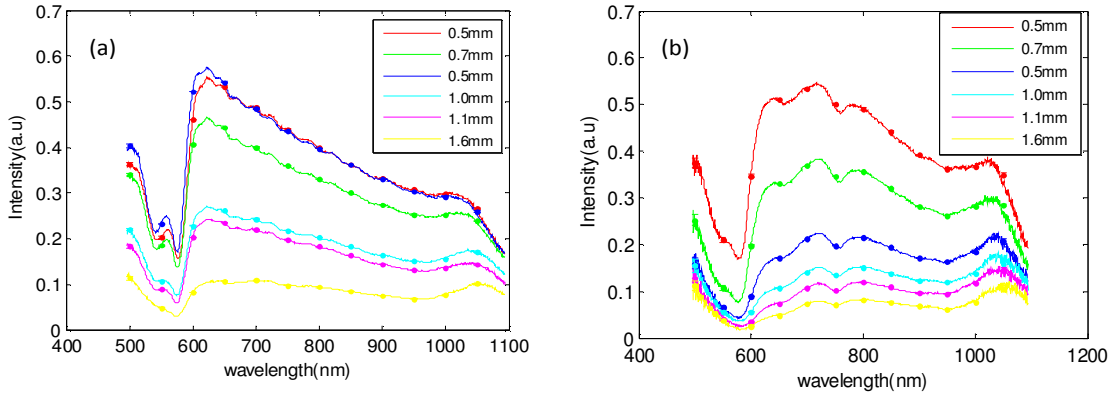

Figure 6-6. The spatially resolved diffuse reflectance spectra for different tumour types. (a) The DR spectra for the grade II meningioma samples. (b) The DR spectra for the high-grade glioma (anaplastic oligodendroglioma) samples.

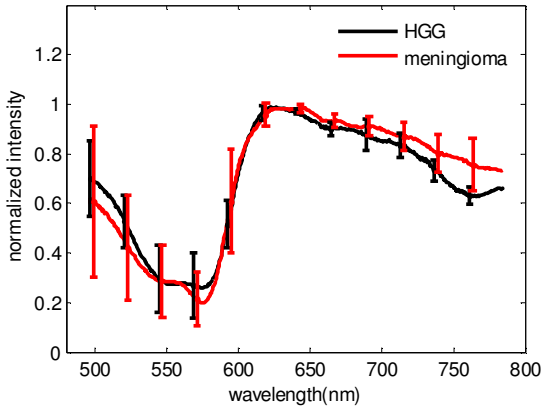

Figure 6-7. Normalized diffuse reflectance spectra of HGG and meningiomas at the source–detector distance of 1 mm. The HGG and meningiomas have different intensity in the wavelength range of 700-800

nm. (mean ± standard error).

6.4.3. Significant features

The significant spectral features (I_λ) and time-resolved features (τ_λ, LEC_λ) were chosen using the one-way ANOVA test if a p-value < 0.05 is obtained. This step is used to minimize the data size and find the significant features between different tumour types. The results indicated that the spectral parameters provide significant differences for the meningiomas and HGG such as the intensity ratio at different wavelengths of 400 nm, 460 nm, and 530 nm. For example, the intensity ratio of the spectral band of 390-410 nm and 520-540 nm for meningioma grade I is twice higher than that of meningioma grade II. Average lifetime as well as the Laguerre expansion coefficients at 400 nm, 460 nm, 480 nm, and 500 nm are also used to discriminate the different tumour types. Therefore, three intensity ratios, four lifetime values and two Laguerre coefficients ratios are chosen for further classification (Table 6-2). These features correlate with the changes of endogenous fluorophores in different tissue types. For example, the intensity ratio $I_{450\text{-}470}/I_{520\text{-}540}$ indicates the variation of NADH and FAD, which are highly related to the metabolic status of biological tissue [52]. Moreover, the ratio of Laguerre coefficients in different orders such as LEC0/ LEC2 at 400 nm indicates the changes of the fast and slow decay components in the IRF.

Table 6-2. Representative set of spectroscopic parameters that allows for tissue type discrimination.

Features	Meningioma grade I	Meningioma grade II	AOD	GBM
$I_{(390\text{-}410)}/I_{(520\text{-}540)}$ (a.u)	2.28 ± 0.035	0.97 ± 0.05	1.01 ± 0.21	1.14 ± 0.77
$I_{(390\text{-}410)}/I_{(450\text{-}470)}$ (a.u)	0.44 ± 0.07	0.25 ± 0.01	0.23 ± 0.03	0.27 ± 0.02
$I_{(450\text{-}470)}/I_{(520\text{-}540)}$ (a.u)	5.19 ± 0.07	3.93 ± 0.13	4.17 ± 0.41	4.24 ± 0.19
τ_{400} (ns)	3.38 ± 0.11	3.55 ± 0.09	3.19 ± 0.16	3.23 ± 0.08
τ_{460} (ns)	3.25 ± 0.08	3.86 ± 0.15	3.19 ± 0.12	3.04 ± 0.10
τ_{480} (ns)	3.17 ± 0.10	3.97 ± 0.16	3.09 ± 0.15	2.99 ± 0.11
τ_{530} (ns)	3.27 ± 0.10	4.36 ± 0.11	3.39 ± 0.22	2.88 ± 0.16
$LEC0/LEC2_{(400)}$ (a.u)	5.97 ± 0.60	5.26 ± 0.41	5.26 ± 0.59	6.41 ± 0.76
$LEC0/LEC2_{(530)}$ (a.u)	5.42 ± 0.61	3.45 ± 0.23	7.29 ± 1.8	6.12 ± 0.56

6.4.4. Classification results

The classification models are designed to separate the meningiomas and HGG as well as their subgroups. Three classification sets were studied including: (1) the meningiomas and HGG; (2) the grade I and grade II meningiomas; (3) the AOD and GBM. The performance of the classification using different features was assessed by the

classification error, which is the ratio of the misclassification sample numbers and the total sample numbers. The features that can provide the minimum classification error were chosen as the optimal feature set.

By using all of the spectral- and time-resolved features mentioned in Table 6-2 into the SVM classification model, the HGG can be discriminated from the meningiomas with a high sensitivity but a low specificity of 91% and 45%, respectively (Figure 6-8a). The grade I meningiomas can be discriminated from the grade II meningiomas using the intensity ratio features ($I_{390-410}/I_{520-540}$) and lifetime features (τ_{400}) with both sensitivity and specificity of 100% (Figure 6-8b). In the classification set of HGG subgroup, the AOD and GBM have very similar fluorescence spectra and lifetime values. The AOD can be discriminated from GBM with a sensitivity of 82% but with a specificity of only 20%. In addition, we observe that the spectra and lifetime features of the grade II meningiomas are very similar to that of the normal dura tissue as presented in Ref [55]. Due to lack of the histopathological results, the signals of grade II of meningiomas may be measured from the normal tissue that is adjacent to the grade II meningiomas. Therefore, the detailed histopathological results are necessary to confirm this hypothesis. Based on this hypothesis, the classification of meningiomas and HGG was investigated again using only the grade I meningioma. The classification results demonstrates that the grade I meningioma can be differentiated from the HGG with a sensitivity of 100% and a specificity of 95%. Table 6-3 summarizes the sensitivity and specificity of different classification sets. We can see that the meningiomas (especially grade I) can be discriminated with very high sensitivity and specificity.

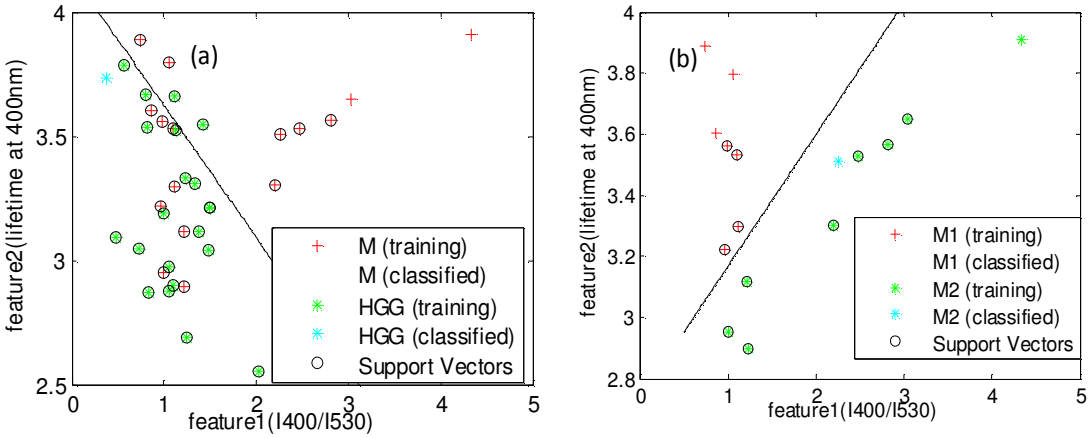

Figure 6-8. SVM supervised classification results of HGG and meningioma using the intensity and lifetime features. (a) SVM classification results for HGG (red cross) and Meningioma (green circle). (b) SVM classification results of grade I and grade II meningiomas.

Table 6-3. SVM classification results for different groups

Tissue types	Features	Sensitivity	Specificity
Meningioma and HGG	ALL features	91%	45%
Meningioma grade I and grade II	Spectra/lifetime	100%	100%
AOD and GBM	Spectra/lifetime	82%	20%
Meningioma grade I and HGG	Spectra/lifetime	100%	95%

6.5. Discussion

The autofluorescence and diffuse reflectance characteristics of different brain tumour types were investigated in this pilot study. The fluorescence characteristics, including the normalized intensity, the average lifetime, and the normalized Laguerre coefficients, were presented. The main endogenous fluorophores contributed to the fluorescence emission of meningiomas include collagen, NADH, FAD, and lipid, while the main endogenous fluorophores in the HGG include NADH and FAD. This leads to different spectra and lifetime values between the HGG and meningiomas. The fluorescence of extracellular proteins, in particular collagens, is most likely to dominate the fluorescence emission at 390 nm with lifetime of 3-3.5 ns in meningiomas. This is in good agreement with the lifetime of collagen measured in other studies [55]. Short lifetime values at the emission peak in 460 nm were found in both the HGG and meningiomas, which are contributed by NADH [41].

The grade I meningioma has significant differences from grade II meningioma in the fluorescence features. The spectral intensities of grade I meningioma in the short wavelength range of 390-400 nm are much higher than that of grade II meningioma. In terms of time-resolved features, the lifetime value of grade II meningioma increases at longer wavelengths and reaches 4.36 nm at 540 nm, whereas the lifetime value of grade I meningioma decreases from 3.5 ns to 3 ns over the observed spectral region. By using these features, the grade I meningioma can be separated from grade II meningiomas with both the sensitivity and specificity of 100%. In addition, two kinds of HGG including glioblastoma multiforme and anaplastic oligodendroglioma were investigated. Glioblastomas originate from astrocytes and lead to 80% of the malignant brain tumour. Oligodendroglioma is another type of glioma originating from the oligodendrocytes. Both tumour types have very similar spectral and time-resolved fluorescence characteristics as Figure 6-5 shows. The sensitivity and specificity of glioblastomas differentiated from anaplastic oligodendroglioma are only 82% and 20% respectively when using SVM classification method.

Since only a few specimens were investigated in this study, it is not sufficient to

provide robust classification results. Therefore, these classification results need to be carefully interpreted. A large population of clinical studies are needed to verify these fluorescence characteristics in future studies. Even though this *ex vivo* study demonstrates the potential of TRF and DR spectroscopy to distinguish the tumour types, it should be noted that the results might not exactly correlate with the active brain tumour status. The biological properties such as the blood volume, enzyme activities related to metabolic status may be different for *ex vivo* and *in vivo* samples, thus causing the difference of fluorescence signals for *ex vivo* and *in vivo* conditions as demonstrated by Chung *et al.* [112] and Butte *et al.*[6,56]. Therefore, our future works will focus on *in vivo* clinical studies using the integrated TRF-DR spectroscopy system to investigate the properties of tumour and normal tissue.

Chapter 7

Hyperspectral fluorescence lifetime imaging for optical biopsy

In this chapter, a scanning-based spectrally and temporally resolved hyperspectral fluorescence lifetime imaging setup is developed for optical biopsy studies. The intensity and lifetime images in the spectral range of 370-550 nm can be obtained to provide hyperspectral intensity and lifetime features of biological tissue. An introduction of optical biopsy applications of fluorescence lifetime imaging is presented in Section 7.1. It is followed by the system configuration and tissue phantom preparation in Section 7.2. The performance of the system was characterized and validated using standard fluorescence phantoms and biological tissue and is presented in Section 7.3. The results illustrated that this system is capable of resolving the fluorescence signals spectrally and temporally from different fluorescence dyes and autofluorescence from biological tissue.

7.1. Introduction

Chapter 3 presented a single-point spectroscopy system for optical biopsy to reveal the changes of biochemical composition and structures of biological tissue. However, the single-point spectroscopy only measured the fluorescence signal from a small tissue volume at a time, which limits its sampling numbers and its ability to identify the location of the tumour directly. Two-dimension (2-D) imaging is preferred in tumour diagnosis because it can provide the biochemical and structural features of biological tissue in a large region of interest, which allow it to show the tumour margin directly [114].

Fluorescence lifetime imaging microscopy (FLIM) has been used in many clinical studies such as glioblastoma margin detection [45] and oral carcinoma diagnosis [44]. It measures the variation of lifetime values over the region of interest, which provides a direct contrast image. Both wide-field-based FLIM [115] and scanning-based FLIM [47] have been investigated as intraoperative clinical tools. The wide-field FLIM image modality uses a fibre bundle with tens of thousands of optical fibres and an image detector. There are several disadvantages when applying this technique in clinical studies.

First, it is easy to lose the registration of position during the measurement due to the movement of the fibre probe. Second, the gated image detector has lower sensitivity and longer data collection time compared with the PMT-based detector system. Finally, the sample may have non-uniform illumination due to the curvature of tissue surface. Scanning-based FLIM is much more straightforward because the fluorescence decay can be collected at each pixel in sequence by scanning the illumination beam over the region of interest. In addition, a single-point detector such as PMT or avalanche diode is enough to collect the decay signal; this also reduces the instrument cost.

Hyperspectral FLIM that collects lifetime images over a broad spectral range has the advantage of observing the changes of fluorescence lifetime both in spatial and spectral domain. However, this configuration is limited by current time-resolved fluorescence instruments and is very time-consuming to fully resolve the weak fluorescence emission spectrally, temporally and spatially. For example, by using conventional scanning grating based monochromator, the spectra and lifetime can be collected over a broad spectral region. However, the acquisition time is relatively long (~45 seconds) [16]. Multiple band-pass filters were used in recent TRF instruments. The fluorescence signals could be collected at several wavelengths simultaneously to reduce the data acquisition time [45, 47, 116, 117]. However, only limited spectral bands were collected (*e.g.* 390 nm/40 nm, 450 nm/45 nm, and 520 nm/50 nm [117]), which may not be sufficient to resolve the overlapping autofluorescence spectra. To overcome this challenge, Beule *et al*. [118] designed a hyperspectral fluorescence lifetime system to collect spectra and temporal decay profiles by using a spectrometer and a PMT with 16 channels. This configuration is still time-consuming for clinical studies. Moreover, the spectral channels are determined by the numbers of PMT channels. It is not feasible to switch the wavelengths during clinical studies. On the other hand, Yuan *et al*. [43] proposed a design to collect spectrum and lifetime using an acousto-optical tunable filter (AOTF). The diffracted wavelength can be switched within several microseconds by applying different acoustic frequency on the AOTF crystal. By taking this advantage of AOTF, it is possible to realize a hyperspectral imaging configuration.

This chapter reports a scanning-based spectrally and temporally resolved fluorescence lifetime imaging system modified from the single-point TRF subsystem. This setup allows us to reconstruct the intensity and lifetime images over a broad spectral range. An AOTF was used to switch the diffracted wavelength rapidly in order to obtain the fluorescence signals at different wavelengths. The lifetime acquisition was achieved by using a high-speed photon detector and a fast digitizer in real-time. The 2-D images were acquired by scanning a fibre probe using a translation stage, which can be modified

with other beam scanning techniques in the future. The performance was characterized and validated using standard fluorescence dyes and biological tissue samples. The results illustrated that the system has the ability to resolve the different fluorophores and autofluorescence spectrally and temporally.

7.2. Methods and materials

7.2.1. System configuration

A schematic view of the hyperspectral FLIM system is shown in Figure 7-1. This system was modified from the AOTF-based time-resolved fluorescence (TRF) spectroscopy subsystem described in Chapter 3. The system is capable of obtaining the fluorescence decay signals in the spectral range of 370-550 nm. A fibre optic probe with 400 µm core and 0.12 NA was used to collect fluorescence signals. In order to generate 2-D images, a motorized scanning stage (MS2000, ASI, Eugene, OR) was used to hold the fibre optic probe to realize the scanning configuration. A pulse generator was used to control the data collection. In this way, time-resolved fluorescence signals from each pixel can be collected in sequence and the images of the scanning area can be constructed after the data collection.

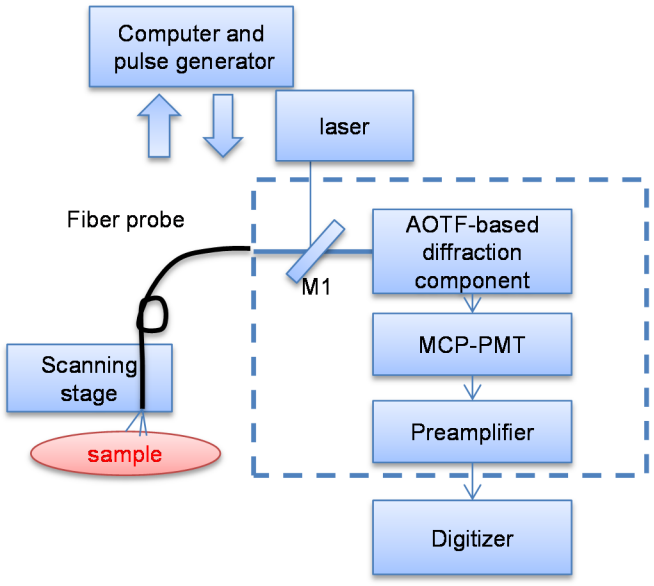

Figure 7-1. Schematic view of the hyperspectral FLIM configuration. AOTF: acousto-optic tunable filter, MCP-PMT: multichannel plate-photomultiplier tube, and M1: dichroic mirror.

7.2.2. Data acquisition

Control software of scanning module programmed in C++ was used to perform a 2-D

raster scanning to acquire the time-resolved signals at each pixel. Signals at 18 wavelengths from 380 nm to 550 nm with 10 nm intervals were collected in each pixel. Ten pulses were averaged to obtain a signal with high signal-to-noise. Therefore, there are a total of 180 pulses acquired at each pixel within 300 ms. In this setup, the fluorescence wavelengths can be selected in the software according to the requirement of clinical studies. The flow chart of the data acquisition is shown in Figure 7-2. The system components, including the AOTF, digitizer, the scanning stage, and the pulse generator, were first initialized to load the data acquisition setting. The scanning parameters, including the numbers of scanning pixels, scanning steps, and scanning wavelengths, can also be set in the software interface. Time-resolved fluorescence signals of each pixel were acquired and saved into a computer in sequence. Additional data analysis was carried out in a graphical-user-interface software programmed in MATLAB: 1) to retrieve the lifetime using the Laguerre-based deconvolution [92], 2) to calculate fluorescence steady-state spectra, and 3) to reconstruct hyperspectral lifetime images.

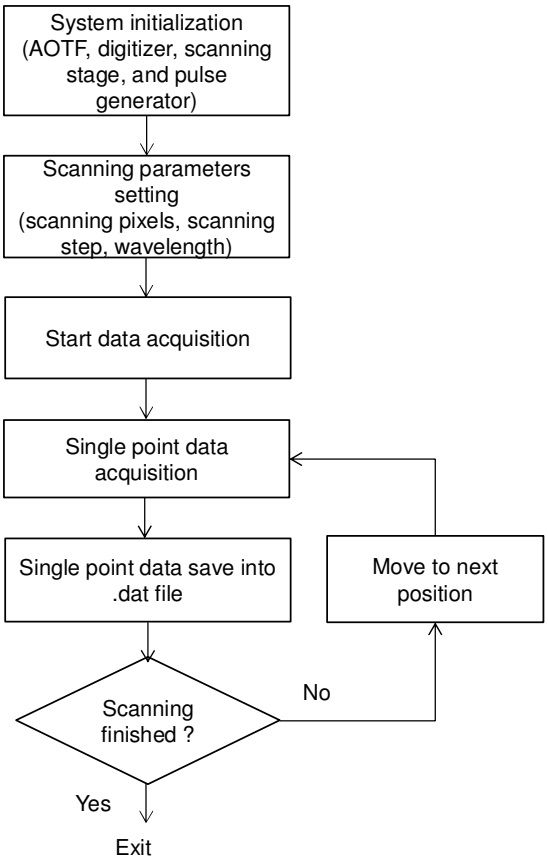

Figure 7-2. The flow chart of hyperspectral FLIM data acquisition.

7.2.3. Phantom preparation

The performance of the system was calibrated and validated using three standard fluorescence dyes: 0.1 mM fluorescein in ethanol (emission peak: 515 nm and lifetime: 4.1 ns [16]), 1 mM 9-cyanoanthracene in ethanol (emission peak: 445 nm and lifetime: 11.8 ns [16]), and 0.1 mM coumarin-6 in ethanol (emission peak: 510 nm and lifetime: 2.5 ns [95]).

Solid phantoms were used to validate the capability of the system to obtain hyperspectral images. Phantom matrices were fabricated to simulate the optical properties of biological tissue: 1 gram agar powder (A1296, Sigma-Aldrich, St. Louis, MO) was slowly mixed into 50 mL boiled deionized water and cooled to the room temperature. Intralipid (20% v/v Baxter Corp, Toronto, Ontario) with a volume of 2.5 mL was added into the agar solution during the cooling process to achieve a reduced scattering coefficient of 1.6 mm^{-1} at 460 nm. This was calculated based on Intralipid calibration data measured by a photospectrmeter. Fluorescence phantoms were achieved by adding fluorescent dye solutions into the phantom matrix solution during the cooling process. Small capillary tubes with outer diameter of 1 mm, inside diameter of 0.5 mm were used to hold the solid fluorescence phantom, and then inserted into the phantom matrix to obtain different phantom patterns.

To validate the performance of hyperspectral FLIM, several phantoms were fabricated as shown in Figure 7-3. Phantom #1 was a pair of capillary tubes with fluorescein that were embedded at the surface of the phantom matrix. This was used to characterize the effect of the scanning step on the imaging quality. Phantom #2 included three capillary tubes with different fluorescence dyes (fluorescein, 9-cyanoanthracene, and coumarin-6) which were embedded parallel at the surface of the phantom matrix gel for observing the performance of one-dimensional raster scanning. Phantom #3 included three capillaries of fluorescence dyes (fluorescein, 9-cyanoanthracene, and coumarin-6) inserted in the phantom matrix in the perpendicular direction. This phantom was used to validate the capability of the system to resolve different fluorescence dyes by lifetime and intensity characteristics.

It should be noted that the agars gel did not emit fluorescence with the excitation at 355 nm, whereas Intralipid has the strong fluorescent emission that cannot be ignored. Therefore, the background signal was measured from a phantom matrix without fluorescence dye but with same optical properties and then subtracted from the measured fluorescence signals.

Besides fluorescence phantoms, fresh porcine skin specimens purchased from a local

butcher shop were tested in this study. Two solid fluorescent phantoms (9-cyanoanthracene and fluorescein) were embedded into the porcine skin to determine the sensitivity of our system in differentiating the distinct features (chemical composition and structures) of the fluorophores from the autofluorescence background. Saline was used to keep the tissue wet during the experiment.

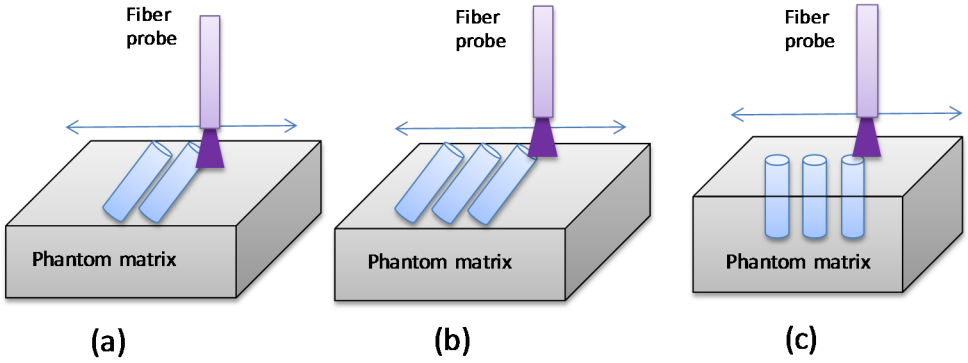

Figure 7-3. Diagrams of different solid phantom patterns. (a) Phantom #1, (b) Pantom#2, and (c) Phantom #3.

7.3. System validation on tissue phantoms and biological tissue

7.3.1. Scanning system calibration

2-D hyperspectral FLIM was obtained by scanning the fibre probe using the 2-axial translation stage. The spatial resolution of the image depends on many factors including optic-fibre core diameter and numerical aperture, scanning step, illumination beam size, and probe-to-target distance. In this section, we investigated the effects of the aforementioned parameters on the spatial resolution.

To characterize the effect of scanning step on spatial resolution, the fluorescence emission of phantom #1 was measured with different scanning steps (0.1 mm, 0.2 mm, and 0.3 mm). Fluorescence decay at the emission peak of 515 nm was acquired over a scanning area of 5 × 2 mm^2. Figure 7-4a and 7-4b show the intensity and lifetime images, respectively. The average lifetime values did not change with the scanning steps, whereas the imaging quality degraded as the scanning step increased from 0.1 mm to 0.3 mm; especially in the lifetime images of 0.2 mm and 0.3 mm scanning steps, where the fluorescence tube cannot be visualized. Figures 7-4c and 7-4b show the intensity and lifetime variation over the cross section. The FWHM of the intensity profiles did not changes with the scanning steps.

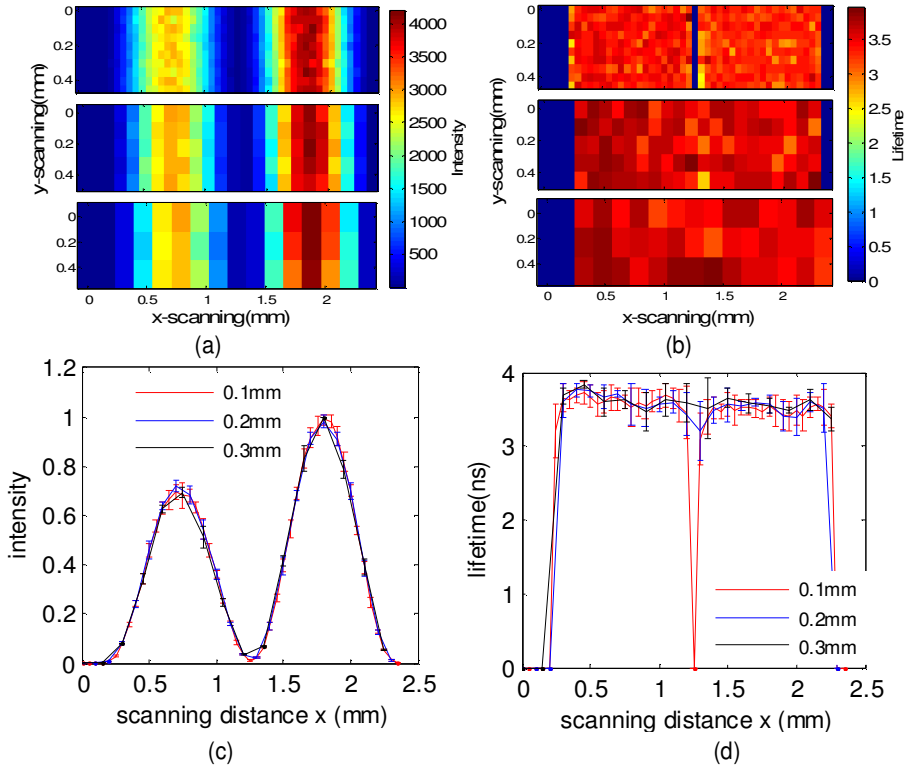

Figure 7-4. Effects of the scanning steps on the spatial resolution (image quality). The intensity (a) and lifetime (b) images are obtained at three different scanning steps (top to bottom: 0.1 mm, 0.2 mm, and 0.3 mm). (c) and (d) the cross intensity and lifetime variance along the x-scanning direction respectively. : The FLIM images were collected from the fluorescence phantom #1 at 515 nm.

During clinical studies, the probe-to-target distance (PTD) may change over the scanning area due to the curvature of biological samples. Therefore, both the laser illumination area and power change at each location of the tissue surface and affect the spatial resolution of the images. The effect of the PTD on spatial resolution was investigated by holding the fibre probe at different positions (0.5 mm, 2 mm, and 5 mm) above the surface of the tissue phantom. The illumination area and power of laser beam on the sample were calculated at different PTDs as shown in Table 7-1. The laser power density deceased dramatically when increasing the PTD. Two-D FLIM images of intensity and lifetime from different PTDs are shown in Figure 7-5a and Figure 7-5b, respectively. Figure 7-5c and 7-5d provide the variations of the intensity and lifetime across the x-scanning direction, respectively. Fluorescence intensity decreased significantly with the increase of PTD and caused a low signal-to-noise ratio of the image. The margin of capillary tubes cannot be identified in the lifetime image with PTD of

5 mm.

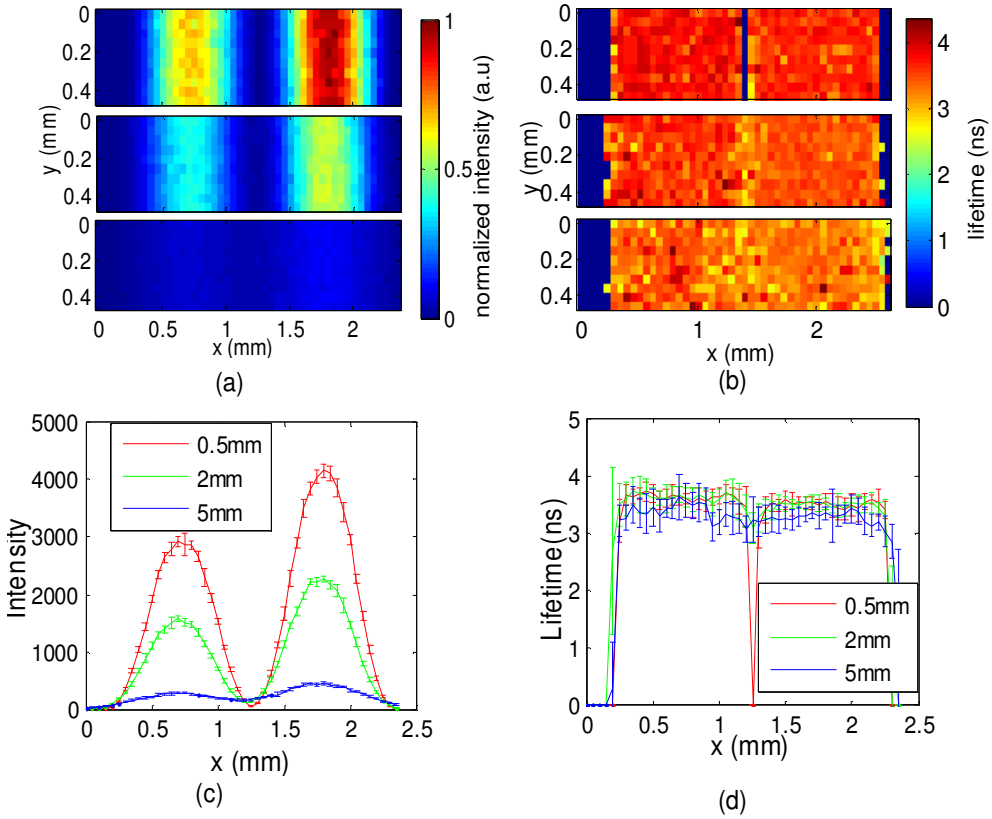

Figure 7-5. Scanning performance with different probe-target distances (PTD). (a)The intensity and (b) lifetime images at different PTDs. The cross intensity and lifetime changes along the x-scanning direction are shown in (c) and (d) respectively.

Table 7-1. Laser illumination area and power of each PTD

PTD (mm)	Illumination area (mm^2)	Power ($\mu J/mm^2$)
0	0.126	19.9
0.5	0.212	11.8
2	0.608	4.11
5	2.009	1.24

In order to verify the stability of scanning module, the forward and reverse scanning over the phantom #1 were collected. Figure 7-6 shows the intensity and lifetime over the scanning direction. The results illustrated that the intensity and lifetime were stable for both forward and reverse scanning.

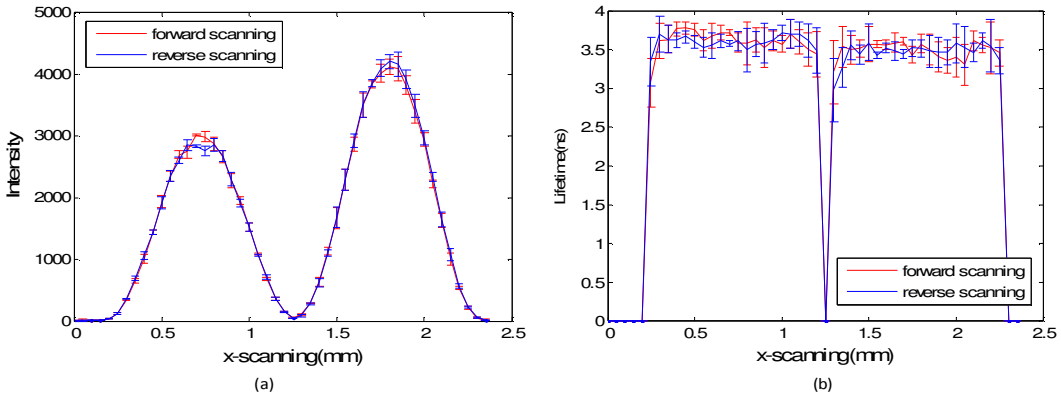

Figure 7-6. Scanning performance of stability for forward and reversed scanning. (a) Intensity, (b) lifetime.

7.3.2. 1-D scanning for different fluorescence dyes

The one-dimensional raster scanning was performed on the phantom #2. The fibre probe was placed at 1 mm above the surface of the phantom. Time-resolved spectroscopy was obtained at a raster scanning distance of 6.5 mm with a scanning step of 0.3 mm as shown in Figure 7-7. Figure 7-7a demonstrates the changes in the steady-state spectra over the scanning distance. The fluorescein, courmain-6, and 9-cyanoanthracene can be identified straightforward according to their spectral features. Figure 7-7b presents the intensity changes over the scanning distance at different wavelengths of 515 nm, 490 nm, and 435 nm that perform the emission peaks of fluorescein, coumarin-6, and 9-cyanoanthracene respectively. Meanwhile, the average lifetime values varied from 4 ns to 2.5 ns and finally became 11.8 ns across over the scanning distance, which indicates the position of fluorescein, courmain-6, and 9-cyanoanthracene, respectively.

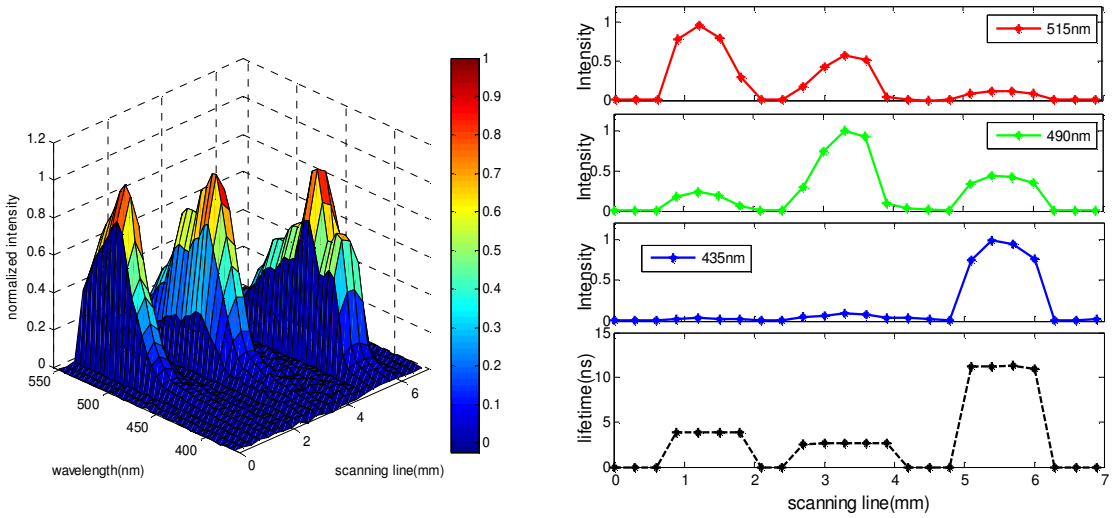

Figure 7-7. One-dimensional raster scanning preformed on the fluorescence phantom #2. (a) The time-resolved fluorescence spectra over the raster scanning length. (b) The intensity mapping at the emission peak wavelengths of three fluorescence dyes (515 nm, 490 nm, and 435 nm) as well as averaged lifetime over the scanning distance

7.3.3. Fluorophores in the tissue phantom

The performance of hyperspectral FLIM system was validated on the tissue phantom to characterize its capability of resolving multiple fluorophores spectrally, temporally, and spatially. Figure 7-8c shows the arrangement of three embedded fluorophores within Phantom #3. The fluorescence decays were collected in the range of 380-550 nm with 10 nm intervals for each pixel. The total scanning area was 3.5×1.5 mm^2 with 0.05 mm scanning step. After data acquisition, the hyperspectral intensity and lifetime images were constructed off-line. Figure 7-8a and 7-8b show the fluorescence intensity and averaged lifetime images obtained from five wavelengths: 410 nm, 450 nm, 510 nm, 520 nm, and 550 nm. As expected, 9-cyanoanthracene is clearly visible in the centre of the intensity and lifetime images at 410 nm and 450 nm with an average lifetime of 11.2 ns. Its intensity decreased at longer wavelength whereas the lifetime remained constant. Fluorescein and courmarin-6 shared the same intensity variation trend but have different lifetime values (2.6 ns for coumarin-6, 3.9 ns for fluorescein) in the range of 450 nm to 550 nm. The averaged spectra and lifetime of these three fluorophores in the phantom are shown in Figure 7-8d and 7-8e respectively, which provides the detailed intensity and lifetime variation information over the observed spectral range. We can see that 9-cyanoanthracene has a broad emission spectrum in the wavelength range of

400-550 nm, while fluorescein and coumarin-6 emit between 450-550 nm. Although the coumarin-6 and fluorescein have similar emission spectra, they still can be distinguished using lifetime features. The average lifetime values at the emission peaks of coumarin-6, 9-cyanoanthracene, and fluorescein have been shown in Table 7-2, which are in very good agreement with Refs [16,95]. These results demonstrate that a combination of both spectral and time-resolved fluorescence features can be used to resolve the fluorescence emission of multiple fluorophores. Moreover, images also provide us with the morphological feature of each fluorophore, thus helping to identify the location of the fluorophores.

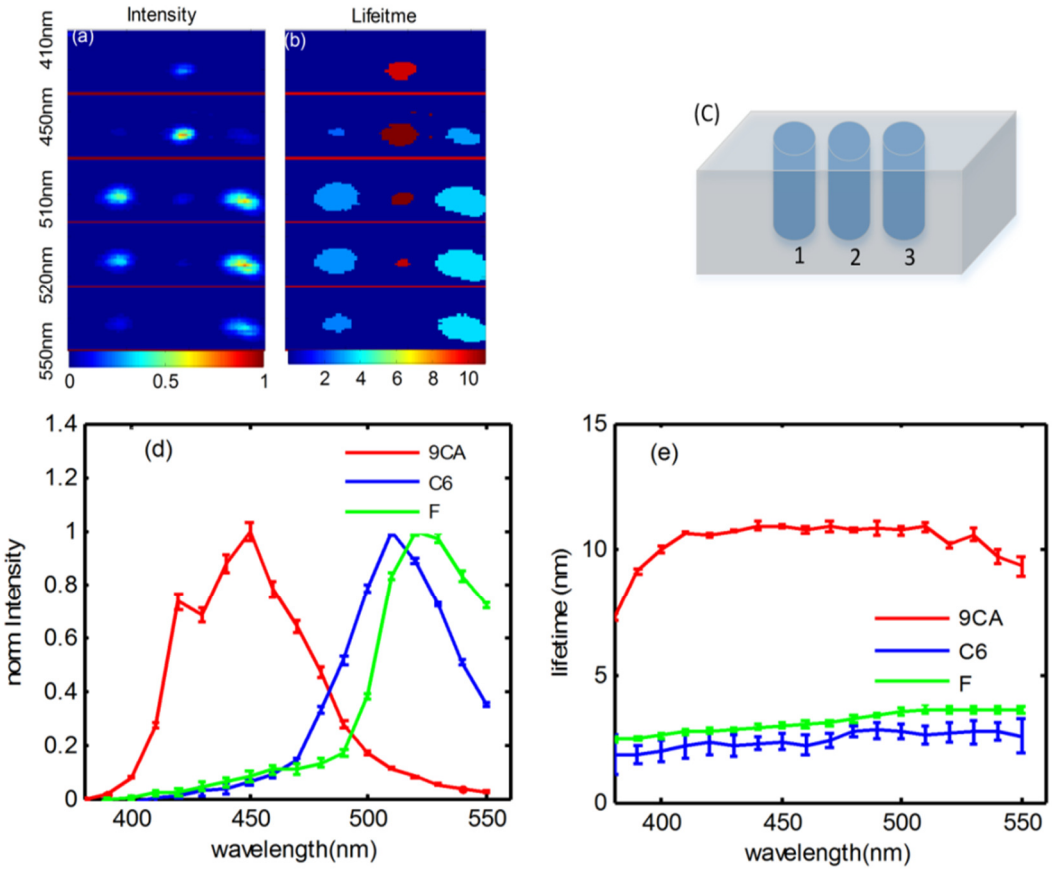

Figure 7-8. Spectral and temporal resolving of the fluorescence emission for three fluorophores embedded in the phantom matrix. The intensity (a) and lifetime (b) images are obtained at different wavelengths (410 nm, 450 nm, 510 nm, 520 nm, and 550 nm) over a 3.5 ×1.5 mm^2 area. (c) A schematic view of the phantom #2 (#1: Coumarin-6, #2: 9-cyanoanthracene, and #3: fluorescein). Normalized intensity (d) and lifetime (e) spectroscopy can provide the detailed information of three different fluorophores.

Table 7-2. Lifetime for three fluorescence phantoms

Fluorophores	Emission peak (nm)	Lifetime (ns)	Reference
Coumarin-6	510	2.6 ± 0.1	2.5
9-cyanoanthracene	450	11.2 ± 0.4	11.8~12.8
Fluorescein	515	3.9 ± 0.2	4.1

7.3.4. Biological tissue study

The system was also validated using fresh porcine skin specimens to demonstrate the capability of acquiring the autofluorescence from biological tissue. The scanning area is 4.5×3 mm^2 (30×20 pixels) with 0.15 mm scanning step. Figure 7-9a and 7-9b show the intensity and lifetime images at 405 nm, 450 nm, and 515 nm. The embedded fluorescence dyes were clearly resolved against the autofluorescence background from the skin tissue. The 9-cyanoanthracene is resolved at both 405 nm and 450 nm wavelengths, whereas the fluorescein is observed at 515 nm. The autofluorescence of the porcine skin has strong intensity emission and lifetime around 4.5 ns at the images of 405 nm and 450 nm, which are primarily contributed by collagen (emission peak around 390 nm to 405 nm) and elastin (emission peaks around 440 nm to 460 nm) in skin tissue. The decrease of 9-cyanoanthracene lifetime at 515 nm is attributed to diffusion of the fluorescein dyes in same area. Figure 7-9d and 7-9e present the intensity and lifetime spectroscopy of the selected spots from the porcine skin specimen and the embedded fluorescence dyes as the black arrows point out in Figure 7-9b. We can see that the autofluorescence of the porcine skin tissue has a broad emission spectrum with a peak at 440 nm, and then decreases quickly after 500 nm, whereas the fluorescein has a relatively narrow emission spectrum with a peak at 515 nm. In the time-resolved spectrum, the autofluorescence lifetime value of the porcine skin tissue decreased at longer wavelengths, whereas the fluorescein lifetime remained constant at around 4 ns over the spectral region. Therefore, the fluorescein target was easily resolved from the skin tissue based on the chemical and morphological features. This experiment demonstrated that the system is capable of measuring the autofluorescence of biological tissue and distinguishing the fluorescence targets from the autofluorescence background.

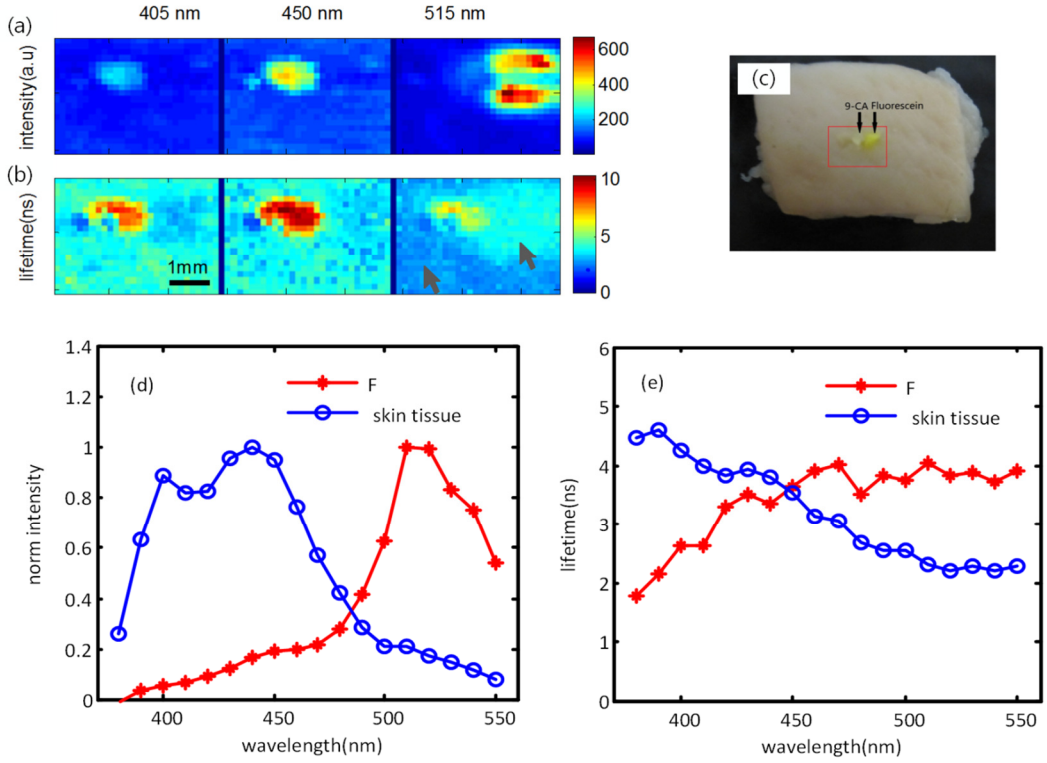

Figure 7-9. The evaluation results of the hyperspectral FLIM on the porcine skin specimen with the fluorescence targets to observe its ability to spectrally and temporally resolve autofluorescence and distinguish the fluorescence targets against autofluorescence background. Fluorescence intensity (a) and lifetime (b) images are shown at different wavelengths (405 nm, 450 nm, and 515 nm). (c) A photograph of the porcine skin specimen with two fluorescence targets [fluorescein (F), 9-cyanoanthracene (9-CA)]. The scanning area is marked by the red square. Normalized intensity (d) and lifetime (e) spectroscopy at the selected spots from the skin tissue and fluorescein (black arrows in (b)).

7.4. Discussion

An AOTF-based hyperspectral FLIM system was presented in this Chapter. It is able to spectrally, temporally, and spatially resolve the fluorescence signals from biological tissue in the wavelength range of 370-550 nm. Fluorescence intensity and lifetime images at different wavelengths can be constructed from the fluorescence decay signals after the data acquisition. The data acquisition time is ~ 300 ms for each pixel, which is compatible with clinical studies. Currently, the acquisition time of 2-D hyperspectral FLIM is limited by the laser repetition rate of 1 kHz. Some high repetition rate UV lasers are now available and may further reduce the data acquisition time [47]. In this study, a

2-axial motorized stage was used to move the fibre in order to demonstrate the feasibility of generating a 2D FLIM image, *e.g.* demonstrating spatial resolving capability. Although this setup is useful for *ex vivo* investigation of specimens removed from patient, it is certainly not intended to be used for *in vivo* studies. There are many high-speed beam-scanning techniques exist (*e.g.* galvanometer mirrors, rotating fibres) which will be used in our system in future.

The spatial resolution of the FLIM images depends on many factors such as the scanning step, the fibre probe size, and the probe-to-target distance. The relationship between the scanning step and the spatial resolution is illustrated in Figure 7-4. The scanning step can be changed during the experiment to obtain an expected spatial resolution. In many cases, the spatial resolution of surgical margin detection is around 1-2 mm [120]. Therefore, this system is feasible to detect the tumour margin with sufficient spatial resolution. The resolution of our system is limited by the 400 μm core fibre size. In further beam steering setup, where a focusing Gradient refraction index (GRIN) lens may be used, the focal spot size is expect to be much smaller [119].

In conclusion, a hyperspectral fluorescence lifetime imaging setup that provides the multi-dimensional information of endogenous and exogenous fluorophores in space, spectrum, and time was demonstrated. The performance of system has been characterized and evaluated using fluorescence tissue phantoms and biological tissue. The results suggest that this technique has a potential to be used as an optical biopsy tool for tissue diagnosis.

Chapter 8 Conclusion and future work

The combination of the fluorescence and diffuse reflectance spectroscopy towards intraoperative detection of brain tumour margin is presented in this dissertation. This chapter provides a summary of the work presented and suggests further research inspired from current state of art optical techniques and an outlook on the future of the optical biopsy technique for clinical application.

8.1. Conclusion

Optical biopsy provides a promising minimally invasive tool to determinate biochemical composition and morphological structures of biological tissue in real-time. Fluorescence spectroscopy and diffuse reflectance (DR) spectroscopy are two common optical biopsy modalities. The goal of this dissertation is to combine the time-resolved fluorescence (TRF) and DR spectroscopy for the intraoperative detection of brain tumour margin. Several milestones have been achieved towards this goal.

- A clinically compatible TRF-DR spectroscopy system was developed as an intraoperative tool for clinical studies. It was calibrated, and evaluated using the tissue phantom to demonstrate its capability of detecting the fluorescence and optical properties accurately (Chapter 3 and Chapter 4).
- A robust Laguerre-based deconvolution method was optimized to retrieve impulse response functions accurately and quickly from measured signals with low SNR (Chapter 5). In addition, a fast selection method of Laguerre parameters was developed for real-time analysis during clinical studies.
- A pilot study on the *ex vivo* brain specimens has been carried out to investigate the fluorescence and diffuse reflectance properties of different brain tumour types (Chapter 6). Fluorescence features can be used to discriminate the different tumour types.
- A hyperspectral fluorescence lifetime imaging system was proposed to collect fluorescence lifetime images for optical biopsy (Chapter 7).

The integrated TRF-DR spectroscopy instrument was built and calibrated to retrieve fluorescence and diffuse reflectance signals from biological samples. The fluorescence spectra and lifetime, as well as the spatially resolved diffuse reflectance spectra can be collected using a dual-modality fibre optic probe near real-time (2s). The fluorescence

decays at different wavelengths are collected by the AOTF-based spectrometer, whereas the steady-state fluorescence spectra can be collected by the grating-based spectrometer. The spatially resolved diffuse reflectance spectra at three different source-detector distances are collected by three independent spectrometers. The system was performed on the fluorescence phantoms. The results indicate that our system has the ability to accurately retrieve the fluorescence and diffuse reflectance properties of the samples.

Towards on-line diagnosis, the Laguerre deconvolution method was optimized to overcome the over-fitting problem that was introduced by the low signal-to-noise ratio and high-order Laguerre functions. The physical profiles of fluorescence decay were used to constrain the least squares fitting. In addition, a look-up table of the optimized Laguerre scale parameter α for different lifetime values was generated to realize fast Laguerre parameter selection during the clinical study.

A pilot study on the *ex vivo* brain specimens was investigated using the time-resolved fluorescence and diffuse reflectance spectroscopy. The fluorescence and diffuse reflectance characteristics of different tumour types including meningiomas (grade I, grade II) and high-grade gliomas (glioblastoma multiforme, astrocytoma oligodendroglioma) have been demonstrated in this study. Meningiomas show higher intensity and larger lifetime value at 400 nm due to its high collagen concentration. Some spectral and time-resolved features (*e.g.* intensity ratios, lifetime values, and the LEC ratios) were selected to classify the different tumour types that are categorized based on the diagnostic results. The meningioma grade I can be differentiated from the meningioma grade II with the sensitivity and specificity of both 100%. However, due to lack of detailed histopathological results and limited specimens volumes, this classification results need to be carefully interpreted.

In addition, to overcome the small detection tissue volume of single-point measurements, a hyperspectral fluorescence lifetime imaging setup was developed to provide the fluorescence lifetime and intensity images for tissue diagnosis. It can resolve the fluorescence features of biological tissue spectrally, spatially, and temporally, which may improve the accuracy of tumour margin detection.

8.2. Future works

8.2.1. Clinical studies

The changes in biochemical composition and morphological structures of tumours can be used to indicate its tissue statues, thus finding the resection margin during neurosurgery. The pilot study on the brain specimens using the time-resolved fluorescence and diffuse reflectance spectroscopy has demonstrated their potential as

intraoperative tissue diagnostic tools. However, the result of this investigation is limited by the sample size, which may not reflect the real properties of different tumour types. Therefore, a large number of clinical studies are needed to evaluate the sensitivity and specificity of the discrimination models. In addition, gliomas especially high-grade gliomas are the primary causes of patient death of brain tumours. Our future clinical studies will focus on the discrimination between the high-grade gliomas and the surrounding normal tissue to improve the resection accuracy.

8.2.2. Intrinsic fluorescence extraction from turbid tissue

The absorption and scattering properties of turbid tissue alter the laser and autofluorescence signals in TRF measurements. From the experimental results in Section 4.3, fluorescence lifetime was not altered by the optical properties, whereas the fluorescence intensity varied with the changes in optical properties. Therefore, the distortions on fluorescence intensity are the main problem that needs to be solved to obtain the intrinsic fluorescence signal. Diffuse reflectance spectroscopy provides a method to retrieve the optical properties at the same tissue volume with fluorescence measurements. Hence, once we obtain the optical properties in the UV-visible range from DR measurements, it is possible to estimate the transmission path of the laser and fluorescence signals in biological tissue, thus determining the exact location of the excited fluorophores in the tissue and retrieving the intrinsic fluorescence spectrum.

Several intrinsic fluorescence recovery methods have been investigated using the diffuse reflectance theory [78, 79] and the Monte Carlo simulation [81-83]. In our case, since the diffuse reflectance spectroscopy and fluorescence spectroscopy are collected from different channels, the diffuse reflectance spectroscopy cannot directly predict the fluorescence transmission path using the diffuse theory. Therefore, both the laser and fluorescence transmission in the tissue will be estimated using the Monte Carlo simulation using calculated optical properties. A series fluorescence phantoms with different optical properties will be prepared and measured to investigate the relationship between the fluorescence distortions and optical properties of turbid tissue. A look-up table will be created based on this simulation and experimental results. It can be used to determine the intrinsic fluorescence signal during the clinical study in real-time [121].

8.2.3. Intraoperative hyperspectral FLIM for neurosurgery

The hyperspectral FLIM demonstrated in Chapter 7 can be used to resolve the fluorescence signal in spectra, time, and space. However, the current configuration is not suitable for the *in vivo* clinical study due to the large-size of scanning stage and slow scanning speed. In the future, the laser with the high repetition rates can be used to

improve the scanning speed. Other scanning techniques, such as galvanometer mirrors and rotating fibres, also can be used to minimize the size of scanning module.

8.3. Closing remarks

The work presented in this dissertation has been dedicated to the improvement of the performance of TRF and DR spectroscopy towards intraoperative tumour margin detection. A clinically compatible integrated TRF-DR spectroscopy instrument was built, calibrated, and evaluated for optical biopsy studies. A robust Laguerre-based deconvolution method has been optimized to solve the over-fitting and oscillation problems. In addition, a pilot study on the *ex vivo* brain specimens was carried out to investigate the fluorescence and diffuse reflectance characteristics of different brain tumour types. The results demonstrated the feasibility of TRF and DR spectroscopy in resolving the different tissue types. A hyperspectral fluorescence lifetime imaging setup was also developed to resolve the fluorescence signal from biological tissue. The findings of this thesis will act as a springboard to inform future research of intraoperative detection of brain tumor margin using optical biopsy methods.

Appendix I: AOTF background noise

A weak background was found at the position of the diffracted beams after the light transmitted through the AOTF crystal as shown in Figure AI-1a. This was caused by the light scattered from the crystal surface and the bulk. The background introduced a background decay signal in the fluorescence decay as shown in Figure AI-2. For the steady-state signal measurement, this background signal could be easily eliminated during the measurement by subtracting it from the measured signal. However, for the time-resolved fluorescence measurement, it is very hard to compensate by subtracting the background signal which will introduce errors in the deconvolution. To eliminate the background, an Iris with the aperture of 6 mm diameter was aligned in the optical path right after the plano-convex lens to block the dispersed fluorescence light away from the collimated beam. Therefore, the background light was eliminated as Figure AI-1 shows.

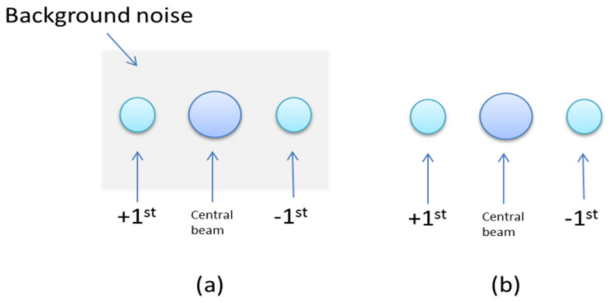

Figure AI-1. Background noise caused by dispersed fluorescence light. (a) and (b) are the diffraction beam with /without the 6 mm aperture.

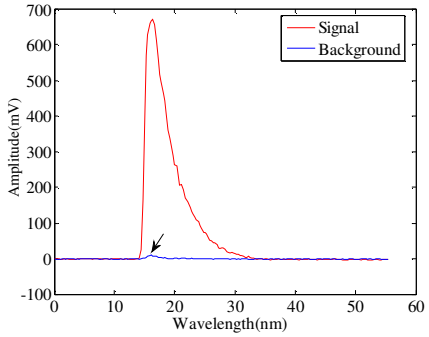

Figure AI-2. The background noise decay was introduced by the scattered light from the AOTF crystal at the diffracted beam position.

Appendix II: AOTF calibration results

RF frequency (MHz)	Wavelength (nm)	Left (nm)	Right (nm)	Amplitude (%)	Difference-O-ray (nm)	Difference e-ray (nm)
182.5	370	370.2	369.9	20%	0.2	-0.1
177.69	375	374.6	375.5	17%	-0.4	0.5
173.45	380	379.9	380.2	14%	-0.1	0.2
168.52	385	384.9	385.5	14%	-0.1	0.5
164.58	390	389.6	390.2	11%	-0.4	0.2
161.03	395	394.7	395.2	9%	-0.3	0.2
157.15	400	400	400.6	9%	0	0.6
153.57	405	404.7	405.3	10%	-0.3	0.3
150.5	410	409.7	410.3	11%	-0.3	0.3
147.35	415	415	415.3	11%	0	0.3
144.35	420	420	420.3	14%	0	0.3
141.6	425	424.7	425.3	14%	-0.3	0.3
138.8	430	429.7	430.3	14%	-0.3	0.3
136.13	435	435	435.3	14%	0	0.3
133.9	440	439.8	440.1	14%	-0.2	0.1
131.58	445	444.8	445.1	14%	-0.2	0.1
129.38	450	449.5	450.1	14%	-0.5	0.1
127.25	455	454.9	455.2	16%	-0.1	0.2
124.95	460	459.9	460.2	18%	-0.1	0.2
122.97	465	464.9	465.2	18%	-0.1	0.2
121	470	470	470.3	20%	0	0.3
119.27	475	474.7	475	25%	-0.3	0
117.32	480	480	480.3	40%	0	0.3
115.73	485	484.8	484.8	40%	-0.2	-0.2
113.98	490	489.8	490.1	40%	-0.2	0.1
112.34	495	494.8	495.1	50%	-0.2	0.1
110.77	500	499.9	500.3	50%	-0.1	0.3
109.22	505	504.9	505.2	50%	-0.1	0.2
107.73	510	509.9	510.2	50%	-0.1	0.2
106.85	515	515	515.3	50%	0	0.3
104.85	520	520	520	50%	0	0

103.5	525	525	525	50%	0	0
102.2	530	529.8	530.1	50%	-0.2	0.1
100.85	535	534.8	535.1	50%	-0.2	0.1
99.7	540	539.8	540.1	50%	-0.2	0.1
98.4	545	544.9	545.2	50%	-0.1	0.2
97.22	550	549.9	550.5	50%	-0.1	0.5

Appendix III: Data analysis software in Chapter 5

The Laguerre-based deconvolution method was used in this study. The program was developed in the MATLAB (2013a, MathWork). The flowcharts of the data preprocessing and the Laguerre-based deconvolution method are shown in Figure AIII.1 and Figure AIII.2 respectively.

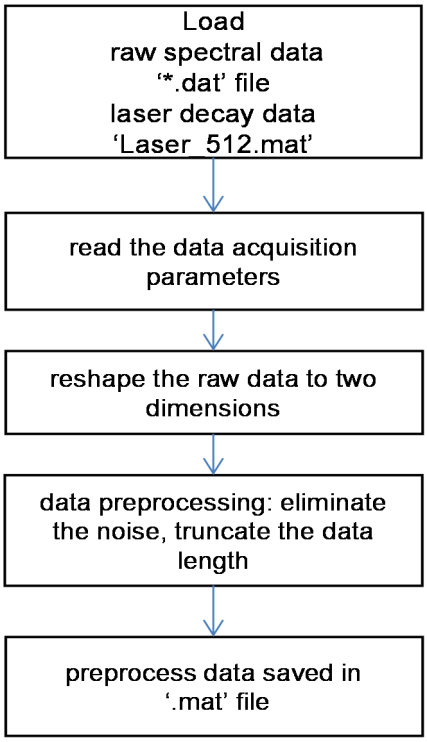

Figure AIII-1. Data preprocessing flow chart.

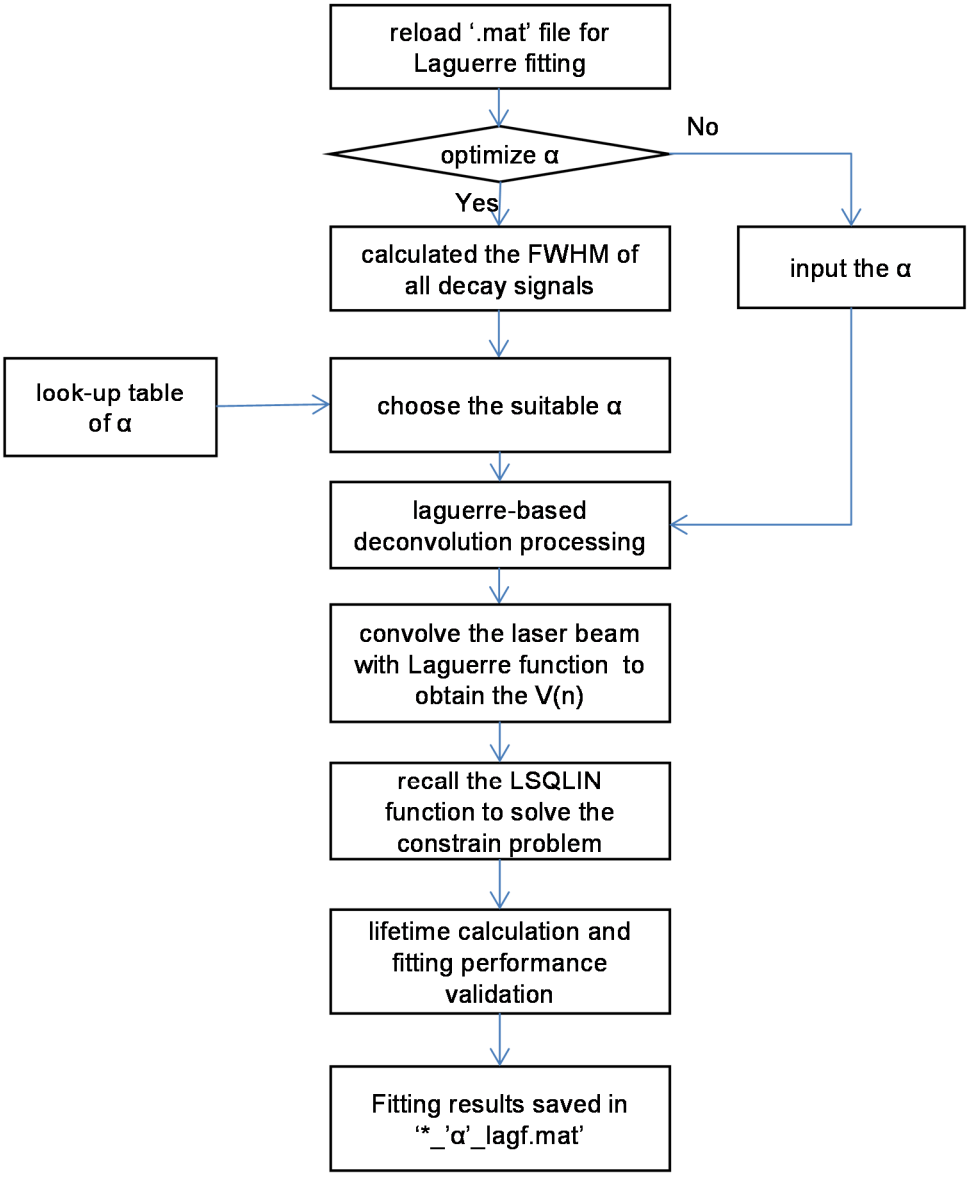

Figure AIII-2. The flow chart of the CLF -based deconvolution method

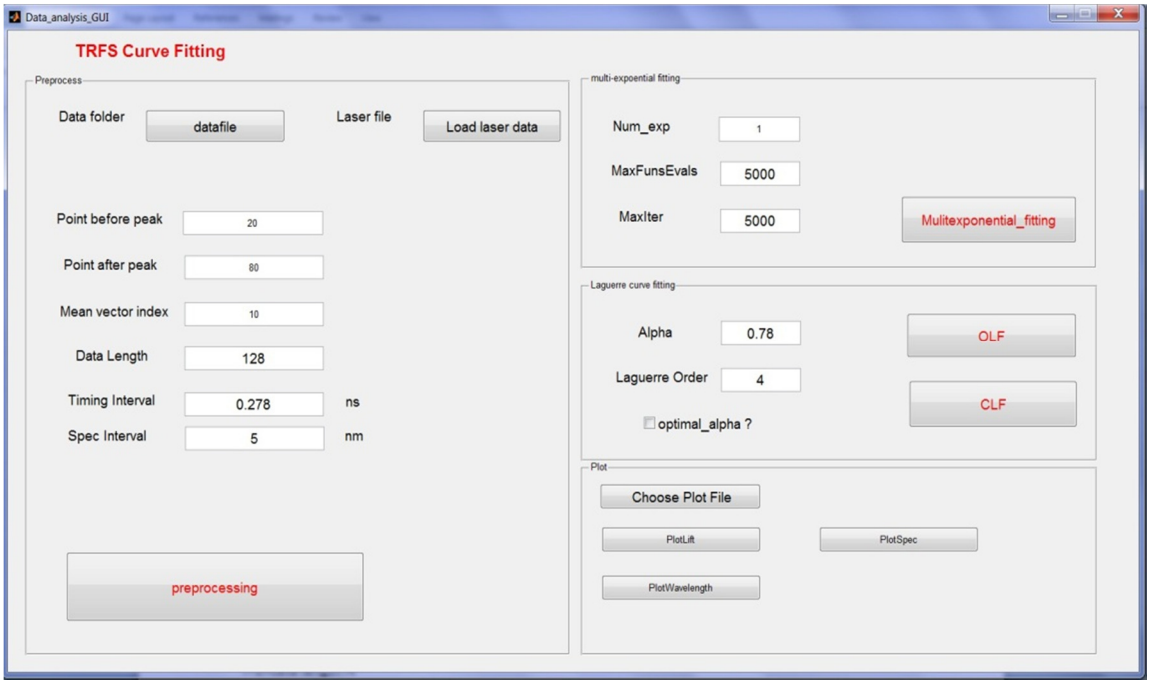

Figure AIII-3 Software user interface including the data preprocessing and deconvolution parts. Both multi-exponential-, CLF-, and OLF-based deconvolution methods can be used in this software.

References

1 P. N. Prasad, Introduction to biophotonics. 2003.

2 "CBTRUS Statistical Report: Primary Brain and Central Nervous System Tumors Diagnosed in the United States in 2004-2008," National Cancer Institute, 2012.

3 "Canadian Cancer Statistics 2012," Canadian Cancer Society, 2012.

4 Centers for Disease Control and Prevention, "Colorectal cancer rates by state" 2012. Link: http://www.cdc.gov/cancer/colorectal/statistics/state.htm

5 Y. Eyupoglu et al., "Surgical resection of malignant gliomas - role in optimizing patient outcome," Nat. Rev. Neuro. 9(3): 141-151, 2013.

6 P. V Butte et al., "Fluorescence lifetime spectroscopy for guided therapy of brain tumors," Neuroimage. 54(supp1): 125–135, 2011.

7 Y. Zhou et al., "Human brain cancer studied by resonance Raman spectroscopy," J. Biomed. Opt. 17(11): 116021, 2012.

8 N. Yaroslavsky et al., "Optical properties of selected native and coagulated human brain tissues in vitro in the visible and near infrared spectral range," Phys. Med. Bio. 47(12): 2059–2073, 2002.

9 A. Giese et al., "Non-invasive intraoperative optical coherence tomography of the resection cavity during surgery of intrinsic brain tumors," SPIE processing 6078: 60782Z 1–8, 2006.

10 J. Staley et al., "Growth of melanoma brain tumors monitored by photoacoustic microscopy," J. Biomed. Opt.15(4): 040510, 2013.

11 B. W. Pogue et al., "Review of Neurosurgical Fluorescence Imaging Methodologies," IEEE J. Sel. Top. Quantum Electron. 16(3): 493–505, 2010.

12 A. M. Zysk et al., "Optical coherence tomography: a review of clinical development from bench to bedside" J. Biomed. Opt. 12(5): 051403, 2007.

13 L. V. Wang and S. Hu, "Photoacoustic tomography: in vivo imaging from organelles to organs," Science 335(6075): 1458–1462, 2012.

14 R. Richards-Kortum and E. Sevick-Muraca, "Quantitative optical spectroscopy for tissue diagnosis," Annul. Rev. Rhys. Chem. 47: 555-606, 1996.

15 J. R. Lakowicz, Principles of fluorescence spectroscopy, 3rd editor, Springer, New York, 2006.

16 Q. Fang et al., "Time-domain laser-induced fluorescence spectroscopy apparatus for clinical diagnostics," Rev. Sci. Instrum. 75(1): 151-162, 2004.

17 J. R. Mourant et al., "Predictions and measurements of scattering and absorption over broad wavelength ranges in tissue phantoms," Appl. Opt. 36：949–957, 1997.

18 G. Zonios et al., "Melanin absorption spectroscopy: new method for noninvasive skin investigation and melanoma detection," J. Biomed. Opt. 13: 014017, 2008.

19 N. Rajaram et al., “Pilot clinical study for quantitative spectral diagnosis of non-melanoma skin cancer,” Lasers. Surg. Med. 42(10): 716-727, 2010.

20 M. D. Keller et al., "Autofluorescence and diffuse reflectance spectroscopy and spectral imaging for breast surgical margin analysis," Lasers. Surg. Med. 42(1): 15-23, 2010.

21 W. C. Lin et al., “In vivo brain tumor demarcation using optical spectroscopy,” Photochem and photobio 73(4): 396–402, 2001.

22 W. C. Lin et al., “Optical spectroscopy for in-vitro differentiation of pediatric neoplastic and epileptogenic brain lesions,” J. Biomed. Opt. 14(1): 014028, 2009.

23 P. A. Valdes et al., “Combined fluorescence and reflectance spectroscopy for in vivo quantification of cancer biomarkers in low- and high- grade glioma surgery,” J. Biomed. Opt. 16(11): 116007, 2011.

24 Z. Nie et al., “Hyperspectral fluorescence lifetime imaging for optical biopsy,” J. Biomed. Opt. 18(9):096001, 2013.

25 D. N. Louis et al., “The 2007 WHO classification of tumours of the central nervous system,” Acta neuropathologica, 114(2): 97–109, 2007.

26 W. J. Elias et al., “Cortical and subcortical brain shift during stereotactic procedures,” J. Neurosurg. 107(5): 983–988, 2007.

27 J. Sosna et al., “Intraoperative sonography for neurosurgery,” J. Ultrasound. Med. 24(12): 1671–1682, 2005.

28 P. L. Kubben et al., “Intraoperative MRI-guided resection of glioblastoma multiforme: a systematic review,” Lancet. Oncol. 12(11): 1062–70, 2011.

29 I. J. Bigio and J. R. Mourant, “Optical Biopsy,” Encyclopedia of Optical Engineering, 2: 1577–1593, 2003.

30 S. Koljenovic et al., “Discriminating vital tumor from necrotic tissue in human glioblastoma tissue samples by Raman,” Laboratory Investigation, 82(10): 1265–1277, 2002.

31 C. Krafft et al., “Near infrared Raman spectra of human brain lipids,” Spectrochim. Acta. A. Mol. Biomol. Spectrosc. 61(7): 1529–1535, 2005.

32 M. Kirsch et al., “Raman spectroscopic imaging for in vivo detection of cerebral brain metastases,” Anal. Bioanal. Chem. 398(4): 1707–1713, 2010.

33 D. Huang et al., “Optical coherence tomography,” Science 254(5035): 1178–1181, 1991.

34 S. A. Boppart et al., “Optical coherence tomography for neurosurgical imaging of human intracotical melanoma,” Neurosurgery 43(4): 834–841, 1998.

35 M. F. Kircher et al., “A brain tumor molecular imaging strategy using a new triple-modality MRI-photoacoustic-Raman nanoparticle,” Nat. Med. 18(5): 829–834, 2012.

36 M. C. Skala et al., “In vivo multiphoton microscopy of NADH and FAD redox states, fluorescence lifetimes, and cellular morphology in precancerous epithelia,” Proc, Natl. Acad. Sci USA 104(49): 19494–9, 2007.

37 G. A. Wagnieres et al., "In vivo fluorescence spectroscopy and imaging for oncological applications," Photochem. Photobiol. 68(5):603-632, 1998.

38 R. Richards-Kortum, E. Sevick-Muraca, "Quantitative optical spectroscopy for tissue diagnosis," Annu. Rev. Phys. Chem. 47: 555-606, 1996.

39 N. Ramanujam, "Fluorescence spectroscopy of neoplastic and non-neoplastic tissues," Neoplasia, 2: 89-117, 2000.

40 D. Chorvat Jr and A. Chorvatova, "Multi-wavelength fluorescence lifetime spectroscopy: a new approach to the study of endogenous fluorescence in living cells and tissues," Laser Phys. Lett. 6(3): 175-193, 2009.

41 I. Georgakoudi et al., "NAD(P)H and collagen as in vivo quantitative fluorescent biomarkers of epithelial precancerous changes," Cancer Res. 62(2): 682-687, 2002.

42 Y. Yuan et al., "Single-shot acquisition of time-resolved fluorescence spectra using a multiple delay optical fibre bundle," Opt. Lett. 33(8): 791–793, 2008.

43 Y. Yuan et al., "High-throughput acousto-optic-tunable-filter-based time-resolved fluorescence spectrometer for optical biopsy," Opt. Lett. 34(7): 1132-1134, 2009.

44 Y. Sun et al., "Fluorescence lifetime imaging microscopy: in vivo application to diagnosis of oral carcinoma," Opt. Lett. 34(13): 2081-2083, 2009.

45 Y. Sun et al., "Fluorescence lifetime imaging microscopy for brain tumor image-guided surgery," J. Biomed. Opt. 15(5): 0506022, 2010.

46 D. S. Elson et al., "Miniaturized side-viewing imaging probe for fluorescence lifetime imaging (FLIM): validation with fluorescence dyes, tissue structural proteins and tissue specimens," New J. phys. 9:127, 2007.

47 S. Shrestha et al., "High-speed multispectral fluorescence lifetime imaging implementation for in vivo application," Opt. Lett. 35(15): 2558-2560, 2010.

48 A. Papour et al., "Optical imaging for brain tissue characterization using relative fluorescence lifetime imaging." J. Biomed. Opt. 18(6): 60504, 2013.

49 S. Cheng et al., "Flexible endoscope for continuous *in vivo* multispectral fluorescence lifetime imaging," Opt. Lett. 38(9): 1515-1517, 2013.

50 Y. G. Chung et al., "Diagnostic potential of laser-induced autofluorescence emission in brain tissue," J Korean Med Sci 12(2): 135-142, 1997.

51 A. C. Croce et al., "Diagnostic potential of autofluorescence for an assisted intraoperative delineation of glioblastoma resection margins," Photochem. Photobiol. 77(3): 309–18, 2003.

52 Q. Liu et al., "Compact point-detection fluorescence spectroscopy system for quantifying intrinsic fluorescence redox ratio in brain cancer diagnostics," J. Biomed. Opt. 16(3): 037004, 2011.

53 L. Marcu et al., "Fluorescence lifetime spectroscopy of glioblastoma multiforme," Photochem. Photobiol. 80: 98–103, 2004.

54 W. H. Yong et al., “Distinction of brain tissue, low-grade and high-grade glioma with time-resolved fluorescence spectroscopy,” Front. Biosci. 11: 1255–1263, 2006.

55 P. V. Butte et al., “Diagnosis of meningioma by time-resolved fluorescence spectroscopy,” J. Biomed. Opt. 10(6): 064026, 2006.

56 P. V. Butte et al., “Intraoperative delineation of primary brain tumors using time-resolved fluorescence spectroscopy,” J. Biomed. Opt. 15(2): 027008, 2010.

57 W. Stummer et al., “Extent of resection and survival in glioblastoma multiforme: identification of and adjustment for bias,” Neurosurgery 62(3): 564–576, 2008.

58 W. Stummer et al., “Fluorescence-guided resection of glioblastoma multiforme by using 5-aminolevulinic acid-induced porphyrins: a prospective study in 52 consecutive patients,” J. Neurosurg. 93(6): 1003–1013, 2000.

59 W. Stummer et al., “Fluorescence-guided surgery with 5-aminolevulinic acid for resection of malignant glioma: a randomised controlled multicentre phase III trial,” The lancet oncology 7(5):392–401, 2006.

60 Valdes et al., “Quantitative fluorescence in intracranial tumor: implications for ALA-induced PpIX as an intraoperative biomarker,” J. Neurosurg. 115(1): 11-17, 2011.

61 S. Kumar et al., “Multifocal multiphoton excitation and time correlated single photon counting detection for 3-D fluorescence lifetime imaging,” Opt. Express 15(20): 12548–61, 2007.

62 W. F. Cheong et al., “A review of the optical properties of biological tissues,” IEEE journal of quantum electronics, 26(12): 2166–2185, 1990.

63 T. J. Farrell et al., “A diffusion theory model of spatially resolved, steady-state diffuse reflectance for the noninvasive determination of tissue optical properties in vivo,” Med. Phys. 19(4): 879–888, 1992.

64 A. Kienle and M. S. Patterson, “Time-resolved diffusion equations for reflectance from a semi-infinite turbid medium,” J. Opt. Soc. Am. A Opt. Image Sci. Vis. 14(1): 246–254, 1997.

65 D. J. Cappon et al., “Fiber-optic probe design and optical property recovery algorithm for optical biopsy of brain tissue,” J. Biomed. Opt. 18(10): 107004, 2013

66 M. Johns et al., “Computational and in vivo investigation of optical reflectance from human brain to assist neurosurgery,” J. Biomed. Opt. 3(4): 437–445, 1998.

67 W. C. Lin et al., “Diffuse reflectance spectroscopy for in vivo pediatric brain tumor detection,” J. Biomed. Opt. 15(6): 061709, 2010.

68 N. Yadav et al., “In vivo detection of epileptic brain tissue using static fluorescence and diffuse reflectance spectroscopy,” J. Biomed. Opt. 18(2): 27006, 2013.

69 Z. Volynskaya et al., “Diagnosing breast cancer using diffuse reflectance spectroscopy and intrinsic fluorescence spectroscopy,” J. Biomed. Opt. 13(2): 024012, 2008.

70 S. McGee et al., “Model-based spectroscopic analysis of the oral cavity: impact of anatomy,” J. Biomed. Opt. 13(6): 064034, 2010.

71 M. G. Müller et al., "Spectroscopic detection and evaluation of morphologic and biochemical changes in early human oral carcinoma," Cancer 97(7): 1681–1692, 2003.

72 O. R. Sćepanović et al., "Multimodal spectroscopy detects features of vulnerable atherosclerotic plaque," J. Biomed. Opt. 16(1): 011009, 2011.

73 S. A. Toms et al., "Intraoperative Optical Spectroscopy identifies infiltrating glioma margins with high sensitivity," Neurosurgery, 57(S4): 382–391, 2005.

74 S. C. Gebhart et al., "Liquid-crystal tunable filter spectral imaging for brain tumor demarcation," Appl. Opt. 46(10): 1896–910, 2007.

75 G. M. Palmer et al., "Comparison of multiexcitation fluorescence and diffuse reflectance spectroscopy for the diagnosis of breast cancer (March 2003)," IEEE Trans. Biomed. Eng. 50(11): 1233–42, 2003.

76 C. Zhu et al., "Diagnosis of breast cancer using fluorescence and diffuse reflectance spectroscopy: a Monte-Carlo-model-based approach," J. Biomed. Opt. 13(3): 034015, 2010.

77 C. Zhu et al., "Fluorescence spectroscopy: an adjunct diagnostic tool to image-guided core needle biopsy of the breast," IEEE Trans. Biomed. Eng. 56(10): 2518–28, 2009.

78 J. Wu et al., "Analytical model for extracting intrinsic fluorescence in turbid media," Appl. Opt. 32(19): 3585–3595, 1993.

79 M. G. Müller et al., "Intrinsic fluorescence spectroscopy in turbid media: disentangling effects of scattering and absorption," Appl. Opt. 40(25): 4633–4646, 2001.

80 A. Kim et al., "Quantification of in vivo fluorescence decoupled from the effects of tissue optical properties using fiber-optic spectroscopy measurements," J. Biomed. Opt. 15(6): 067006, 2010.

81 K. Vishwanath and M-A. Mycek, "Time-resolved photon migration in bi-layered tissue models," Opt. Express 13(19): 7466–7482, 2005.

82 K. Vishwanath and M-A. Mycek, "Do fluorescence decays remitted from tissues accurately reflect intrinsic fluorophore lifetimes?" Opt. Lett. 29(13): 1512–1514, 2004.

83 K. Vishwanath et al., "Quantitative fluorescence lifetime spectroscopy in turbid media: comparison of theoretical, experimental and computational methods," Phys. Med. Biol. 47(18): 3387-3405, 2002.

84 L. Marcu et al., "Photobleaching of arterial fluorescent compounds: characterization of elastin, collagen and cholesterol time-resolved spectra during prolonged ultraviolet irradiation," Photochem. Photobiol. 69(6): 713–721, 1999.

85 D. A. Glenar et al., "Acousto-optic imaging spectropolarimetry for remote sensing," Appl. Opt. 33(31): 7412-7424, 1994.

86 G. Georgiev et al., "Spectral characterization of acousto-optic filters used in imaging spectroscopy," Appl. Opt. 41(1): 209-217, 2002.

87 "AOTF user manual," Brimrose Corporation of America, Sparks Glencoe, US.

88 "Photomultiplier tubes: basics and applications", 3rd edition, Hamamatsu, Japan.

89 M. Krishnamoorthy, “Optimization of a time-resolved spectroscopy system with an acousto-optic tunable filter employing a deconvolution method based on discrete Laguerre functions,” MSc thesis, McMaster University, 2010.

90 T. Papaioannou et al., “Effects of fiber-optic probe design and probe-to-target distance on diffuse reflectance measurements of turbid media: an experimental and computational study at 337 nm,” Appl. Opt. 43(14): 2846-2860, 2004.

91 T. Glanzmann et al., “Time-resolved spectrofluorometer for clinical tissue characterization during endoscopy,” Rev. Sci. Instrum. 70(10): 4067-4077, 1999.

92 J. Jo et al., “Fast model-free deconvolution of fluorescence decay for analysis of biological systems,” J. Biomed. Opt. 9(4): 743–752, 2004.

93 “American National Standard for Safe Use of Lasers,” ANSI Z136.1-2007 (ANSI, 2007).

94 J. A. Zuclich, “Ultraviolet-induced photochemical damage in ocular tissues,” Health Phys. 56(2):671-682,1989.

95 R. W. K. Leung et al., “Effects of incomplete decay in fluorescence lifetime estimation,” Biomed. Opt. Express 2(9): 2517-2531, 2011.

96 D. E. Hyde et al., “A diffusion theory model of spatially resolved fluorescence from depth-dependent fluorophore concentrations,” Phys. Med. Biol. 46:369-383, 2001.

97 W. R. Lloyd et al., “Instrumentation to rapidly acquire fluorescence wavelength-time matrices of biological tissues,” Biomed. Opt. Express 1(2): 574-586, 2010.

98 J. D. Pitts and M-A. Mycek, “Design and development of a rapid acquisition laser-based fluorometer with simultaneous spectral and temporal resolution,” Rev. Sci. Instrum. 72(7): 3061:3072, 2001.

99 K. R. Diamond et al., “Quantification of fluorophore concentration in tissue-simulating media by fluorescence measurements with a single optical fiber,” Appl. Opt. 42(13): 2436–2442, 2003.

100 M. S. Patterson and B. W. Pogue, “Mathematical model for time-resolved and frequency-domain fluorescence spectroscopy in biological tissues,” Appl. Opt. 33(10): 1963–1974, 1994.

101 W. R. Ware et al., “Deconvolution of fluorescence and phosphorescence decay curves. Least-squares method,” J. Phys. Chem. 77(17): 2018-2048, 1973.

102 K. C. Lee et al., “Application of the stretched exponential function to fluorescence lifetime imaging,” Biophys. J. 81(3): 1265-1274, 2001.

103 J. C. Andre et al., “Application of fast Fourier transform to deconvolution in single photon counting,” J. Phys. Chem. 83(17): 2285-2294, 1979.

104 M. Ameloot et al., “Simultaneous analysis of multiple fluorescence decay curves by Laplace transforms. Deconvolution with reference or excitation profiles,” Biophys. Chem. 23(3-4): 155-171, 1986.

105 V. Z. Marmarelis, “Identification of nonlinear biological systems using Laguerre expansion of Kernels,” Ann. Biomed. Eng. 21(6): 573-589, 1993.

106 A. Agrawal et al., "Sensitivity of time-resolved fluorescence analysis," IEEE. J. Sel. Top. Quant. 16(4): 877-885, 2010.

107 J. Liu et al., "A novel method for fast and robust estimation of fluorescence decay dynamics using constrained least-squares deconvolution with Laguerre expansion," Phys. Med. Biol. 57(4): 843-865, 2012.

108 E. M. Landaw and J. J. DiStefano III, "Multiexponential, multicompartmental, and noncompartmental modeling. II. Data analysis and statistical consideration," Am. J. Physiol. 246 (5 Pt 2): R665-677, 1984.

109 S. Dabir et al., "Fully automated deconvolution method for on-line analysis of time-resolved fluorescence spectroscopy data based on an iterative Laguerre expansion technique," J. Biomed. Opt. 14(2): 024030, 2012.

110 P. E. Gill et al., Practical Optimization, Academic Press, London, UK, 1981.

111 P. R. Bevington and D. K. Robinson, "Data reduction and error analysis for the physical sciences," Third edition, McGraw-Hill, 2003.

112 Y. G. Chung et al., "Diagnostic potential of laser-induced autofluorescence emission in brain tissue," J Korean Med. Sci. 12: 135–142, 1997.

113 V. Kecman, "Learning and soft Computing, support vector machines, neural networks, and fuzzy logic models," The MIT Press, Cambridge, MA, 2001.

114 N. Lue et al., "Portable fiber optic probe-based spectroscopic scanner for rapid cancer diagnosis: a new tool for intraoperative margin assessment," PLoS One 7(1): e30887, 2012.

115 J. Requejo-Isidro et al., "High-speed wide-field time gated endoscopic fluorescence-lifetime imaging," Opt. Lett. 29(19): 2249-2251, 2004.

116 Y. Sun et al., "Simultaneous time- and wavelength-resolved fluorescence spectroscopy for near real-time tissue diagnosis," Opt. Lett. 33(6): 630-632, 2008.

117 H. Xie et al., "Multispectral scanning time-resolved fluorescence spectroscopy (TRFS) technique for intravascular diagnosis," Biomed. Opt. Express 3(7): 1521-1533, 2012.

118 P. A. De Beule et al., "A hyperspectral fluorescence lifetime probe for skin cancer diagnosis," Rev. Sci. Instrum. 78(12): 123101, 2007.

119 B. A. Flusberg et al., "Fiber-optic fluorescence imaging," Nat. Methods. 2(12): 941:950, 2005

120 L. Marcu and B. A. Hartl, "Fluorescence lifetime spectroscopy and imaging in neurosurgery," IEEE J. Sel. Top. Quant. Electron. 18(4): 1465-1477, 2012.

121 N. Rajarm et al., "Design and validation of a clinical instrument for spectral diagnosis of cutaneous malignancy," App. Opt. 49 (2): 142-152, 2010.

Publications

(a) Peer-reviewed papers and manuscripts

Zhaojun Nie, Michelle LePalud, Mowly Krishnamoorthy, Frances Tse, Louis Liu, David Armstrong, Jamal Deen, and Qiyin Fang, "Time-resolved Fluorescence Spectroscopy in the Upper GI Tract: a Pilot *ex vivo* Study," manuscript in preparation.

Zhaojun Nie, Derek Cappon, Vinh Ngnyen Du Le, Joseph E. Hayward, Thomas J. Farrell, John Provias, Naresh Murty, William McMillan, and Qiyin Fang, "Integrated Time-resolved Fluorescence and Diffuse Reflectance Spectroscopy for Intraoperative Brain Tumor Margin Detection, " manuscript in preparation.

Zhaojun Nie, Ran An, Joseph E. Hayward, Thomas J. Farrell, and Qiyin Fang, "Hyperspectral Fluorescence Lifetime Imaging for Optical Biopsy," J. Biomed. Opt. 18(9): 096001, 2013.

Vinh Ngnyen Du Le, **Zhaojun Nie**, Joseph E. Hayward, Thomas J. Farrell and Qiyin Fang, "Measurements of Extrinsic Fluorescence in Intralipid and Polystyrene Microspheres," submitted to Journal of Biomedical Optics Express.

Shu-Chi Allison Yeh, Kevin Diamond, Michael Patterson, **Zhaojun Nie**, Joseph Hayward, and Qiyin Fang, "Monitoring Photosensitizer Uptake Using Two Photon Fluorescence Lifetime Imaging Microscopy," Theranostics 2(9):817-826, 2012.

(b) Presentations and posters

Zhaojun Nie, Derek Cappon, Joseph E. Hayward, Thomas J. Farrell, Michael S. Patterson, John Provias, Naresh Murty, William McMillan, and Qiyin Fang, "Integrated Time-resolved Fluorescence and Diffuse Reflectance Spectroscopy Optical Biopsy Instrument" in BIOS, 2011 SPIE photonics west, 2011. (Presentation)

Zhaojun Nie, Derek Cappon, Joseph E. Hayward, Thomas J. Farrell, Michael S. Patterson, John Provias, Naresh Murty, William McMillan, Brian Pikul, William H. Yong, and Qiyin Fang. "Integrated Time-resolved Fluorescence and Diffuse Reflectance Spectroscopy Optical Biopsy Instrument" in 9th Annual World Congress of SBMT on Brain, Spinal Cord Mapping and Image Guided Therapy, 2012. (Presentation)

Zhaojun Nie, Derek Capon, Joseph E. Hayward, Thomas Farrell, and Qiyin Fang, "Time-Resolved Fluorescence based Optical Biopsy Technology Development," in Thinking Ahead For a Strong Future Canada Research Chairs 2010.(Poster)

F. Tse, L. Liu, D. Armstrong, **Z. Nie**, M. LePalud, T. Mursalin, M. J. Deen, Q. Fang, "Time-Resolved Fluorescence Based Optical Biopsy in the UGI Tract: A Pilot ex vivo Study" Canadian Digestive Diseases Week, 2011.(Poster)

Derek J. Cappon, **Zhaojun Nie**, Thomas J. Farrell, Qiyin Fang, and Joseph E. Hayward, "A Novel Optical Property Recovery Algorithm for Use in the Optical Biopsy of Brain Tissue" in Digital Holography and Three-Dimensional Imaging, OSA Technical Digest, Optical Society of America, 2012.(Poster)

M. LePalud, F. Tse, J. Jo, M. Krishnamoorthy, R. Leung, D. Cappon, **Z. Nie** and Q. Fang, "Time-Resolved Fluorescence Spectra of Upper GI Tract: An Ex-Vivo Study", 217th ECS Meeting: The Hyatt Regency Vancouver and The Fairmont Hotel Vancouver, Vancouver, Canada, April 25-30 2010. (Presentation)